Carnegie Mellon University
MELLON COLLEGE OF SCIENCE

THESIS

SUBMITTED IN PARTIAL FULFILLMENT OF THE REQUIREMENTS
FOR THE DEGREE OF

DOCTOR OF PHILOSOPHY IN THE FIELD OF PHYSICS

TITLE: “Graphene Formation on the Carbon face of Silicon Carbide”

PRESENTED BY: Guowei He

ACCEPTED BY THE DEPARTMENT OF PHYSICS

Randall Feenstra	09/15/14
RANDALL FEENSTRA, CHAIR PROFESSOR	DATE
Stephen Garoff	09/15/14
STEPHEN GAROFF, DEPT HEAD	DATE

APPROVED BY THE COLLEGE COUNCIL

Fred Gilman	09/15/14
FRED GILMAN, DEAN	DATE

Graphene Formation on the Carbon Face of Silicon Carbide

Doctoral Thesis

August 2014

Guowei He

Advisor

Prof. R. M. Feenstra

Department of Physics

Carnegie Mellon University, Pittsburgh, PA 15213

Abstract

In this thesis, we study the structure of epitaxial graphene formed on polar faces of SiC - the (0001) face, also known as the Si-face, and the $(000\bar{1})$ face, known as the C-face. On both polar surfaces, graphene films are prepared in ultra-high vacuum (UHV), in environments either of argon or cryogenically purified neon, or in a low-pressure background of disilane. Characterization of graphene is done by using atomic force microscopy (AFM), low-energy electron diffraction (LEED), and low-energy electron microscopy (LEEM). In addition, a dynamical LEED structure calculation is performed to analyze the interface structures formed between graphene films and the C-face of SiC.

When SiC is heated at high temperature, Si atoms preferentially sublimate from the surface, leaving behind excess C atoms that self-rearrange to form graphene on the surface. We find, in agreement with other reports, that the structure and the electrical properties of graphene films formed on the two polar faces are very different, in many aspects. For example, in all environments we have employed, the graphene formation rate is slower on the Si-face than that on the C-face under the same preparation condition. Also, graphene films formed on the Si-face are generally more homogeneous and the domain sizes are larger, compared to those formed on the C-face (by "domain", we mean a surface area with constant thickness of multilayer graphene). On the Si-face, graphene lattice vectors are rotated 30º with respect to the SiC lattice vectors as observed by LEED, while on the C-face, graphene films are usually rotationally disordered which gives rise to streaking in the diffraction pattern. In addition, the electrical properties of graphene films are also quite different between these two polar surfaces. These differences between the two polar surfaces, we believe, can be attributed to the differences of interface structures between graphene films and the underlying substrate. In this thesis, we report our interpretation of these differences in terms of the detailed interface structures that form for graphene on the two polar surfaces.

For the Si-face, graphene films prepared in *vacuum* are of moderate quality; thickness uniformity e.g. for a film with average thickness of two graphene monolayer (ML) ranges between about 1 and 3 ML, and the surface morphology of the underlying SiC is found to contain numerous small pits. In this thesis, we report improvements in the morphology of graphene films for the Si-face utilizing environments of disilane, 1 atm of argon or 1 atm

cryogenically purified neon. The presence of disilane, argon, or neon gas decreases Si sublimation rate, thus increasing the temperature required for graphene formation. The higher graphitization temperature enhances the mobility of diffusing species, which in turn results in an improved morphology of the graphene films.

For the case of the C-face, graphene prepared in vacuum is of considerably *worse* quality than for the Si-face; a film with average thickness of 2 ML will contains areas covered by 0 – 5 ML of graphene. In order to improve the quality of graphene, the same preparation techniques (graphitization in 1 atm of argon, 1 atm purified neon, or in disilane) as we have used for the Si-face are employed for the C-face. When graphene is prepared in argon on the C-face, the morphology is found to become much worse (unlike the improvement found for the Si-face). We find that the surface becomes unintentionally oxidized before the graphene formation (due to residual oxygen in the argon), and hence become resistant to graphitization. This unintentional oxidization results in inhomogeneous islands of thick graphene forming over the surface. In contrast, utilizing purified neon can eliminate the unintentional oxidation while permitting increased preparation temperatures, and thus is found to improve the morphology of graphene on the C-face. Use of a low-pressure background of disilane yields a similar improvement. The morphology of graphene on both polar surfaces of SiC in these various environments is reported in detail in this thesis.

In terms of interface structure, the situation is presently well understood for the Si-face: the interface consists of a C-rich layer having $6\sqrt{3} \times 6\sqrt{3} - R30°$ symmetry, which is covalently bonded to the underlying SiC substrate. This interface on the Si-face acts as an electronic "buffer" layer between graphene films and substrate and provides a template for subsequent graphene formation. It is noteworthy that this interface on the Si-face occurs for all growth conditions. In contrast, formation of interface structures on the C-face is sensitive to both the starting surface of SiC and graphene preparation conditions. In this thesis, the graphene/SiC interface on the C-face is studied by varying the preparation conditions (sample temperature T, and silicon partial pressure P_{Si}). In vacuum, a 3×3 reconstruction is found before and after graphitization. At relatively low P_{Si} of 5×10^{-6} Torr, a 2×2 reconstruction is found, both before and after graphene formation. When graphene is formed on the C-face using 5×10^{-5} Torr of disilane (or using 1 atm of neon), a new interface structure forms between the graphene films and the

underlying substrate, which displays $\sqrt{43} \times \sqrt{43} - R \pm 7.6°$ ($\sqrt{43}$ for short) symmetry as revealed by *in situ* LEED immediately after graphitization. When subsequent oxidation of the surface is performed, the interface structure transforms to one with $\sqrt{3} \times \sqrt{3} - R30°$ symmetry. Electron reflectivity measurements coupled with the recent published first-principles computations indicate that the new interface structures consists a graphene-like layer that forms between the graphene and the underlying substrate, similar to that found on the Si-face. This graphene-like layer has the $\sqrt{43}$ symmetry due to bonding to the underlying SiC, but upon oxidation, these bonds are broken and the layer becomes "decoupled" from the SiC. The decoupled graphene-like layer then becomes a graphene layer. From a dynamical LEED structure calculation for the oxidized C-face surface, it is found that the interface structure transforms to that of a graphene layer sitting on top of a silicate (Si_2O_3) layer, with the silicate layer having the well-known structure as previously studied on bare SiC$(000\bar{1})$ surfaces.

A separate project discussed in this thesis is determination of size, shape, and composition of InAs/GaAs quantum dots (QD) by scanning tunneling microscopy (STM) and finite-element calculation. Cross-sectional STM images and finite-element calculations reveal individual InAs QDs having a lens shape with maximum base diameter of 10.5 nm and height of 2.9 nm. Comparison between the STM data and the computational results of the displacement of the dot profile out from the cleavage surface, together with measurements of its local lattice parameter, leads to an accurate determination of the cation composition as varying from 65% indium at the base of the QD to 95% at its center and back to 65% at its apex.

Acknowledgements

First and foremost, I would like to thank my advisor, Prof. Randall Feenstra for years of guidance not only on my research issues, but also on personal matters. Whenever I need help, he is always there to help. I am especially grateful for his tremendous effort in discussing and revising my papers and thesis. His encouragement led me to finish my Ph.D study, and I am very grateful that I can work with such a brilliant and nice scientist.

I would also like to thank my Ph.D thesis committee members, Prof. Michael Widom, Robert Suter, and Elias Towe, for their helpful scientific guidance. I thank Hilary Homer for helping me with paperwork issues, Al Brunk for helping me with computer issues, and Charles Gitzen for helping me to obtain experimental hardware.

In addition, I would like to thank my lab members Nishtha Srivastavas and Luxmi for teaching me various kinds of experimental techniques. I am so grateful for their collaboration and helpful discussions on my research projects.

Finally, I would like to thank my father and mother. Without their encouragement and selfless support, I could not finish my Ph.D study.

Contents

Chapter 1

Introduction

1.1 Introduction to graphene

Graphene is defined as a single layer of strongly bonded carbon atoms arranged in a hexagonal lattice, as shown in Fig. 1.1. One layer of graphene is denoted as single-layer graphene, and two or three graphene layers are known as bilayer or trilayer graphene, respectively. The atomic structure of graphene can be used as a basic building block for many other carbon-based materials, such as fullerenes, nanotubes or graphite [1]. For many years, graphene was considered as a purely academic material, since older theories predicted that pristine two-dimensional graphene would be unstable in reality due to thermal fluctuations that prevent long-range crystalline order at finite temperatures [2]. For this reason, 2D materials were presumed not to exist without a 3D base. However, in 2004, graphene and other free-standing 2D atomic crystals were experimentally discovered [3,4]. Since those discoveries, a lot of research effort has been devoted to understand the properties of graphene. Many interesting properties of graphene, such as unusual half-integer quantum Hall effect, a non-zero Berry's phase and a strong ambipolar electric field, have been unveiled [5,6]. Some basic properties of graphene will be discussed in detail in Section 1.2.

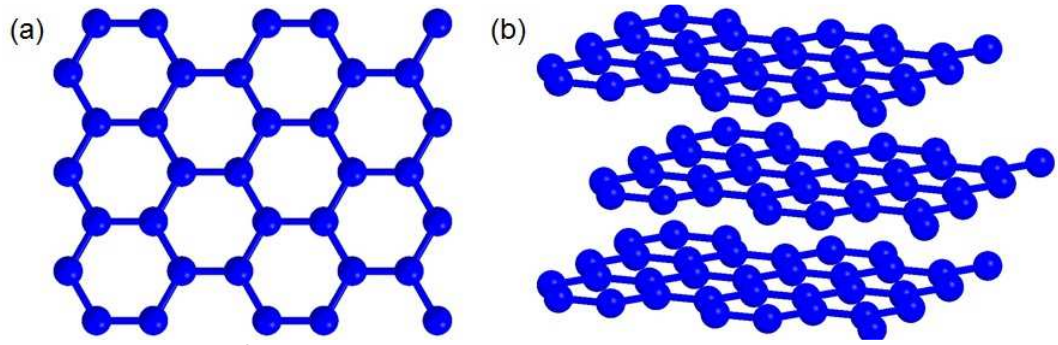

Fig. 1.1 Schematic view of graphene structure: (a) carbon atoms arrange in a hexagonal lattice; (b) different graphene layers commonly arrange in Bernal stacking.

Motivated by potential future applications using these unique properties of graphene, a lot of novel graphene devices have been investigated. For example, graphene was proposed to be utilized as the channel in field effect transistors since graphene has a high electron (or hole) mobility as well as low Johnson noise [7]. Nowadays, graphene has been successfully used to fabricate high-speed graphene-based transistors operating with outstanding cutoff frequencies [8,9]. However, pushing graphene-based technology into a commercial status is still restricted by difficulties in mass production and limited reproducibility in device performances. A lot of

research effort is also devoted to reproducibly making wafer-scale high-quality graphene. Some common graphene production techniques will be discussed in Section 1.3.

1.2 Basic electronic properties of graphene

A single carbon atom has four valence electrons with a ground-state electronic shell configuration of $2s^2 2p^2$. When carbon atoms form solids, the total energy decreases due to overlap of the electron wave functions and formation of energy bands. This energy gain is sufficient to promote a 2s electron into a 2p state. Normally, carbon is tetravalent, in which four electrons are in the states of 2s, $2p_x$, $2p_y$ and $2p_z$ and hybridize to form hybridized sp^3 electron states [10].

In the case of graphene, three electrons in the states of 2s, $2p_x$ and $2p_y$ form hybridized sp^2 electron states. These planar orbitals form the energetically stable and localized σ-bonds with the three nearest-neighbor carbon atoms in the honeycomb lattice. The last electron with the $2p_z$ orbital perpendicular to the graphene sheet forms a π bond. The overlap of the $2p_z$ orbital states between neighboring atoms plays a major role in the electronic properties of graphene. For this reason, the electronic structure of graphene can be described by a good approximation using an orthogonal nearest-neighbor tight-binding approximation, in which the electronic states are simply represented by a linear combination of the $2p_z$ states [11]. The electronic structure of graphene derived by this tight-binding approximation is described below.

Graphene sheet has a honeybomb crystal lattice as shown in Fig. 1.2(a). The lattice is triangular, with the lattice vectors

$$\vec{a}_1 = \frac{a}{2}(3, \sqrt{3}), \quad \vec{a}_2 = \frac{a}{2}(3, -\sqrt{3}),$$

where $a = 1.42\text{Å}$ is the distance between nearest carbon atoms.

The honeycomb lattice contains two atoms per elementary cell. They belong to two sublattices, A and B. Each atom from sublattice A is surrounded by three atoms from sublattice B, and vice versa, as shown in Fig 1.2(a). The vectors between nearest-neighbor atoms are

$$\vec{\delta}_1 = \frac{a}{2}(1, \sqrt{3}), \quad \vec{\delta}_2 = \frac{a}{2}(1, -\sqrt{3}), \quad \vec{\delta}_3 = a(-1,0).$$

The reciprocal lattice is also triangular. The lattice vectors of the reciprocal lattice are

$$\vec{b}_1 = \frac{2\pi}{3a}(1, \sqrt{3}), \quad \vec{b}_2 = \frac{2\pi}{3a}(1, -\sqrt{3}).$$

The Brillouin zone is shown in Fig. 1.2(b). High-symmetry points K, K' and M are also shown in Fig. 1.2(b), with the vectors

$$\vec{K}' = (\frac{2\pi}{3a}, \frac{2\pi}{3\sqrt{3}a}), \quad \vec{K} = (\frac{2\pi}{3a}, -\frac{2\pi}{3\sqrt{3}a}), \quad \vec{M} = (\frac{2\pi}{3a}, 0).$$

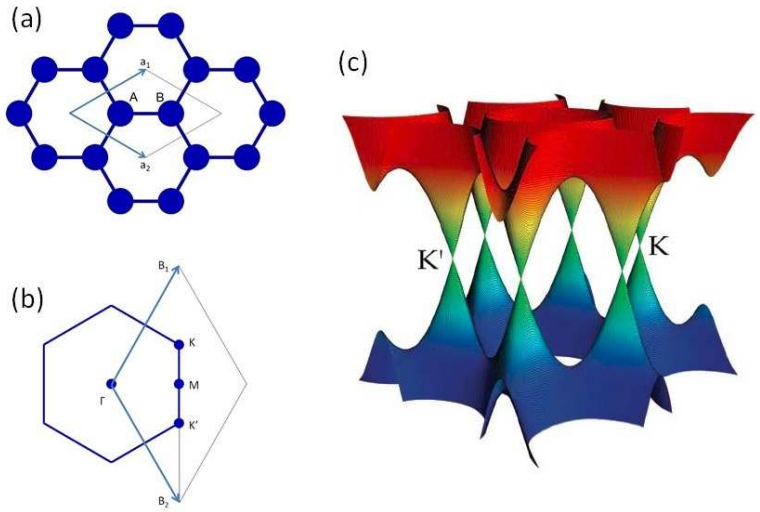

Fig. 1.2 (a) Honeycomb lattice of graphene. One unit cell contains two nonequivalent atoms labeled by A and B. (b) First Brillouin zone of graphene. Reciprocal lattice vectors and some special high-symmetry points are shown in the figure. (c) Band structure obtained by the tight binding approximation.

Using the nearest-neighbor approximation for the π states only, the wave function contains two π states belong to the atoms from sublattices A and B. In the nearest-neighbor approximation, there are no hopping processes within the sublattices; hopping occurs only between them. The tight-binding Hamiltonian is therefore described by a 2 × 2 matrix

$$\hat{H}(\vec{k}) = \begin{pmatrix} 0 & tS(\vec{k}) \\ tS^*(\vec{k}) & 0 \end{pmatrix},$$

where t is the hopping parameter and

$$S(\vec{k}) = \sum_{\vec{\delta}} e^{i\vec{k}\cdot\vec{\delta}} = 2\exp\left(\frac{ik_x a}{2}\right)\cos\left(\frac{k_y a\sqrt{3}}{2}\right) + \exp(-ik_x a).$$

The energy is

$$E(\vec{k}) = \pm t\left|S(\vec{k})\right| = \pm t\sqrt{3 + f(\vec{k})},$$

where

$$f(\vec{k}) = 2\cos(\sqrt{3}k_y a) + 4\cos\left(\frac{\sqrt{3}}{2}k_y a\right)\cos(\frac{3}{2}k_x a).$$

The band structure calculated by this simple tight-binding method is shown in Fig. 1.2(c). One can see that graphene has symmetric conduction and valence bands with respect to the Fermi energy set at 0 eV. At points K and K', one can see that $E(\vec{K}) = E(\vec{K}') = 0$, so graphene valence and conduction bands are degenerate at 6 points located on the corners of the Brillouin zone. These 6 points are often called Dirac points. Since the Fermi surface of graphene is composed of a finite set of 6 points on its Brillouin zone, graphene is usually termed a semimetal material with no overlap, or a zero-gap semiconductor [11].

To study the band structure in detail near the Dirac points, one can expand the Hamiltonian near the points K and K'. The effective Hamiltonians near the points K and K' are

$$\hat{H}_{K,K'}(\vec{q}) = \hbar v \begin{pmatrix} 0 & q_x \mp iq_y \\ q_x \pm iq_y & 0 \end{pmatrix},$$

where $\vec{q} = \vec{k} - \vec{K}$, and $v = \frac{3at}{2}$ is the electron velocity at the conical points.

The energy dispersion near the Dirac points exhibits a circular conical shape, as displayed in the Fig. 1.2(c), unlike the quadratic energy-momentum relation obeyed by electrons at the band edges in conventional semiconductors. Comparing this linear energy relation of graphene with the dispersion of massless relativistic particles obtained from the Dirac equation, one can see that graphene charge carriers can behave as Dirac fermions with an effective Fermi velocity that is about 300 times smaller than the speed of light [11,6].

Additional band features can be obtained when we use a model that goes beyond the nearest-neighbor tight-binding approach. Sophisticated implementations that consider interactions up to the third-nearest neighbor atoms can result in a more accurate description of the electronic properties [12]. More robust techniques, such as *ab initio* methods, predict that the conduction and valence bands are asymmetric about the Dirac points [13].

The amazing electronic properties of graphene have greatly motivated the scientific community to apply them for real-world applications. However, the absence of an energy band gap greatly restricts graphene's use in digital devices. So, strategies for inducing a band gap are

being sought. Several strategies have already been successfully employed to modify the electronic band structure of graphene, such as chemical doping, application of mechanical force or external electric/magnetic field, and stacking graphene layers in the form of bilayers [14,15]. Since lateral confinement of charge carriers can open up a band gap, advanced lithographic techniques have also been employed to tailor graphene sheets into narrow graphene structures. Such narrow graphene structures are known as graphene nanoribbons (GNR) and it has been demonstrated that their energy gap varies with the width [16].

Despite these successes, pushing graphene-based technology into a commercial status requires methods to produce wafer-scale high quality graphene reproducibly. In section 1.3, we will discuss some graphene production techniques.

1.3 Graphene production techniques

The exceptional electrical properties of graphene are attractive for future applications in electronics, such as ballistic transistors, field emitters, integrated circuits, transparent conducting electrodes, and sensors [17]. Most of these interesting applications require single-layer graphene on a suitable substrate with controlled and practical band gap, which is very difficult to achieve and control [17]. To date, several graphene production techniques have been established: mechanical cleaving, chemical exfoliation, chemical synthesis, chemical vapor deposition, and epitaxial growth on a SiC substrate are the most commonly used methods [17]. Some other techniques, such as unzipping nanotube [18] and microwave synthesis [19] are also reported; however, these techniques require further research [20]. Graphene synthesis methods are summarized in section 1.3.1. Epitaxial growth on a SiC surface, which is studied intensively in our group, will be discussed in detail in section 1.3.2 to section 1.3.5.

1.3.1 Overview of graphene synthesis methods.

Single-layer graphene was first produced by mechanical exfoliation in 2004. In this method adhesive tape was used to repeatedly slice down the graphene layers and they were placed on a silicon wafer using dry deposition [4]. This technique was found to be relatively easy to employ and is capable of producing different thicknesses of multi-layer graphene. Mechanical exfoliation using an AFM cantilever was found capable of producing graphene from bulk graphite. In this method, a very sharp AFM tip is used to penetrate into the graphite source to exfoliate layers

[21,22]. Graphene synthesis by catalytic thermal CVD has proved to be one of the best processes for wafer-scale graphene fabrication. In this process, thermally dissociated carbon is deposited onto a catalytically active transition metal surface and forms graphene at elevated temperature under atmospheric or low pressures [23,24,25]. During the reaction, the metal substrate works as a catalyst to lower the energy barrier of the reaction, and ultimately affects the quality of graphene [23]. When the process is carried out in a resistive heating furnace, it is known as thermal CVD, and when the process consists of plasma-assisted growth, it is called plasma-enhanced CVD or PECVD [11].

As a whole, all the above techniques are well established in their respective research fields. However, all synthesis methods have their own advantages as well as disadvantages depending on the final application of graphene. For example, although the mechanical exfoliation method is easy to use for fabricating different thicknesses of graphene (from monolayer to few-layer), it is not reliable for reproducibly obtaining a given thickness and it is not suitable for large scale production, which limits the feasibility of this process for industrialization. Using AFM tips to do the exfoliation may be feasible for mass production, but the process is limited to producing thick graphene (about 30 layers of graphene) [21,22]. In contrast, thermal CVD methods are more advantageous for large-area device fabrication and favorable for future complementary metal-oxide semiconductor (CMOS) technology. However, producing graphene on metals suffers from the essential disadvantage that many electronic applications require graphene on an insulating substrate. Transferring graphene from a metal to an insulating substrate inevitably leads to contamination and degradation of graphene [11].

Thermal graphitization of a SiC surface is another graphene synthesis method capable of producing large-area single-layer graphene [17]. We have intensively studied this type of graphene synthesis in the past several years, and I will discuss this method in detail in the following sections.

1.3.2 Epitaxial growth of graphene on SiC surface

Epitaxial thermal growth on a single crystalline SiC surface is one of the most promising methods of graphene synthesis and has been explored intensively for the last 7 to 8 years [17]. The term epitaxy can be defined as a method that allows deposition of a crystalline overlayer on a crystalline substrate, where there is registry between the overlayer and the substrate. The

deposited film is referred to as an epitaxial film on the substrate, and the process is known as epitaxial growth [26]. Research dealing with epitaxial graphene on SiC has attracted attention both academically and industrially due to its capability of producing high-quality and scalable graphene. The major advantage of this process is its ability of producing wafer-scale graphene films on an insulator or semiconductor surface (i.e. the SiC surface), which can be used for CMOS-based electronics directly [27,28].

SiC is known to have at least 200 crystallographic variants called polytypes. These polytypes all have equal numbers of Si and C atoms that are covalently bonded and are distinguished by different C-Si bilayer stacking sequences. The most common polytypes that are considered for electronic applications are cubic (3C), hexagonal (4H and 6H), and rhombohedral (15R). High quality 4H- and 6H-SiC wafers are commercially available, which are used in most of our experiments. Wafers can be *n*-type doped or semi-insulating and are available in different orientations. Typical orientations are basal planes or slightly misoriented from the basal plane by a miscut towards either $(11\bar{2}0)$ or (1100) directions for various angles. SiC has two polar faces perpendicular to the c-axis, as shown in Fig. 1.3. The face with outward normal in [0001] direction is the SiC(0001) surface, also called the *Si-face*. The face with outward normal in $[000\bar{1}]$ direction is the SiC$(000\bar{1})$ surface, also known as the *C-face* [29].

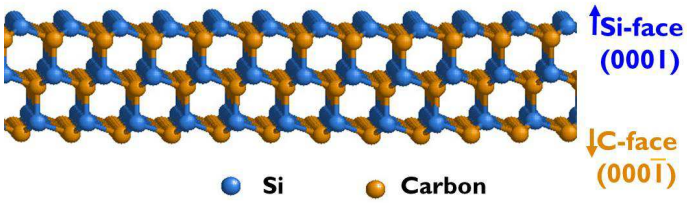

Fig. 1.3 Two inequivalent polar faces of SiC.

On both polar surfaces of SiC, graphene can be formed by heating the surface to 1100 – 1600 ºC, which causes preferential sublimation of Si atoms whereby leaving behind excess C atoms which self-assemble into graphene, as shown in Fig. 1.4.

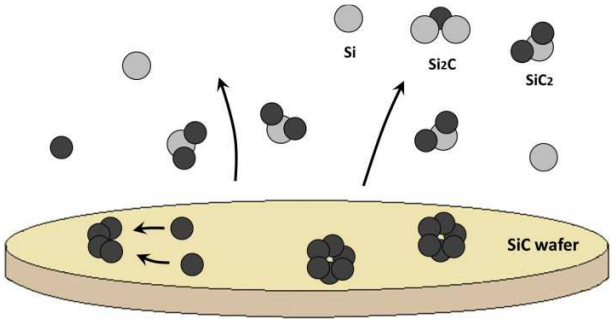

Fig. 1.4 Schematic view of graphene formation. Sublimation of vapor species leaves behind excess C atoms which self-assemble into graphene.

Graphene growth on SiC depends on several growth parameters, including gas pressure, temperature, and growth time. Thus, epitaxial graphene can be formed over a wide range of process conditions. As shown in the pressure-temperature diagram of partial pressure of Si over a SiC substrate (Fig. 1.5), for a given temperature, a buildup of excess C will occur on the surface for pressures of Si above the surface that are less than the indicated Si vapor pressure [30]. Under UHV conditions, graphene growth can be accomplished at temperatures as low as about 1200 ºC since the sublimated Si can be swept away by the vacuum system. In intermediate vacuum conditions, higher temperature is required. Inert gases such as argon can be added to further increase the required temperature, since the inert gas increases the Si partial pressure near the surface. This pressure-temperature relationship also implies that the growth rate will increase as the temperature increases, since more Si atoms sublimate and thus more C atoms are left on the surface to form graphene. Therefore, the graphene growth can be controlled through the choice of temperature, growth time and pressure [30].

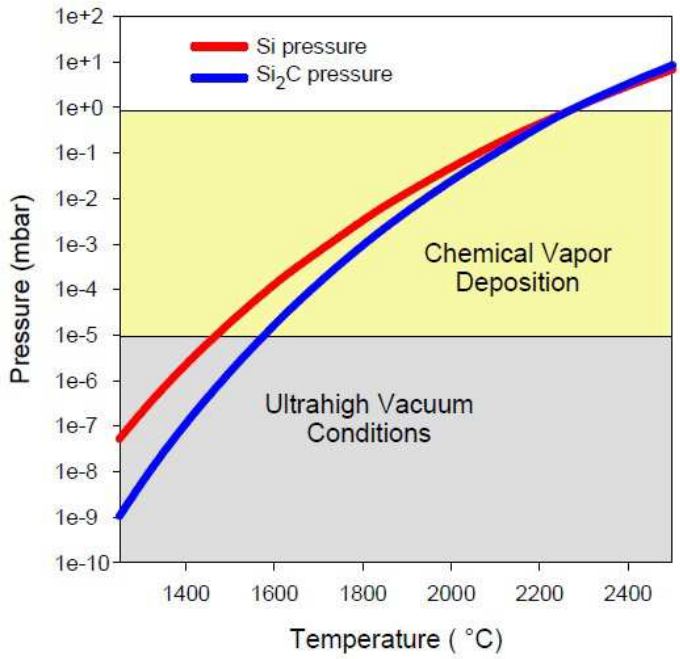

Fig. 1.5 The vapor pressure of Si and Si_2C over SiC as a function of temperature. For a given temperature, a buildup of excess C will occur on the surface for pressures of Si above the surface that are less than the indicated Si vapor pressure. The chemical vapor deposition and ultrahigh vacuum conditions are shown in colored zone [30]. For a given temperature, the necessary vacuum conditions near the surface can be determined from the curves.

The above simple model gives us a general picture of graphene growth on SiC. However, the model only considers the growth parameters of pressure, temperature and growth time, and makes use of the assumption that the surface reconstructions of SiC before graphene growth does not depend on these parameters. It is found that the surface reconstructions of SiC before graphene growth *are* quite different for the two polar surfaces of SiC [17, 31, 32]. These differences of surface reconstructions greatly affect both the structure and the electrical properties of graphene films formed on the two polar faces. So, we need to discuss graphene growth on the two polar surfaces of SiC separately.

In the next subsections, I will discuss the three main growth approaches employed in our group, which are differentiated by process pressure: UHV (10^{-9} Torr), 1 atm of gas (argon or cryogenically-purified neon), and a background of disilane (at typically 10^{-7} Torr – 10^{-4} Torr). As mentioned previously, the properties of graphene grown on the two SiC polar surfaces are very different, and so they are discussed separately. We first describe the preparation of the surface used to remove polishing damage, using a hydrogen-etching procedure common to both surfaces,

and we then give an overview of the graphene formation observed for each surface. My research work on the graphene formation is discussed in much more detail in Chapters 3 and 4.

1.3.3 SiC preparation

Since SiC is a very hard material, it is difficult to polish it without leaving defects, i.e. polishing scratches. A typical approach to remove these defects, so as to prepare a smooth surface with uniform orientation before graphene growth, is hydrogen etching. Hydrogen etching of SiC surface is performed using 99.9995% purity hydrogen with a flow rate of 10 lpm and at a temperature of 1550 ºC [33,34]. During the H-etching, damaged surface layers are removed from the substrate. For the Si-face with nominally 0 degree misorientation, the resulting surface shows a terrace and step morphology with the step heights being full unit-cell high [35]. For the C-face, morphology similar to that of the Si-face is observed but with steps half unit-cell in height [35]. An example of the terrace and step morphology is shown in Fig. 1.6(a).

However, we do sometimes observe less well ordered step arrays following H-etching. This can occur for either the Si-face or the C-face, but is more of a problem for the latter. For the C-face, surfaces that do not form a regular step-terrace array also tend to display a significant number of etch pits on the surface after H-etching. Fig. 1.6 compares the typical morphology of a C-face sample displaying few etch pits after H-etching [Fig. 1.6(a)] with one having many etch pits after H-etching [Fig. 1.6(b)]. We cannot at present say what aspect of the sample or surface produces a regular step-terrace array, or not, but the observation of Robinson *et al.* [36] that a slight miscut (>0.2º) leads to a more regular step arrangement is consistent with our own experience. It is also possible that a greater number of dislocations on certain wafers might lead to a higher number of etch pits, but we have not to date independently measured these two variable for a range of samples [41]. After hydrogen etching, the sample is then heated at a high temperature to produce graphene.

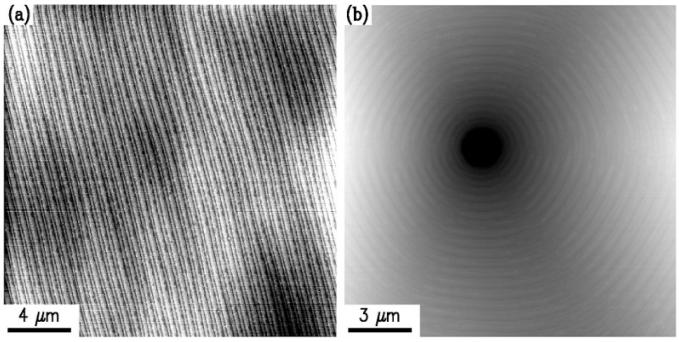

Fig. 1.6 AFM images from C-face SiC, showing typical morphologies of (a) a surface with very few etch pits, and (b) a surface with many etch pits (many etch pits were observed by optical microscopy, with one shown here). Gray scale ranges are 2 nm and 30 nm, respectively.

1.3.4 Epitaxial graphene on the Si-face

For graphene growth under UHV conditions on the Si-face, graphitization begins at a temperature of about 1300 ºC [37,38,39,40,41]. Normally, higher temperature and/or longer annealing time results in thicker graphene films. During graphene formation, the Si-face undergoes several surface reconstructions, as seen in LEED. These surface reconstructions have been studied by a number of other groups [42,43,44,45], and also observed by us. After H-etching, the surface shows a SiC 1×1 pattern along with a weak $\sqrt{3} \times \sqrt{3} - \mathrm{R}30°$ pattern as shown in Fig. 1.7(a). This $\sqrt{3} \times \sqrt{3} - \mathrm{R}30°$ pattern is associated with a small amount of unintentional oxidation of the surface [46,47]. Further heating the sample to 1400 ºC results in a carbon rich $6\sqrt{3} \times 6\sqrt{3} - R30°$ reconstruction (denoted $6\sqrt{3}$ for short) and graphene, as shown in Fig. 1.7(b). On further heating the sample at the same temperature for another 30 min, the graphene spots becomes more intense as compared to the SiC spots and the $6\sqrt{3}$ spots, indicating thicker graphene formed on the surface, as shown in Fig. 1.7(c).

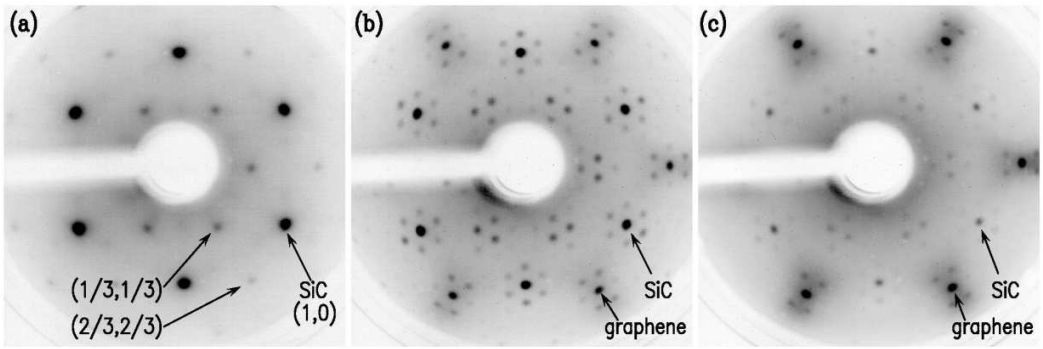

Fig. 1.7 LEED patterns at 100 eV. (a) LEED pattern acquired from a sample after 3 min of H-etching. In addition to the SiC(1,0) spots, we have marked the (1/3,1/3) and (2/3,2/3) spots associated with a

$\sqrt{3} \times \sqrt{3} - R30°$ reconstruction, that arises from residual oxidation of the surface. (b) LEED pattern acquired after heating the sample in vacuum for 5 min at 1400 ºC. Additional 1 × 1 spots associated with graphene appear. They are rotated from the SiC 1 × 1 by 30º. The 6 fold satellite spots around the SiC and the graphene spots arise from the $6\sqrt{3} \times 6\sqrt{3} - R30°$ reconstruction. (c) LEED pattern acquired after further heating of the sample in vacuum for 30 min at 1400 ºC.

On the Si-face, the $6\sqrt{3}$ reconstruction begins at about 1150 ºC (prior to graphene formation) and it continues after graphene formation. Using scanning tunneling microscopy (STM), it has been demonstrated that the $6\sqrt{3}$ reconstruction persists beneath the graphene [48]. Emtsev *et al*. mapped out the valence band structure of the $6\sqrt{3}$ reconstruction using angle-resolved photoemission spectroscopy (ARPES) [32,49]. They found that the $6\sqrt{3}$ reconstruction shows graphene-like σ bands implying that the arrangement of atoms in this structure is similar to that of graphene, but it fails to exhibit graphene-like π bands near the Dirac points implying strong covalent bonding with the underlying substrate [32]. As graphene films form on top of the $6\sqrt{3}$ reconstruction, the π-band becomes prominent and the graphene electronic transport is manifested and is accessible, implying that the $6\sqrt{3}$ reconstruction electrically isolates the graphene layer from the substrate. So, this $6\sqrt{3}$ reconstruction on the Si-face is covalently bonded to the underlying SiC substrate, and acts as an electronic "buffer" layer between graphene films and SiC substrate [32]. By the term *buffer layer* here, we mean a layer that has nearly the same structure as graphene, but is covalently bonded to the underlying material and therefore has different electronic structure than graphene. Schematic side views of the $6\sqrt{3}$ reconstruction and graphene layers are shown in Fig. 1.8.

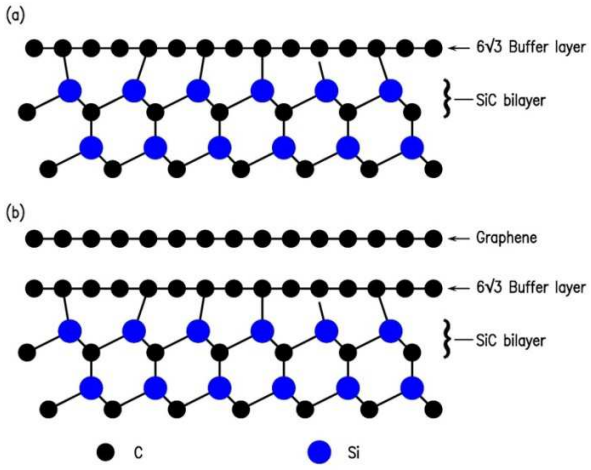

Fig. 1.8 (a) Side view of the $6\sqrt{3}$ layer. It is a graphene-like layer bonded to the substrate. (b) Further heating of the sample results in additional graphene layers on top of the $6\sqrt{3}$ layer. LEED pattern of such structure is like that of Fig. 1.7(b).

Since the structure of the $6\sqrt{3}$ layer is close to the structure of graphene, it provides a template for subsequent graphene formation and forces the graphene layers to be azimuthally aligned with respect to the underlying substrate [32]. After the formation of the $6\sqrt{3}$ layer, further annealing leads to sublimation of Si atoms below the $6\sqrt{3}$ layer. The excess C atoms beneath the original $6\sqrt{3}$ layer rearrange to form covalent bonds with the substrate, thus forming a new $6\sqrt{3}$ layer. The original $6\sqrt{3}$ layer decouples from the substrate to form a new graphene layer. It should be mentioned that this $6\sqrt{3}$ layer not only forms on the vacuum-prepared Si-face samples, but also forms on the Si-face samples prepared under nearly all of the preparation conditions investigated to date.

Since the $6\sqrt{3}$ layer is covalently bonded to the substrate, it is found to significantly affect the transport properties of graphene films on top of it. The influence of the $6\sqrt{3}$ layer is responsible for the intrinsic doping and somewhat low mobilities of Si-face graphene. Eliminating the covalent bonds between the $6\sqrt{3}$ layer and the underlying substrate would result in quasi-free-standing graphene with superior electronic properties. So, it would be desirable to decouple the $6\sqrt{3}$ layer from the substrate. In order to achieve this goal, some groups have reported on the exposure of Si-face graphene to hydrogen [50,51]. It is found that the hydrogen could pass through the interface layer and make covalent bonds with the Si atoms of the topmost SiC bilayer. This intercalation process is illustrated in Fig. 1.9. The decoupled $6\sqrt{3}$ buffer layer when studied by ARPES showed the π bands of graphene, confirming that it had become a graphene layer [52]. This method of decoupling the $6\sqrt{3}$ buffer layer could potentially lead to an improvement in the performance of graphene based devices [17]. Since the original work on hydrogen intercalation, it has been shown that such intercalation can also be achieved with other elements like oxygen [53], lithium [54,55], germanium [56], silicon [57], gold [58], etc.

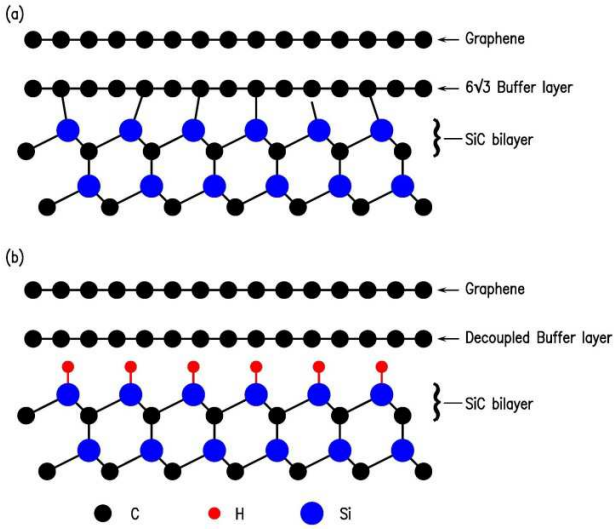

Fig. 1.9 Side views for the $6\sqrt{3}$ buffer layer before and after hydrogen intercalation. (a) Before intercalation, the $6\sqrt{3}$ buffer layer bonds to the substrate. (b) After intercalation, the $6\sqrt{3}$ buffer layer decouples and becomes a graphene layer.

Sheets of graphene are known to stack in a number of ways to produce graphite. The three most common stacking arrangements are: hexagonal or AA… stacking, Bernal or AB… stacking, and rhombohedral or ABC… stacking [17], as shown in Fig. 1.10. The lowest energy stacking and most abundant form (80%) in single crystal graphite is Bernal stacking [17]. The Bernal stacking is formed by stacking two graphene sheets on top of each other and rotating one 60º relative to the other about a z axis (in the $\hat{c}$ direction through any atom) [17]. Charrier *et al*. used STM to demonstrate that graphene layers formed by annealing the Si-face have the Bernal stacked structure [59]. The Bernal stacked structure is also confirmed by theoretical calculations. Ohta *et al*. calculated the expected band structure for bilayer, trilayer, and quadlayer graphene for both Bernal and rhombohedral stacking. By comparing the band structure predictions to band structure measurements obtained by ARPES on samples prepared in UHV, they showed that multilayer graphene grown on the Si-face is Bernal stacked [60].

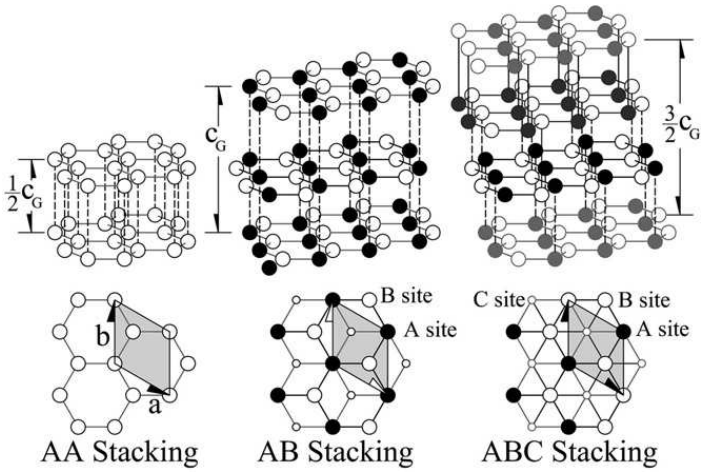

Fig. 1.10 Structure of graphite in different stacking arrangements. Unit cells are shown as shaded areas. (a) Hexagonal AA… stacking. (b) Bernal AB… stacking. (c) Rhombohedral ABC… stacking. From Ref. 17.

As mentioned in Section 1.3.3, substrates are hydrogen etched before graphene formation and the hydrogen etching process produces a uniform array of steps and terraces on the surface. When thin graphene (1-3ML) forms on the surface, the morphology of graphene shows vestiges of the original substrate step and terrace structure. The terrace width are up to several hundred nm in extent and the step heights reported ranged from 0.25 to 0.75 nm (this is variable with reports) [17,38,39,40,45]. At higher annealing temperature near 1350 ºC, the steps undergo considerable motion and the ordered step-terrace array no longer exists. The surface transforms into one with quite large (≥10 μm) terraces separated by step bunches [39]. In addition, it has been demonstrated by STM that graphene covers the steps like a carpet [45,61].

However, despite these somewhat ideal aspects of the surface structure, graphene formed on the Si-face in vacuum is *not* so ideal, with surface pits forming naturally on the surface [62] and some variation in graphene thickness occurring over the surface. We found that, for graphene thicknesses less than or equal to 2 ML, the uniformity of the graphene is rather poor. The nonuniformity in the film thickness appears to be an inherent property of the vacuum formation, and our results are similar to those reported by other groups [17,62,63,64]. Annealing at elevated temperatures and/or increased times leads to greater uniformity in the surface morphology, albeit with an increase in the average thickness. Some results are published in Ref. 39, where nearly layer-by-layer growth of the graphene is found for thicknesses greater than about 2 ML.

Uniform coverage of thinner films, e.g. single ML, is very difficult to achieve by annealing in vacuum. However, it was shown that the use of an argon inert-gas environment during the

annealing greatly improved the morphology of graphene [31], since the collisions between the desorbed Si atoms and the argon atoms will reflect the Si atoms back to the surface [65], thus effectively increases the Si partial pressure near the surface. The higher Si partial pressure leads to higher graphitization temperature. And this higher temperature enables reconstruction of the surface to be completed before graphene growth and increases carbon diffusion distances. Emtsev *et al*. used 100 – 900 Torr argon pressures and temperatures of 1500 – 2000 ºC and found improved morphology over UHV results except for the lowest pressure used [31]. We have produced graphene in one atmosphere of argon, and our results are consistent with those of Emtsev *et. al.* [39,41]. Our results will be discussed in detail in Chapter 3.

Aside from improved morphology, the structure of graphene grown under Ar is similar to that of the samples prepared in vacuum. Emtsev *et al*. reported that the X-ray photoelectron spectroscopy (XPS) spectra for graphene films prepared in Ar contain the same interface peak as report for UHV [31,66]. In addition, LEED patterns for argon-prepared samples show the diffraction spots consistent with the $6\sqrt{3}$ reconstruction and in which the graphene film is epitaxial and rotated 30º with respect to the SiC lattice [31]. In general, the electron mobility for argon-prepared samples was increased and the sheet charge density was decreased as compared to vacuum-prepared samples. Tedesco et al. reported that a sample grown at 1600 ºC for 120 min in 100 Torr Ar has the best 77 K mobility of 2647 $cm^2V^{-1}s^{-1}$ [67].

The use of disilane can also increase the Si partial pressure in the chamber, since disilane (Si_2H_6) decomposes into Si and H on the surface at high temperature [85]. We have found improvement in the morphology of graphene produced in disilane, as discussed in Chapters 3 and 4.

1.3.5 Epitaxial graphene on the C-face

Similar to graphene growth on the Si-face, graphene can be grown on the C-face using the previously described surface preparation recipes and annealing processes. However, graphene prepared on the C-face is quite different from that on the Si-face in many aspects. The growth rate of graphene on the C-face is over an order of magnitude faster than that on the Si-face [42,40]. For UHV preparation, areas of graphene with constant thickness on the Si-face extend laterally over many microns or more. In contrast, the domain size on the C-face is up to only a

micron or so, much smaller as compared to that on the Si-face. Importantly, the thickness variation between domains on the C-face is larger than that on the Si-face. For an average thickness of 4 ML, the thinnest and thickest regions on the C-face differ by 5 ML, while on the Si-face the variation in thickness over the surface is limited to 1 ML [40]. Thus, graphene is seen to form in a 3-dimensional manner on the C-face, whereas it forms in a layer-by-layer manner on the Si-face [40]. Tedesco *et al*. also reported similar results for the C-face, referring to the growth mechanism on C-face graphene as island nucleation and coalescence [68]. Creeth *et al*. explored growth conditions from 1250 ºC to 1450 ºC and found "granular" morphology for low temperatures and increased grain sizes at 1450 ºC for vacuum-prepared graphene [69]. We have seen similar morphology in our lab, and we attribute these areas of the surface to the presence of nanocrystalline graphite (NCG) [70,71]. We believe that this formation of the NCG is related to the inhomogeneous nucleation of graphene. Camara *et al*. discussed both intrinsic and extrinsic graphene formation. Their extrinsic graphene forms in an ordered manner, whereas we found disordered NCG, but the growth temperature employed by Camara *et al*. are considerable higher than ours and we believe that the higher temperature could account for this difference [72,73,74].

These differences in the growth modes for the two faces is surely influenced by the different temperatures used in the two cases in vacuum, about 1150 ºC for the C-face but 1300 ºC for the Si-face. Another contributing factor is the different interface structures for the two faces: a $6\sqrt{3} \times 6\sqrt{3} - R30°$ interface layer forms between Si-face SiC and the graphene, acting as a template for the formation of graphene, as discussed in the previous section, whereas on the C-face there are 3×3 and $(2 \times 2)_C$ structures that variously occur but do not seem to act as templates (This difference in interface structures likely affects the formation temperatures themselves [41]). The subscript "C" on the 2×2 label denotes that this reconstruction is more carbon rich than a different 2×2 structure that occurs on the same surface.

When the C-face is heated in vacuum, it undergoes very different surface reconstructions than the Si-face. Wide-area LEED patterns obtained from various C-face surfaces are shown in Fig. 1.11. From a surface following H-etching, Fig. 1.11(a), a 1×1 pattern is obtained, together with weak $\sqrt{3} \times \sqrt{3} - R30°$ spots arising from residual oxidation of the surface [75]. When the sample was further heated in vacuum at 1130 °C for 15 min, graphene formation began. As shown in Fig. 1.11(b), weak graphene streaks and a 3×3 pattern from the C-face reconstruction

are seen [32,40, 76 , 77]. Some groups reported seeing $(2 \times 2)_C$ in addition to the 3×3 reconstruction [78,79,80], as mentioned in the previous paragraph. Further heating the sample another 30 min results in multilayer-graphene, as shown in Fig. 1.11(c). The multilayer-graphene displays predominantly graphene streaks. These graphene streaks indicate that graphene layers on the C-face do not stack in the Bernal manner, but rather, considerable rotational disorder occurs [42,79]. Significantly, it was demonstrated by Hass *et al*. that this disorder produces a band structure (even for these multilayer films) that closely resembles that of single-layer graphene [28]. Hence these multilayer films on the C-face can properly be called multilayer-graphene, rather than graphite. It should be noted that, the graphene layers are not totally disordered, because a strong intensity modulation in the streaks indicates that there are preferential rotational angles. This disordered graphene is sometimes referred to as turbostratic graphene [81].

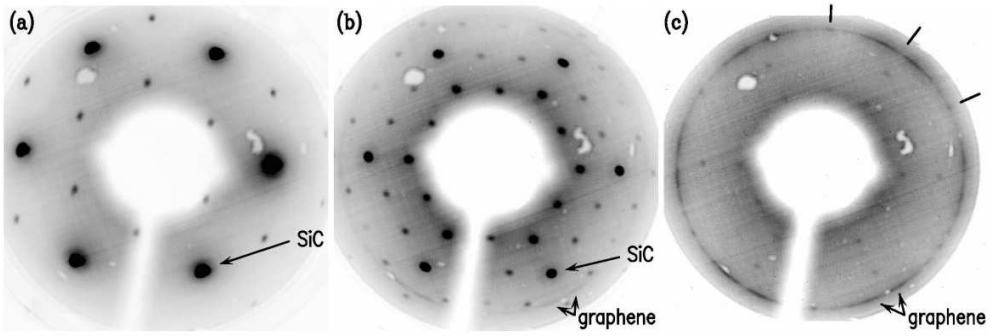

Fig. 1.11 LEED patterns acquired at 100 eV from the C-face: (a) following H-etching, (b) following heating in vacuum at 1130 ºC for 15 min, (c) following heating in vacuum at 1130 ºC for another 30 min. The black lines in (c) indicate a 60º angular range.

An STM study found that the $(2 \times 2)_C$ and 3×3 structure survive also at the interface between graphene and SiC (i.e. in analogy to the $6\sqrt{3}$ layer for the Si-face) [32,76,77]. Even so, it is not expected that the $(2 \times 2)_C$ or 3×3 structure would act as a template for subsequent graphene formation, since there is no simple coincidence between their unit cell size and that of graphene. The $(2 \times 2)_C$ structure is known to consist of 1/4 ML Si adatoms on the surface [82,83]. Side views of the $(2 \times 2)_C$ and 3×3 structures are shown in Fig. 1.12.

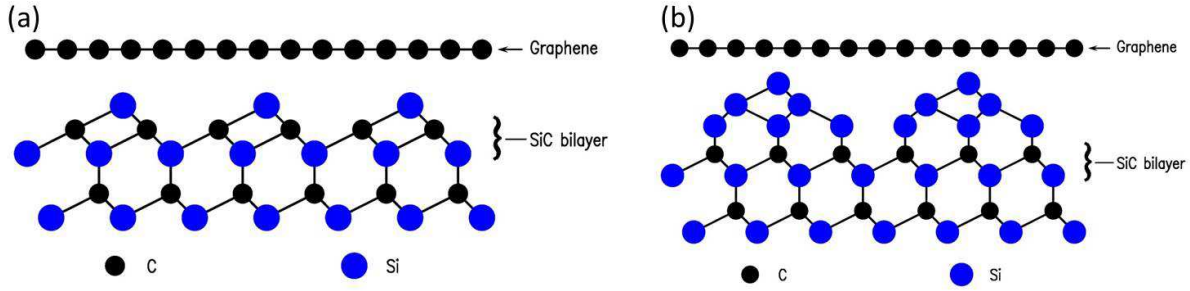

$(2 \times 2)_C$ 3×3

Fig. 1.12 Side views for (a) the $(2 \times 2)_C$ and (b) the 3×3 interface structures. The $(2 \times 2)_C$ and 3×3 structures, which appear on a bare SiC surface, survive when graphene forms on the surface. These reconstructions interact only weakly with the graphene, so they do not constitute a good template for producing rotational alignment of subsequent graphene layers.

For both the $(2 \times 2)_C$ surface and the 3×3 surface, it was found by Hiebel *et al*. by STM that graphene forms simply on top of the reconstructed surface, i.e. in the sense of a carpet covering the surface [76]. Emtsev *et al*. reported that the XPS C 1s core levels show only two peaks, one of which is attributed to the SiC bulk and the other is attributed to the graphene [32]. Both σ and π bands are noted by ARPES measurements and SiC bulk bands are almost completely attenuated with nearly a monolayer of coverage. The observed lack of perturbations of the spectra of graphene from the substrate implies weak coupling between the graphene and the underlying $(2 \times 2)_C$ and/or 3×3 surface [32]. Transmission electron microcopy (TEM) studies [84] and STM studies [76,77] from some groups also suggested weak interaction between graphene and the $(2 \times 2)_C$ surface or the 3×3 surface.

The dependence of C-face graphene/SiC interface structures on preparation conditions will be discussed in detail in chapter 4. Particularly, in Si-rich environments, utilizing either disilane at pressure of ~10^{-4} Torr or cryogenically purified neon at 1 atm pressure, we observed a new interface structure with $\sqrt{43} \times \sqrt{43} - R \pm 7.6°$ symmetry, not seen in vacuum-prepared C-face samples. When this new interface structure is oxidized, the surface changes to that of a graphene layer on top of a Si_2O_3 silicate layer. It is also noteworthy that the graphene layer thus formed has a much larger grain size than for graphene typically formed on the $(2 \times 2)_C$ or the 3×3 surfaces.

As discussed in the previous section, independent control over temperature and Si sublimation can be achieved, either by performing heating in an inert atmosphere such as argon

or using a Si-containing environment such as disilane [66,85]. These techniques have improved the morphology of graphene films on the Si-face, but for the C-face a similar level of improvement has *not* been obtained. Whereas heating the Si-face in argon is found to improve the quality of single-layer graphene, heating the C-face in argon produces relatively *thick* islands of multilayer graphene due to unintentional oxidation of the C-face in the argon environment. This unintentional oxidation of the C-face will be discussed in detail in Chapter 3. Graphene formed on the C-face in other Si-rich environments will also be discussed in detail in Chapter 3.

Chapter 2

Experimental Setup

2.1 Graphene Preparation and Characterization System

We produce graphene by heating SiC at high temperatures (>1000 ºC) under different environments, such as vacuum, 1 atm argon, 1 atm neon, or 5×10^{-5} Torr of disilane. Graphene samples are prepared in a custom-built ultra-high-vacuum (UHV) system, with a base pressure of 1×10^{-9} Torr, pumped by scroll pumps, turbo pumps, and an ion pump. As shown in Fig. 2.1, the whole system has two parts. The right-hand side of the system is a graphene preparation chamber. It is a double-walled chamber. Liquid N_2 can flow between the walls to cryogenically purify neon gas filled into the chamber. The left-hand side of the system is a LEED measurement chamber, in which we can do *in situ* LEED measurements. A dedicated manipulator is built to pick up samples inside the chambers and transport them between the two chambers.

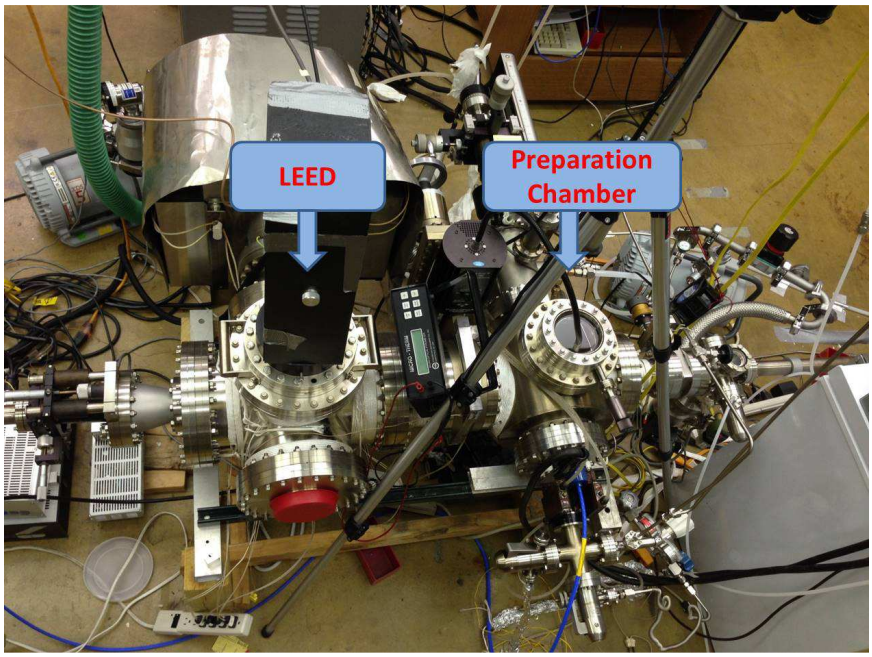

Fig. 2.1 Graphene preparation and LEED measurement system.

I designed and built the system; it is the "second generation" of graphene preparation systems in our group. There are several advantages of this new system. First of all, we can do *in situ* LEED measurements. With such measurements, we can study surface reconstructions at every stage of graphitization, i.e., we can do LEED measurements after an annealing and then transport the sample back to the preparation part and perform further graphitization. All these procedures are performed inside the same system, so that we avoid contamination from air. Secondly, gas introduction procedures are redesigned, so that fewer contaminants can go into the

system when we are filling the chamber with gases. Finally, the preparation chamber is a double-walled chamber. We can obtain a very clean inert gas environment by flowing liquid N_2 between the walls of the double-walled chamber. With this new system, samples were produced for my own studies, for some other group members, and for external collaborators [86,87,88]. In all cases, it was possible to obtain much cleaner and more convenient LEED observations for characterizing the graphene formation than in the previous system (where LEED observation required transferring the sample through air to a separate vacuum system).

The heating is accomplished by using a graphite strip. The material used to fabricate the graphite heater strip is semiconductor grade graphite produced by Poco Graphite (some material other than graphite could in principle be employed for the heater, but graphite turns out to be quite robust even at the high temperatures that we subject it to). No measurable contamination is found to be emitted from the graphite heater during graphitization. As shown in Fig. 2.2, the graphite heater has a bow-tie shape, with a narrow neck of 0.8 inch length and 0.55 inch width. The graphite heater is mounted on two large copper clamps at the ends of the graphite heater. Two thick water-cooled copper feedthroughs are used to transmit current and prevent melting of the copper clamps from high temperature. Current is supplied by a transformer capable of supplying up to 250 A. The heater strip is found to be quite robust; it can survive tens of heating cycles before breaking.

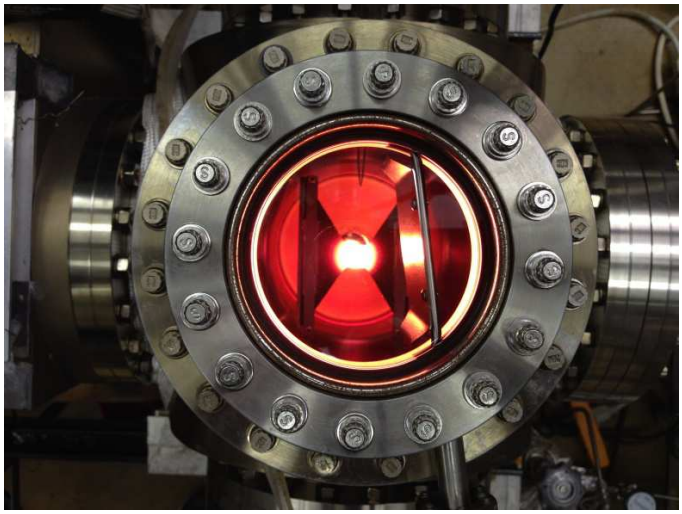

Fig. 2.2 Top view of the graphene preparation chamber. A bow-tie shaped graphite heater is in the middle of the chamber, and the sample is placed on the middle of the heater.

Most of our experiments were performed on nominally on-axis, *n*-type 6H-SiC or semi-insulating 4H-SiC wafers purchased from Cree Corp., with no apparent differences between results for the two types of wafers. The wafers had been mechanically polished and they are epi-ready (i.e. with chemical-mechanical polishing) either on the (0001) surface or the $(000\bar{1})$ surface. The wafers were cut into 1×1 cm^2 samples. To remove polishing damage, the samples were cleaned by hydrogen etching or annealing in disilane. Hydrogen etching is performed using 99.9995% purity hydrogen with a flow rate of 10 lpm and at a temperature of 1600 ºC for 3 min [89]. Cleaning using disilane is performed by heating the samples in 5×10^{-5} Torr of disilane at 850 ºC for 5 min. For making graphene in vacuum, the chamber is being pumped until the pressure reaches 1×10^{-9} Torr, and the annealing to form graphene is then performed. For making graphene in an argon environment, all the valves connected to the preparation chamber are quickly closed to isolate the chamber when it is still under vacuum. Argon gas is filled into the chamber, and then a vent valve is opened after the pressure inside is a little higher than 1 atm. When argon gas is slowly flowing through the chamber, the heating to form graphene is then performed. Making graphene in neon environment uses the same procedure as that for argon, except that liquid N_2 is flowing between the walls of the preparation chamber during annealing. For making graphene in disilane, disilane gas is filled into the chamber through a leak valve. The chamber is still being pumped during annealing in disilane, and the pressure inside is controlled by the leak valve. The pressure we used for disilane environment is up to about 4×10^{-4} Torr.

Temperature is measured using a disappearing filament pyrometer. The pyrometer is directed at the sample. Since the sample is transparent, it is mainly the heater strip that is seen. There is a large discrepancy between the heater temperature and the actual sample temperature, especially for the case of vacuum. Some experiments have been performed by other group members to evaluate these discrepancies. Normally, we use correction factors of 450 ºC and 350 ºC for semi-insulating samples and conducting samples, respectively, for the cases of vacuum and disilane. A correction factor of 150 ºC is used for 1 atm argon and neon environments (the presence of the gases leads to better thermal contact between the heater and the sample in these cases).

2.2 Low-energy electron diffraction (LEED)

LEED is a technique for determination of surface structures of crystalline materials [90]. In LEED measurements, a beam of low-energy electrons in the range of 10 to 300 eV is incident on the surface and the elastically backscattered electrons give rise to diffraction spots on a fluorescent screen [90].

LEED may be used in one of two ways:

(1) Qualitatively, by recording and analyzing diffraction patterns, LEED can be used to study the symmetry of surface structures, since the diffraction patterns correspond to the surface reciprocal lattice [91]. Similarly, in the presence of adsorbates, LEED diffraction patterns may also reveal information about the size, symmetry and rotational alignment of the adsorbate unit cell with respect to the substrate unit cell [91].

(2) Quantitatively, LEED can be used to determine precise atomic positions on the surface. The intensities of diffracted beams are recorded as a function of incident electron beam energy to generate the so called *I-V* curves. *I-V* curves are then calculated theoretically for several trial atom arrangements. By comparing the experimental and the theoretical *I-V* curves, accurate information on atomic positions on the surface can be revealed.

LEED measurements should be performed in an UHV system in order to keep the studied sample clean. The sample itself must be a single crystal with a well-ordered surface structure in order to generate distinguishable spots in a diffraction pattern. A typical LEED apparatus is shown in Fig. 2.3. Monochromatic electrons are emitted by an electron gun. The electrons are accelerated and focused into a beam, typically about 0.1 to 0.5 mm wide, by a series of electrodes serving as electron lenses. The electrons incident on the sample surface are backscattered both elastically and inelastically. But some energy-filtering grids placed in front of the fluorescent screen are employed to screen out the inelastically scattered electrons, so that only the elastically scattered electrons are detected by the florescent screen.

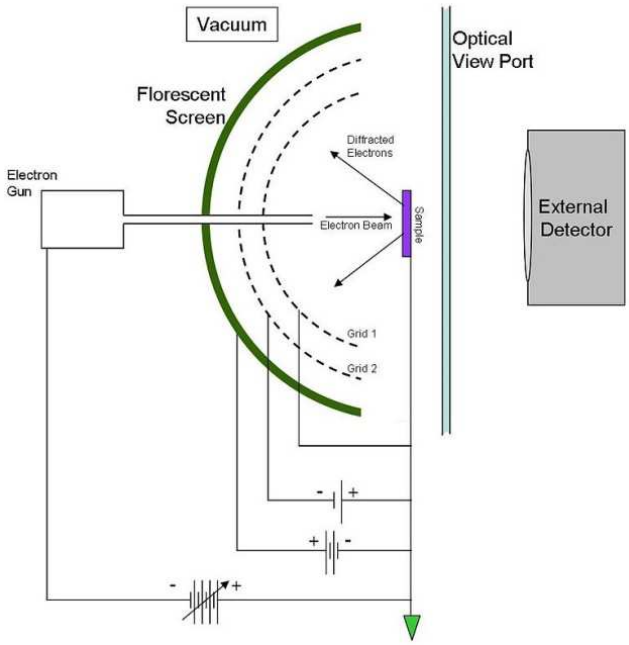

Fig. 2.3 A typical LEED apparatus. It contains a sample holder, an electron gun and a display system having a hemispherical fluorescent screen and some concentric grids.

2.2.1 LEED Patterns

The high surface sensitivity of LEED is due to the fact that low-energy electrons interact with solid and electrons very strongly. Upon penetrating a crystal, the intensity of the primary electron beam decays exponentially [92]. This effective attenuation means that only a few atomic layers are sampled by the electron beam and as a consequence the contribution of deeper atoms to diffraction progressively decreases [92].

Because most of the electrons detected by the fluorescent screen are elastically scattered from the surface, kinematic theory with only one scattering event is sufficient for qualitatively explaining LEED patterns. For an incident electron beam with wave vector $\vec{k}_0 = 2\pi/\lambda$ and scattered electrons with wave vector $\vec{k}' = 2\pi/\lambda$, the conditions for constructive interference are given by the Laue conditions

$$\vec{k}' - \vec{k}_0 = \vec{G},$$

where $\vec{G}$ is a vector of the reciprocal lattice.

Since only the first few atomic layers contribute to the diffraction, there are no diffraction conditions in the direction perpendicular to the sample surface. As a consequence, the Laue conditions reduce to a 2D form:

$$\vec{K}_{||} = \vec{k}'_{||} - \vec{k}_{||} = \vec{G}_{||},$$

i.e. the scattering vector component parallel to the surface ($\vec{K}_{||} = \vec{k}'_{||} - \vec{k}_{||}$) must equal to the vector of the 2D surface reciprocal lattice $\vec{G}_{||}$. It is apparent that the pattern observed on the fluorescent screen is a direct picture of the reciprocal lattice of the surface.

The Laue conditions can readily be visualized using the well-known Ewald's sphere construction. In order to extend the Ewald construction to a 2D problem, we must relax the restriction of the third Laue equation (perpendicular to the surface). This is done by attributing to every 2D reciprocal lattice point (h, k) a rod normal to the surface. In a 3D problem we use discrete reciprocal lattice points in the third dimension rather than rods; the rods in the 2D problem can be considered as regions where the reciprocal lattice points are infinitely dense.

As shown in Fig. 2.4, the possible elastically scattered beams $\vec{k}'$ can be obtained by the following procedures. According to the experimental geometry, the wave vector $\vec{k}_0$ of the incident electron beam is positioned with its end at the (0,0) reciprocal lattice point. The Ewald's sphere with radius $|\vec{k}_0|$ is then drawn with its origin at the beginning of the incident wave vector. As shown in Fig. 2.4, the condition $\vec{K}_{||} = \vec{G}_{||}$ is fulfilled for every point at which the sphere crosses a rod. By constructing every wave vector beginning at the origin and terminating at an intersection between a rod and the sphere, we obtain the diffraction pattern for the surface. The loss of the third Laue condition in our 2D problem ensures a LEED pattern for every scattering geometry and electron energy [91].

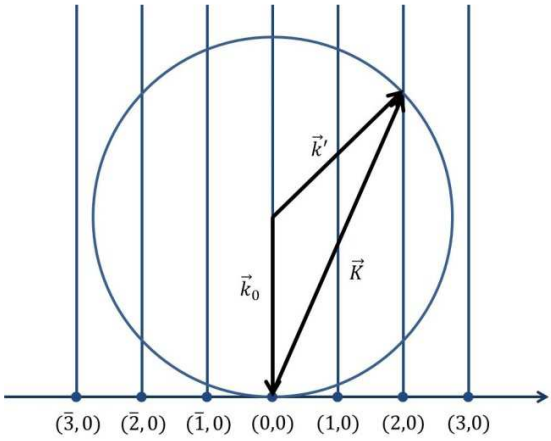

Fig. 2.4 Ewald sphere construction in two dimensions. The dots are reciprocal lattice points on the surface indexed by their coordinates. The rods representing the k_z values of the reciprocal lattice are drawn perpendicularly to the surface for each lattice point. The spots detected by the fluorescent screen are from the intersections between the rods and the sphere. Thus the diffraction pattern is a map of every reciprocal lattice point on the surface.

2.2.2 LEED for quantitative structure determination

From the discussion of the previous section, it seems that the intensities of spots in diffraction pattern will not change as a function of energy. However, that discussion is exact only in the limit of scattering from a true 2D network of atoms. This approximation is good enough to qualitatively interpret LEED patterns; however, to quantitatively understand the intensities of scattered electron beam, we need to consider electron scattering processes in more detail. In a real LEED experiment, electrons do penetrate a few of atomic layers into the crystal. The higher the energy of incident electron beam, the more layers of the crystal the electron beam can penetrate, and the third Laue condition (perpendicular to the surface) becomes more and more important. Experimentally, the intensity of a particular spot depends on the energy of the incident electron beam.

These modulations of the intensities of the Bragg reflections with respect to the incident electron energy can also be visualized by the Ewald construction. However, in this case, rods perpendicular to the surface have thicker or thinner regions. A Ewald construction for the intermediate situation where periodicity perpendicular to the surface enters the problem to a certain extent is shown in Fig. 2.5. When the Ewald sphere crosses a thicker region of the rods, the corresponding Bragg spot has stronger intensity, whereas thinner regions give rise to weaker spots [91]. Changing the energy of the incident electron beam is like changing the radius of the

Ewald sphere. So, when we change the energy of the incident electron beam, the Ewald sphere passes successively through thicker and thinner regions of the rods, and the intensity of a particular Bragg spot varies periodically [91]. The resulting curves of the spot intensities as a function of the electron energy are called *I-V* curves.

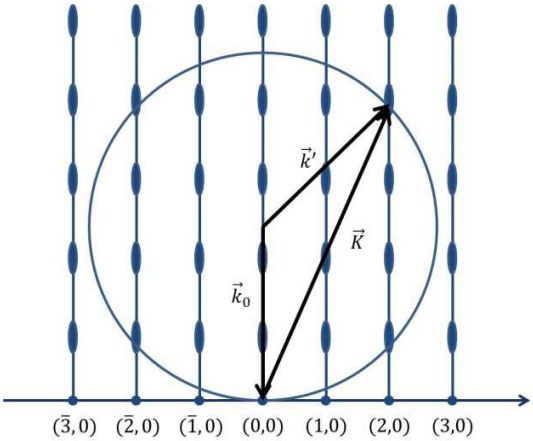

Fig. 2.5 Ewald sphere construction for a quasi-2D surface lattice. The thicker regions of the rods arise from the third Laue condition which cannot be completed neglected. When the Ewald sphere crosses a thicker region of the rods, the corresponding Bragg spot has stronger intensity, whereas thinner regions give rise to weaker spots [91].

I-V curves contain much more information about surface structures than simple LEED patterns. Analyzing the *I-V* curves can reveal accurate crystallographic information about a given surface [93]. However, since multiple-scattering effects in LEED are strong, there is no general method to extract the desired information directly from the *I-V* curves [93]. Instead, the exact atomic configuration of a surface can only be determined by a trial and error process, where computer-calculated spectra for many plausible models of the surface are compared to the experimental *I-V* curves. From an initial reference structure, a set of trial structures is created by varying the model parameters. The parameters are changing routinely, and the comparisons keep going until an optimal agreement between the calculated and experimental *I-V* curves is achieved.

The agreement between the experimental and the computer-calculated *I-V* curves is characterized by a reliability factor (or *R*-factor). A commonly used reliability factor is the one proposed by Pendry [94]. It is expressed in terms of the logarithmic derivative of the intensity

$$L(E) = \frac{1}{I(E)} \frac{dI(E)}{dE},$$

where the intensity is expressed as a sum of a series of Lorentzian peaks $I = \sum \frac{a_j}{(E-E_j)^2+V_{oi}^2}$ [94].

The *R*-factor is then calculated as:

$$R = (\sum_g \int (Y_{gth} - Y_{gexpt})^2 dE)/(\sum_g \int (Y^2{}_{gth} + Y^2{}_{gexpt}) dE),$$

where $Y(E) = L^{-1}/(L^{-2} + V_{oi}^2)$ and V_{oi} is the imaginary part of the electron self-energy [94]. In generally, $R_p < 0.2$ is considered as a good agreement, $R_p \cong 0.3$ is considered mediocre and $R_p \geq 0.5$ is considered as a poor agreement [94].

I-V curves are typically calculated by dynamic LEED calculations, with a muffin tin potential model [95]. However, it is not practical to calculate every trial *I-V* curves by conventional full dynamic LEED calculations, since the time needed to compute the electron wave diffracted from a surface scales essentially as N^3 with N the number of independent scattering centers in the unit cell [93]. For systems with many atoms in a unit cell and a large parameter space, the computational time becomes significant.

Tensor LEED was developed to reduce the computational time by avoiding full LEED calculations for each trial structure. It is based on the idea that, since low energy electron diffraction from a surface is governed by multiple scattering, a small modification of a given reference surface structure will only cause a small change in the diffracted electron wave functions and may be treated as a perturbation [96]. The time needed for calculating the perturbations scales only linearly with the number of atoms. So, once the wave function for a reference surface is calculated by a full dynamic LEED calculation, the wave functions of geometrically similar surfaces are deduced by calculating approximate amplitude changes.

To summarize, the process of obtaining accurate crystallographic information of a surface by LEED is as follows: (1) *I-V* curves are measured experimentally from the diffraction patterns of the surface under investigation. (2) A reference surface is defined, and *I-V* curves are calculated by the full dynamic LEED calculations. (3) *I-V* curves from small modifications of the reference surface are calculated by the Tensor LEED approximation, and *R*-factors are calculated for each trial structures. (4) Steps 2 and 3 are performed iteratively until a satisfactory *R*-factor is obtained. The Erlangen Tensor LEED package [93], with a slight modification by us, is used for the calculations in my studies.

2.3 Low-energy electron microscopy (LEEM)

2.3.1 LEEM instrumentation

LEEM is a surface science technique invented by Ernst Bauer in 1962, and then fully developed by Ernst Bauer and Wolfgang Telieps in 1985. LEEM uses elastically backscattered electrons to image atomically clean surfaces and thin films. Due to the large electron backscattering cross section of most materials, LEEM is an ideal technique to image surface dynamic processes such as surface reconstructions, epitaxial growth, step dynamics, etc. LEEM is a true imaging technique, as opposed to scanning techniques, and it has a high spatial resolution of about 10 nm [97,98,99].

The LEEM setup in our lab is a commercial LEEM III apparatus built by Elmitec, as shown in Fig. 2.6. It consists of (from left to right in Fig. 2.6): (1) Electron gun, used to generate electrons by thermionic emission from a source tip. (2) Condenser lenses (CL), used to focus and manipulate electrons leaving the electron gun. Electromagnetic quadruple electron lenses are used, the number of which depends on how much resolution and focusing flexibility the designer wishes. (3) Illumination aperture, used to control the area of a sample which is illuminated. (4) Magnetic beam separator, used to separate the illuminating and imaging electron beams. The imaging electron beam scattered from the sample is deflected by the separator to the imaging column on the right. (5) Objective lens, used to form a real image of the sample. The uniformity of the electrostatic field between the objective lens and sample determines most of the LEEM performance. (6) Contrast aperture, located in the center of imaging column. An image of the diffraction pattern is created by the objective lens, and the contrast aperture can be used to choose the desired spot to image. (7) Illumination optics, used to magnify the image or diffraction pattern and project it onto the imaging plate or screen. (8) Imaging plate or screen, used to image the electron intensity.

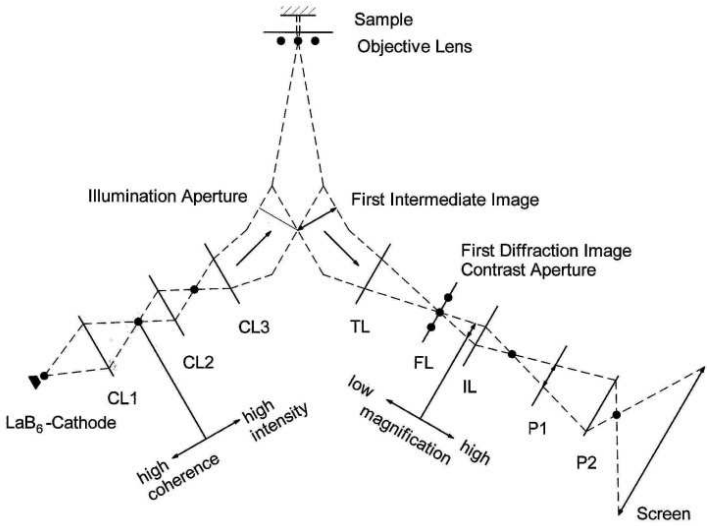

Fig. 2.6 LEEM setup and ray diagram. From Ref. 100.

In LEEM, a beam of high energy electrons (10-20keV) emitted by the electron gun, are focused at the back focal plane of the objective lens by the condenser lenses. The high energy electrons travel through the objective lens and begin decelerating to low energies near the sample surface because the sample is held at a potential close to that of the electron gun. The highly collimated electron beam impinges normally on the sample surface, with energy in the range of 0 to few hundred eV. The energy of the electrons incident on the surface is varied by adjusting a bias voltage between the sample and the electron gun. These low-energy electrons interact with the sample and are back scattered elastically from the sample surface. The backscattered electrons are then reaccelerated through the objective lens, and are reflected to the imaging column by the beam separator. The objective lens produces a magnified image of the sample in the beam separator, which is further magnified by several additional lenses in the imaging column. This image is projected onto an imaging detector with microchannel plate and phosphorous screen, and finally acquired by a computer controlled CCD camera [97,98,101].

Besides the real space imaging, LEEM can be used as a LEED. An illumination aperture can be inserted just before the objective lens. This aperture blocks out a fraction of the incoming beam, allowing only a certain area of the sample to be illuminated. The diffraction pattern formed on the channel plate will only arise from the specifically illuminated area of the sample, so that we can obtain diffraction patterns from any selected region on the sample. This is called micro-diffraction (μ-LEED) and we make use of this capability to study graphene films.

Prior to LEEM measurement, samples are outgassed at a temperature of 700 ºC. For the alignment of illumination and imaging columns, it is better to get started with photoelectron emission microscopy (PEEM) since it allows us to work on a wide area of the sample. In order to get a good intensity in PEEM, lead (Pb) is deposited on the sample. Once the alignment is done, the Pb is removed by heating the sample to a high temperature (> 1000 ºC) for a few minutes. The LEEM results presented in this thesis are done in bright-field mode, in which the (0,0) diffracted beam is used for imaging. The selection is done using the contrast apertures in the first diffraction image. Use of the contrast aperture also helps in cutting down the secondary emission and leads to sharp LEEM images, but at the cost of a reduction of intensity in the image.

2.3.2 Graphene thickness determination by LEEM

Besides imaging of sample surface, LEEM can also be used to determine the number of graphene layers on a surface. As described by Hibino *et al*. [102], areas of graphene with different thickness interact differently with incident electrons, thus producing varying contrast as a function of electron energy. To illustrate this argument from Hibino, a LEEM image obtained for multilayer graphene on the Si-face is shown in Fig. 2.7(a), and the intensities of the reflected electrons as a function of electron energy are shown in Fig. 2.7(b), for the specific locations A – E indicated in Fig. 2.7(a) [39].

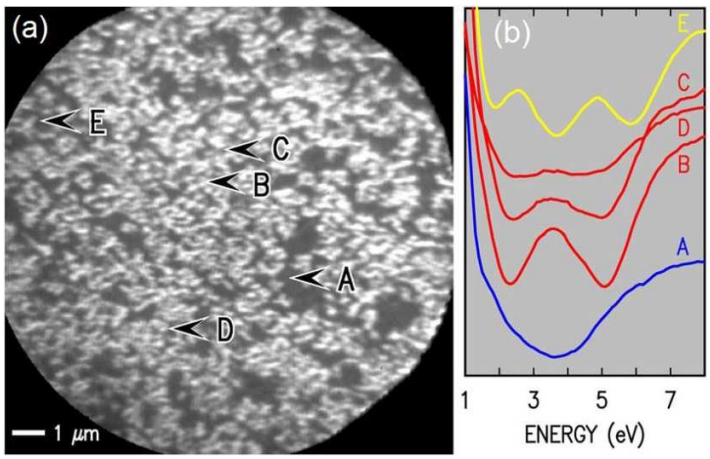

Fig. 2.7 (a) LEEM image at an electron-beam energy of 3.7 eV with 15 µm field of view for Si-face graphene prepared by heating in vacuum at 1320 ºC for 40 min. (b) Intensity of the reflected electrons from different regions marked in (a) as a function of electron-beam energy (curves are shifted vertically for ease of viewing).

Hibino *et al*. calculated the band structure of bulk graphite using a first-principles calculation based on local density functional theory with ultra-soft pseudo-potentials, as shown in Fig. 2.8 [102]. The bands circled by the red dashed line in Fig. 2.8(a) are the ones that were identified by Hibino *et al*. to be responsible for the LEEM reflectivity spectra of graphene. The reflectivity in the energy range of 1 to 7 eV, shown in Fig. 2.7(b), arises from this conduction band [102]. The oscillations in this energy window can be *phenomenologically* explained by quantization of energy levels in the conduction band due to finite thickness of graphene films. When the energy of the incident electrons matches with one of the quantized energy levels, the reflectivity is reduced and a dip occurs in the reflectivity curve. Phenomenologically, Hibino *et al*. estimated the quantized levels using a tight-binding calculation, in which the molecular orbitals on the graphite sheets were assumed as a basis set [102]. According to Hibino *et al*., for *m*-layer-thick film, energy levels are given by:

$$E = \varepsilon - 2t\cos[\frac{\pi n}{m+1}],$$

where ε is the band center energy, *t* is the transfer integral and *n*=1 to *m*. The bandwidth is 4*t*, which is estimated to be 6.4 eV from the first-principles calculation. Thus, *m*-layer-thick graphene films thus would produce *m* dips in the reflectivity [102].

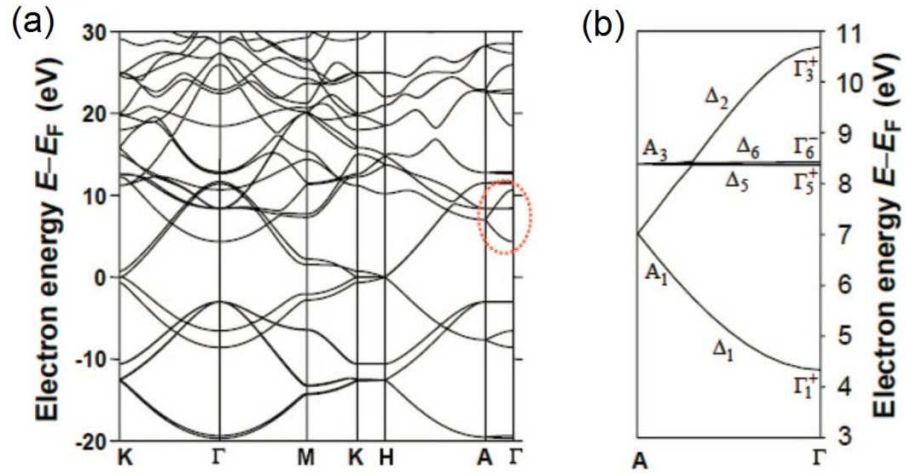

Fig. 2.8 (a) The band dispersion relation of bulk graphite calculated using the first-principles calculation, from Ref. 102. (b) The calculated conduction band in the Γ-A direction, which corresponds to the region indicated by the dotted circle in (a).

It should be noted that Hibino did not count the $6\sqrt{3}$ buffer layer as a graphene layer. Recently, by using additional first-principles computations, we have obtained a more quantitative

understanding of the reflectivity minima. The first-principles computations demonstrate that a free standing *n*-layer graphene slab actually produces $n-1$ reflectivity minima [103,104,105]. The minima in the reflectivity curves are actually associated with electronic states localized *between* the graphene layers (not *on* the layers, as assumed by Hibino *et al*.). These states are known as *interlayer states*, and they had been identified in earlier studies of graphite [106]. For *n* graphene layers (including the buffer layer), there are $n-1$ spaces between them and, hence, $n-1$ interlayer states. Coupling (in a tight-binding sense) between all the interlayer states then produces a set of coupled states, and reflectivity minima are observed at the energies of these coupled states, in agreement with experiment. Interpretation of LEEM reflectivity curves will be discussed in more detail in Chapter 4.

2.3.3 Data analysis

While taking LEEM data, a sequence of images is recorded starting with electron-beam energy of 0 eV and incrementing it 0.1 eV as we go from one image to another. As discussed in the previous section, the reflectivity oscillation enables us to determine local graphene thickness. To obtain local graphene thickness, we analyze the reflectivity curves by the following procedure [40,107,108,109]:

(1) At each pixel a reflectivity curve extending between about 2.0 and 6.5 eV is extracted from the images.

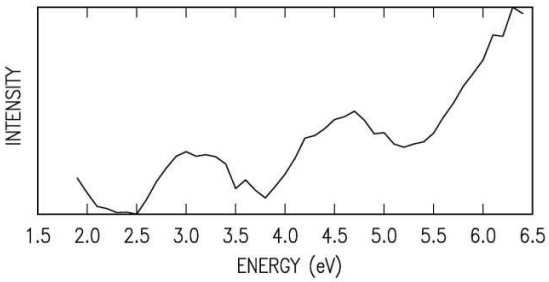

(2) A quadratic background is subtracted.

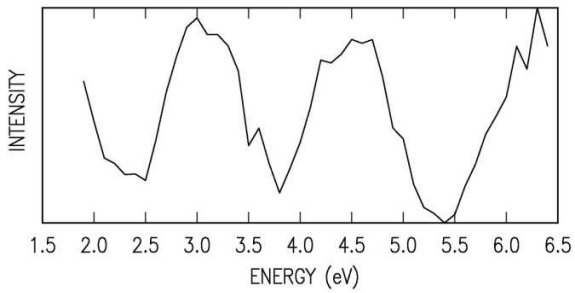

(3) A sinusoidal function with adjustable frequency (ω) and phase (φ), $Asin(\omega E + \emptyset)$, is fit to the curve. The process is repeated for all pixels in the sequence of images, and a scatterplot of the phase *vs*. frequency is constructed. Reflectivity curves associated with different number of monolayers are seen to occupy distinctly different regions in the scatterplot.

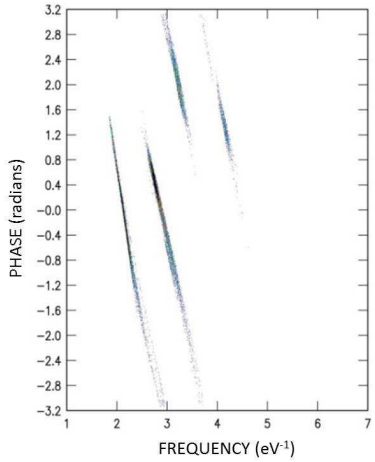

(4) The number of counts in the different regions of the scatterplot then gives the fraction of the surface covered with the different integer monolayer of graphene. From this we can calculate the average graphene thickness for a given sample. Also, we can construct a color map of the local graphene thickness by assigning each pixel in the image a specific color associated with the region that its reflectivity curve falls in [107].

2.4 Atomic force microscopy (AFM)

Atomic force microscopy is one of the foremost tools for imaging solid surfaces, with demonstrated resolution in the order of a nanometer. AFM has the advantage of imaging almost any type of surface, including polymers, ceramics, composites, glass, and biological samples [110,111].

As shown in Fig. 2.9, most AFMs today use a laser beam deflection system, where a laser beam is reflected from the back of a reflective cantilever and onto a position-sensitive photodiode detector.

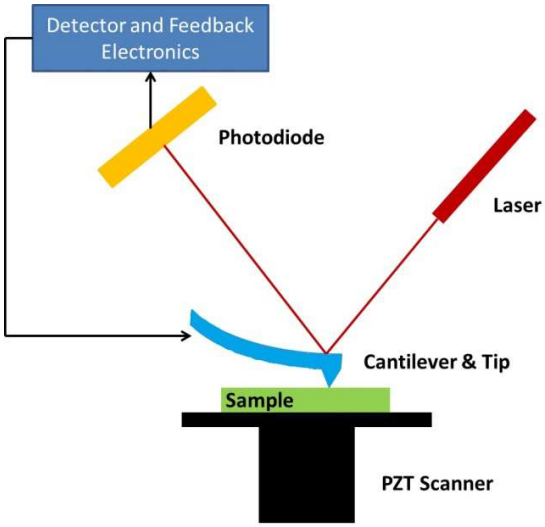

Fig. 2.9 Diagram of an atomic force microscope with laser beam deflection system.

AFMs operate by measuring force between the probe and the sample. The force is not measured directly, but calculated by measuring the deflection of the cantilever and knowing the stiffness of the cantilever. To acquire images of a sample surface, the tip is brought in contact with the sample. The tip experiences a force from the atoms on the surface that leads to a deflection of the cantilever. The deflection is then measured using a laser beam that is reflected from the cantilever and detected by a position-sensitive photodiode. The tip is positioned with high resolution by using piezoelectric ceramics, which can expand or contract with a presence of voltage gradient.

AFM operation is usually described as one of three modes, according to the tip-sample distance and the nature of the tip motion, as shown in Fig. 2.10.

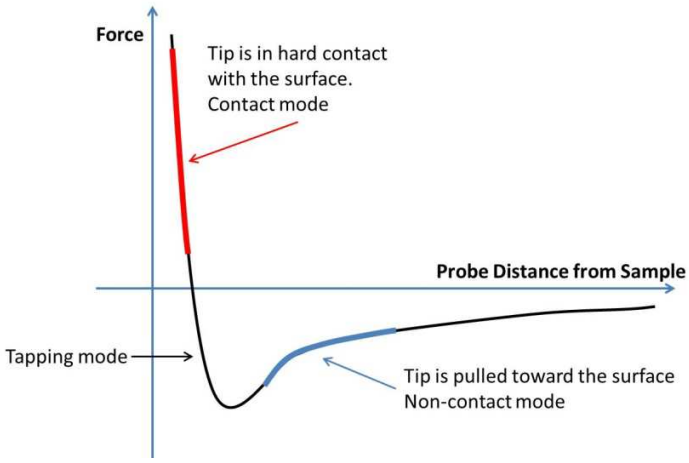

Fig. 2.10 Force between the tip and the sample as a function of tip-sample separation.

(a) Contact mode is the foremost mode of operation. In this mode, the tip is almost always at a depth where the overall force is repulsive. As the tip is dragged across the surface, it is deflected as it moves over the surface corrugation. In contact mode, the tip is continually adjusted to maintain a constant force against the surface (constant spring deflection), and then the surface profile is calculated from the adjustment in vertical sample position needed for this. However, the resolution in this manner is limited by the feedback circuit. Sometimes the tip is allowed to scan without this adjustment, and one measures only the deflection. This is useful for small, high-speed atomic resolution scans. Because the tip is in hard contact with the surface, the stiffness of the cantilever needs to be less that the effective spring constant holding atoms together.

(b) Another commonly used mode is tapping mode, which is also referred to as intermittent-contact or dynamic force mode. In this mode, the tip-sample distance is larger than that in the contact mode and the cantilever is oscillated at near its resonance frequency. Part of the oscillation extends into the repulsive regime, so the tip intermittently touches or “taps” the surface. When the tip comes closer to the surface, stronger interaction between the tip and the sample cause the amplitude of the oscillation to decrease. The height of the tip is continually adjusted to maintain constant oscillation amplitude as the tip scans over the surface, and these adjustments are then converted to a surface profile. The advantage of tapping the surface is improved lateral resolution on soft samples. Sample damage can also be prevented, because lateral forces such as drag, common in the contact mode, are virtually eliminated [112].

(c) AFMs can also operate in a noncontact mode. In this mode, a stiff cantilever is oscillated in the attractive regime. The forces between the tip and sample are quite low, in the order of pN. The detection scheme is based on measuring changes to the resonant frequency or amplitude of the cantilever.

Most of the AFM work presented in this thesis is done in tapping mode using a Digital Instruments Nanoscope III. The cantilevers used for imaging are made of Si doped with antimony.

Chapter 3

Morphology of graphene on SiC prepared in argon, neon or disilane environment

For graphene formation in vacuum, the formation temperature is determined by the preferential sublimation rate for Si as compared with C from the surface. It has been demonstrated that independent control over temperature and Si sublimation rate can be achieved, either by performing the heating in an inert atmosphere such as argon or using a Si-containing environment such as disilane [31,66,85]. The morphological evolution of graphene on the Si- and C-face of SiC in vacuum or argon has been previously presented in a number of papers published by our group [38,39,40,70]. In this chapter, I present additional, new data for graphene prepared in argon, cryogenically purified neon, or disilane.

3.1 Experimental Methods

Our experiments were performed on nominally on-axis (unintentional miscut ≤0.2º), *n*-type 6H-SiC or semi-insulating 4H-SiC wafers purchased from Cree Corp., with no apparent differences between results for the two types of wafer. The wafers were cut into 1 cm × 1 cm samples. Samples were chemically cleaned in acetone and methanol before putting them into the custom built preparation chamber which uses a graphite strip heater for heating the samples. To remove polishing damage, the samples were heated in either 1 atm of hydrogen at 1600 ºC for 3 min or 5 × 10^{-5} Torr of disilane at 850 ºC for 5 min.

Before graphitization, the hydrogen is pumped away from the chamber until a desired pressure of 10^{-8} Torr is reached. The samples were then either heated under 1 atm of flowing argon (99.999% purity) or 1 atm of neon. For the preparation in neon, the neon was cryogenically purified by flowing liquid N_2 between the walls of the double-walled chamber. A vacuum chamber connected to the graphitization chamber permits *in situ* LEED measurements, using a VG Scientific rear-view LEED apparatus.

For quantitative LEED analysis, diffraction spot intensities were measured at different energies in the range of 100 – 300 eV. For a SiC surface of specific termination, a single domain with only one orientation would give rise to a threefold symmetric LEED pattern in which the (1,0) and (0,1) spots have different intensity spectra. Since a six-fold symmetric LEED patterns are indeed observed, both possible domains with different orientations, i.e. rotated by 60° with respect to each other, are present on the surface. Spot intensities from two rotational domains were averaged and the resulting *I-V* curves were compared to theoretical LEED calculations in

order to retrieve details about atomic arrangement of interface structures. Theoretical *I-V* curves are calculated by full dynamical LEED calculations and optimization was carried out by tensor LEED, using a calculation package from Blum *et al*. [93] The Pendry *R*-factor, R_p, [94] was used for comparison between the experimental and calculated *I-V* curves.

Following graphitization our samples were transferred to an Elmitec III system for LEEM measurements. Samples were initially outgassed at 700 ºC, and then as part of the alignment procedure in the LEEM a few ML of Pb were deposited on the sample to enable photoemission electron microscopy (since Pb has a relatively low work function). This Pb was then removed from the sample by heating it to 1050 ºC prior to LEEM measurements. During LEEM measurement, the sample and the electron gun were kept at a potential of -20 kV and LEEM images were acquired with electrons having energy set by varying the bias on the sample, in the range of 0-10 eV. The intensities of the reflected electrons from different regions of the sample were measured as a function of the beam energy. These LEEM reflectivity curves show oscillations, which is associated with the number of graphene layers on the surface. From sequences of images acquired at energies varying by 0.1 eV, color-coded maps of graphene thicknesses were generated using the method described in Section 2.3.3. The surface of our graphene films were also studied by AFM using a Digital Instruments Nanoscope III in tapping mode.

3.2 Results

3.2.1 Argon Environment

Graphene formation on the *Si-face* of SiC in a vacuum environment has been well studied by many groups and is nowadays quite well understood. However, graphene formed in this manner is *not* so ideal. As mentioned in Section 1.3.4, we find that, for graphene thicknesses less than or equal to 2 ML, the uniformity of graphene is rather poor. Annealing at elevated temperatures and/or increased times leads to greater uniformity in the surface morphology, albeit with an increase in the average thickness. Nearly layer-by-layer growth of graphene is found for thicknesses greater than about 2 ML (although much thicker graphene is contained in the pits that are still present on the surface [113,114]).

Uniform coverage of thinner films, e.g. single ML, is very difficult to achieve by annealing in vacuum. However, use of an argon inert-gas environment during annealing permits the use of higher temperatures for an equivalent thickness of graphene, since the sublimation rate of Si is reduced by the argon [31,66]. Higher temperatures then permit a more equilibrium form of the surface structure, i.e. more uniform thickness and few, if any, of surface pits.

Figure 3.1 shows results for graphene on the Si-face formed in 1 atm of argon. This sample is annealed at a temperature of ≈1470 ºC for 15 min. As a result of the argon annealing, the steps undergo considerable motion, and we see in the AFM image in Fig. 3.1(a) large flat terraces separated by step bunches. A LEEM image of this sample, acquired at 4.4 eV, is shown in Fig. 3.1(b). As discussed by Hibino *et al.*, the reflectivity of electrons in the range of 1 – 7 eV shows distinct oscillations arising from the existence of discrete energy levels in the conduction band of graphene with wavevectors normal to the surface. Each such state produces a minimum in the reflectance, and for an *n*-layer thick film there are *n* such minima [102]. Reflectivity curves as a function of electron-beam energy from areas marked as A – E are shown in Fig. 3.1(c). The color-coded map of graphene thickness is shown in Fig. 3.1(d), with this surface area having an average graphene thickness of 1.1 ML. Importantly, the thicker regions of graphene are found near the step bunches. Between the step bunches, the surface is covered by uniform monolayer of graphene. It should be pointed out that, for this particular sample, the starting wafer has a miscut of ≈0.3º, larger than typical for our nominally on-axis wafers [39]. The larger miscut leads to a significant number of step bunches forming during the graphene formation (consistent with the report of Virojanadara *et al*. [115]).

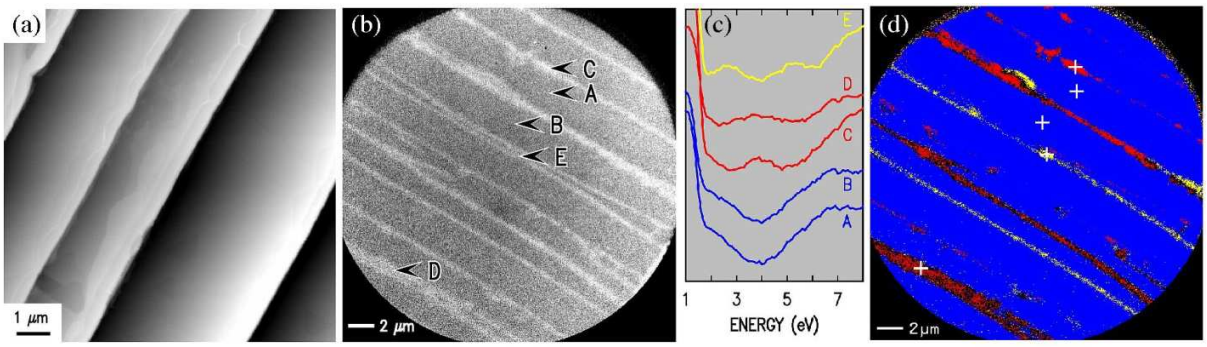

Fig. 3.1 Results for graphene on the Si-face, prepared by annealing at 1470 ºC for 15 min in 1 atm of argon, producing an average graphene thickness of 1.1 ML. (a) AFM image, displayed using grey scale range of 16 nm. (b) LEEM image acquired at electron-beam energy of 4.4 eV. (c) Intensity of the reflected electrons from different regions marked in (b) as a function of electron-beam energy. (d) Color-

coded map of local graphene thickness; blue, red and yellow correspond to 1, 2, and 3 ML of graphene, respectively. Small white or black crosses mark the locations of the reflectivity curves.

LEED patterns obtained from Si-face surfaces are shown in Fig. 3.2, for a surface following H-etching and for the argon-prepared graphene film of Fig. 3.1. In the former case the pattern consists of a 1 × 1 arrangement of SiC spots together with very weak (1/3,1/3) and (2/3,2/3) spots associated with a $\sqrt{3} \times \sqrt{3} - R30°$ arrangement that arises from residual oxidation of the surface [116]. For the graphitized surface there are additional 1 × 1 spots associated with graphene (rotated 30º relative to the SiC spots) and satellite $6\sqrt{3} \times 6\sqrt{3} - R30°$ spots surrounding both the primary SiC and graphene spots. Theses satellite spots are attributed to the underlying buffer layer [32,48,117,118,119,120]. Importantly, these LEED patterns from argon-prepared samples are almost the same as that from vacuum-prepared samples (shown in Fig. 1.7). The similarity of Fig. 3.2 and Fig. 1.7 illustrates that graphitization in 1 atm of argon greatly improves the morphology of graphene while maintaining the structure of graphene on the Si-face.

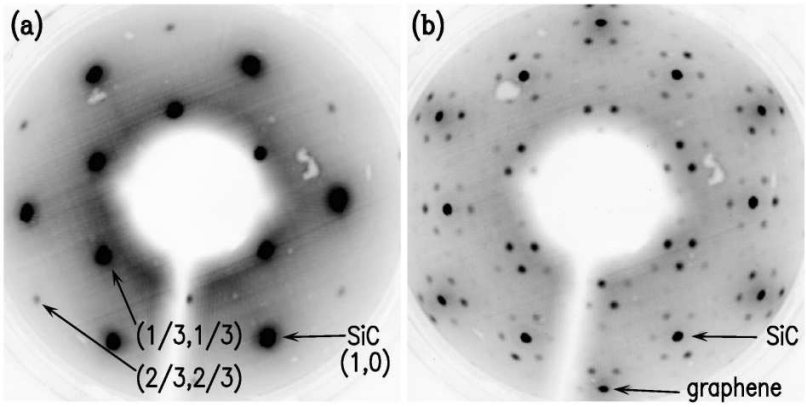

Fig. 3.2 LEED patterns acquired at 100 eV from Si-face surfaces: (a) following H-etching and (b) following graphitization, for the sample of Fig. 3.1.

Another important quantity to consider with respect to the monolayer graphene is the crystallographic grain size [121]. Although the graphene on the Si-face maintains essentially perfect rotational orientation with respect to the SiC (i.e. rotated by 30º), there still may be translational domain boundaries as well as 180º rotational boundaries in the film [122]. Studies of vacuum-prepared graphene by surface X-ray scattering reveal that graphene on the Si-face has mean grain size of 40 – 100 nm [59,121,123], which is on the same scale as (or slightly smaller than) the morphological disorder of such samples [39]. We are not aware of similar measurements for graphene prepared under argon. Nevertheless, by LEEM, domains on the

several-μm length scale or larger have been observed in monolayer graphene films [39,66,115], which likely represents the grain size for argon-prepared graphene.

For the *C-face*, to increase the formation temperature, one can try the same method of performing the annealing in argon, as used for the Si-face. Unfortunately, this technique is found *not* to be successful for the C-face.

We have attempted in eight experimental runs to form thin graphene on the C-face under 1 atm of argon, using nominally similar preparation conditions (≈1600 ºC for 15 min) each time. About half of those attempts resulted in nearly no graphene at all, and the other half produced very thick (>15 ML) graphene films. However, in two cases for samples that displayed no graphene over most of their surface, there were a few isolated 0.1-mm-sized areas that were graphitized. These areas are easily visible under an optical microscope [40].

AFM and LEEM studies near the edge of such area are shown in Fig. 3.3. In the AFM image, Fig. 3.3(a), there are many ridges (white lines at various angles) extending over the surface on the right and left sides of the image. These features are well known to be characteristic of the presence of graphene on the surface, and they arise from the thermal expansion difference between graphene and SiC as the samples are rapidly cooled after graphitization [40,124]. However, near the center of the image (to the right of the step bunch) no such ridges are seen, thus suggesting that no graphene is present there [40].

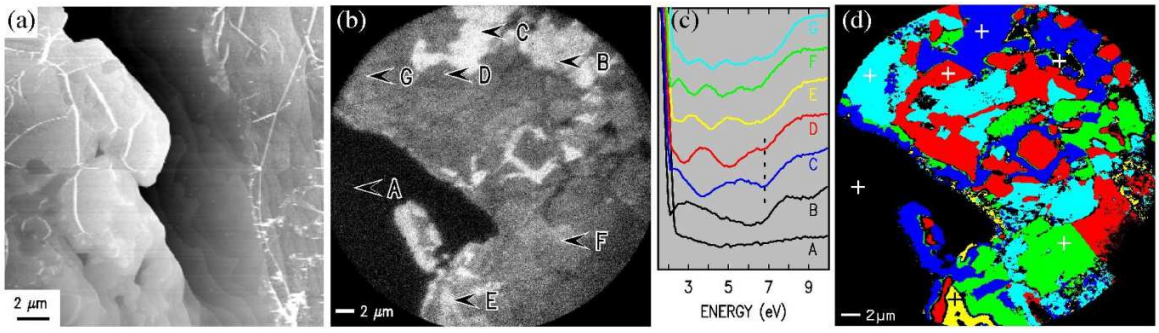

Fig. 3.3 Results of graphene on the C-face, prepared by annealing at 1600 ºC for 15 min in 1 atm of argon, yielding an average thickness of 3.0 ML of graphene (for this image, including only the areas where graphene covers the surface). (a) AFM image, displayed using grey scale range of 16 nm. (b) LEEM image at beam energy of 5.2 eV and with 25 μm field of view. (c) Intensity of the reflected electrons from different regions marked in (b) as a function of electron-beam energy and (d) color-coded map of local graphene thickness. (This data was obtained by Luxmi from Prof. Feenstra's research group) [40].

Fig. 3.3(b) shows a LEEM image acquired at 5.2 eV, and reflectivity curves from the associated sequence of images are shown in Fig. 3.3(c). Curves C – G correspond to 1 – 5 ML of

graphene, respectively. Curve C actually has an additional shallow minimum, marked by the dashed line at 6.8 eV, and this same feature is weakly seen in curve D. A color-coded map of the graphene thicknesses is shown in Fig. 3.3(d), revealing an average graphene thickness (over the area covered by graphene) of 3.0 ML [40].

On the left-hand side of the LEEM image of Fig. 3.3(b) is seen a black region, with reflectivity given by curve A. The reflectivity is seen to be nearly featureless over the range 3 – 10 eV, without the characteristic oscillations of graphene. It should be noted in this regard that, in addition to the oscillations in the range 2 – 7 eV, the reflectivity from graphene also increases over the energy range 8 – 10 eV because of additional band-structure effects [125]. This increase at higher energies is also not seen for curve A. The same reflectivity as in curve A was found over the vast majority of the surface. Thus, we can be certain that the surface, at location A in Fig. 3.3(b) and over the vast majority of the sample, is not covered with any graphene at all [40].

The reflectivity curve B has a shape never before seen on vacuum-prepared samples. The origin of this new reflectivity as well as the extra minima seen in the curves C and D are attributed to the existence of an oxidized SiC layer below the graphene. I will discuss such reflectivity curves from the C-face in more detail in Chapter 4.

LEED patterns obtained from areas of the argon-prepared samples that do *not* have any graphene display clear SiC 1 × 1 spots together with $\sqrt{3} \times \sqrt{3} - R30°$ spots (the latter vary in intensity over the surface). In Fig. 3.4, we display one of these patterns and compare it to the 3 × 3 LEED pattern formed by annealing a C-face sample in vacuum. The surfaces prepared in vacuum or argon are clearly very different. We have measured LEED intensity *vs* energy spectra (*I-V* curves) for the $\sqrt{3} \times \sqrt{3} - R30°$ pattern, as shown in Figs. 3.4(c) and (d). These spectra agree very well with the known spectra for a silicate (Si_2O_3) layer on the C-face of SiC [116].

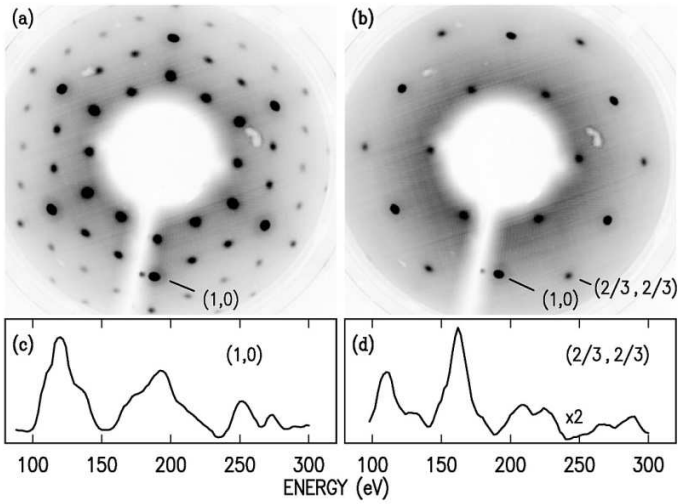

Fig. 3.4 LEED data acquired from C-face surfaces: (a) 3 × 3 pattern acquired at 100 eV from a sample prepared by annealing at 1000 ºC in vacuum, with the primary SiC (1,0) spot indicated; (b) $\sqrt{3} \times \sqrt{3} - R30°$ pattern acquired at 100 eV from a sample prepared by annealing in 1 atm of argon at 1400 ºC, with the (1,0) and (2/3,2/3) spots indicated; (c) and (d) Intensity vs energy characteristics for the two spots marked in (b).

A quantitative LEED analysis, demonstrating that the $\sqrt{3} \times \sqrt{3} - R30°$ pattern in Fig. 3.4 indeed arises from a silicate (Si_2O_3) layer on the C-face, are shown in Fig. 3.5. LEED *I-V* curves for the various spots of this pattern are shown by the solid line in Figs. 3.5(a) – (e). Also shown in those panels are the results of the dynamical LEED calculations, which were carried out using a model consisting of one layer of silicate (Si_2O_3) and six layers of SiC bilayer. The geometry parameters of the Si_2O_3 layer are the same as those used by Starke *et al*. [116,126]. We note that their analysis was done for various different surface terminations of the 6H-SiC surfaces, i.e., S1, S2, and S3, referring to one, two, or three SiC bilayers stacked in cubic manner before the first orientation change associated with the hexagonal stacking. Starke *et al*. found a best fit between experiment and theory for a 45%, 40%, and 15% combination of S1, S2, and S3 stacking, and we employ the same combination (no structural parameters are given for the S3 stacking by Starke *et al*. [116], but we use the same parameters for the S3 domain as the S1 domain, i.e., shifted by one bilayer). The Pendry *R*-factor for the fit between the theory and the experiment in Fig. 3.5 is 0.26, indicating good agreement between the experimental and theoretical *I-V* curves [94]. From this analysis, we conclude that the residual oxygen present during the argon annealing has oxidized the SiC surface, thereby inhibiting the formation of graphene over the majority of the surface.

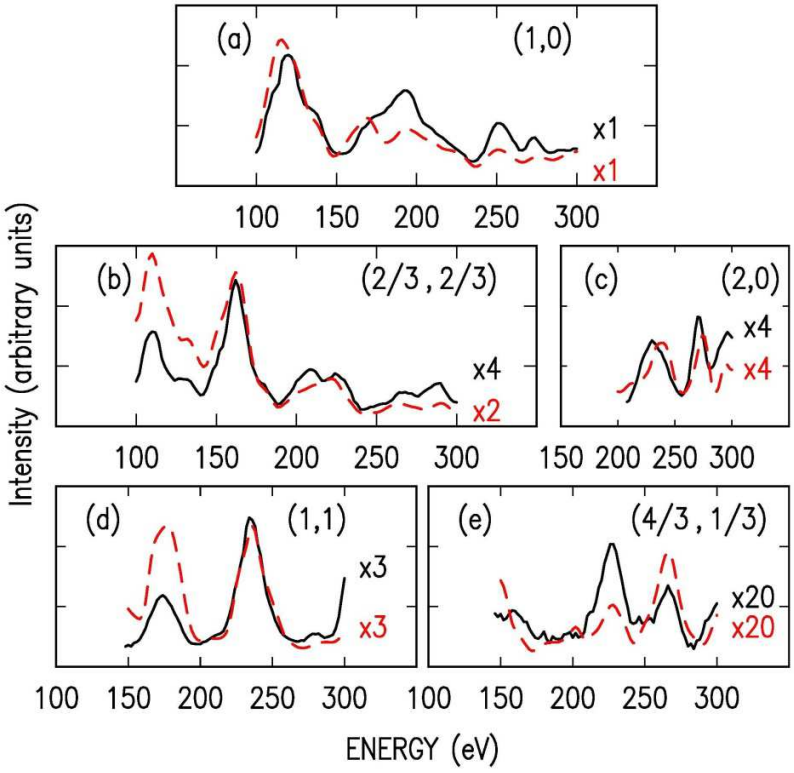

Fig. 3.5 (a) - (e) Set of experimental LEED spot intensity spectra (solid lines), together with theoretically calculated spectra (dashed lines). Spectra are from the same sample in Fig. 3.4(b).

However, regarding our interpretation that the oxidation of the C-face surface is inhibiting the formation of graphene, it should be noted that, in vacuum, the silicate layer is unstable at temperature above about 1200 ºC, at least for the Si-face [127]. This fact raises the possibility that the oxidation observed on our argon-prepared sample might have occurred while the sample was cooling down to room temperature, or during evacuation of the argon gas. To investigate this, we have taken a C-face 3 × 3 surface formed by annealing in vacuum, exposed it for 10 min at various temperatures to a 1 atm argon environment, and measured the resulting LEED pattern. For room-temperature annealing we find that the LEED pattern becomes noticeably dimmer but that the 3 × 3 spots are still faintly visible; no trace of any $\sqrt{3} \times \sqrt{3} - R30°$ spots are seen. But, after annealing in the Ar to >1000 ºC, the $\sqrt{3} \times \sqrt{3} - R30°$ spots appear. This pattern grows markedly in intensity as the temperature is increased to 1200 ºC, and then it maintains an approximately constant intensity as the temperature is increased to 1550 ºC. For annealing at 1640 ºC we find that the surface is graphitized over most of its area, although a few regions of

intense $\sqrt{3} \times \sqrt{3} - R30°$ remain. Thus, we find that the silicate is stable on the C-face, in the argon environment, for temperature up to ~1600 ºC.

Now, the main conclusion from the data of Figs. 3.3, 3.4 and 3.5 is clear: this C-face surface, prepared at high temperatures under 1 atm of argon, is covered only in a few areas by graphene, and there the graphene is many layers thick. Elsewhere on the surface no graphene is present. The absence of the graphene is attributed to unintentional oxidation of the surface, and this mechanism would seem to account also for the islanding of the graphene on the C-face reported by both Camara *et al*. [73] and Tedesco *et al*. [68]

For the C-face in vacuum we found that it graphitizes easier than the Si-face, indicating a higher surface energy (i.e. less stable surface) of the C-face. Now, in argon, we find that the C-face surface is more resistant to graphitization than the Si-face, indicative of a lower surface energy for the C-face. The presence of the oxide layer on the C-face surface accounts for this difference in the surface energies between the vacuum and argon environments, thus providing an explanation for the difficulty in graphitizing the C-face in argon. Apparently the C-face is more sensitive to this type of contamination than is the Si-face.

3.2.2 Purified Neon Environment

As argued in the previous section, graphitization in an argon environment is affected by unintentional oxidation, especially for the C-face. (The C-face appears to be more susceptible to oxidation than the Si-face, which we interpret in terms of the difference in structures for the two surfaces: the terminating layer on the Si-face is a $6\sqrt{3} \times 6\sqrt{3} - R30°$ reconstruction, which apparently has good stability and quite low energy, whereas the C-face is terminated in many cases with a 2×2 or 3×3 reconstruction, which appears to be less stable). Thus, to restrict the sublimation rate of Si, while simultaneously minimizing any unintentional oxidation, it is necessary to perform heating in a cleaner environment. We accomplished this utilizing cryogenically purified neon at 1 atm pressure. The vacuum chamber that we use for graphene preparation is actually a double-walled one. We flow liquid nitrogen between these two walls during the graphene preparation, and in this way any oxygen impurities in the neon stick to the walls of the chamber. (This procedure would not work for argon, since the argon itself will condense at the liquid-nitrogen temperature of 77 K).

At a test of this purified neon environment, we first prepared graphene on the *Si-face*. Figure 3.6 shows results for a Si-face sample prepared by heating at 1630 ºC in 1 atm of purified neon for 20 min. The surface morphology as shown in the AFM image of Fig. 3.6(a) consists of step bunches distributed over the surface, very similar to what occurs for preparation in argon [40]. The graphene thickness is found to be mainly 1 and 2 ML for this preparation condition, along with a few 3 ML areas (likely near the step edges), again similar to what occurs for argon. LEED patterns at 100 eV of this surface (not shown) are nearly identical to those seen for argon-prepared graphene, as in Fig. 3.2(b), with intense $6\sqrt{3}$ satellite spots surrounding the main SiC and graphene spots. These similarities between argon-prepared and neon-prepared samples again confirm that the Si-face is less susceptible to oxidation.

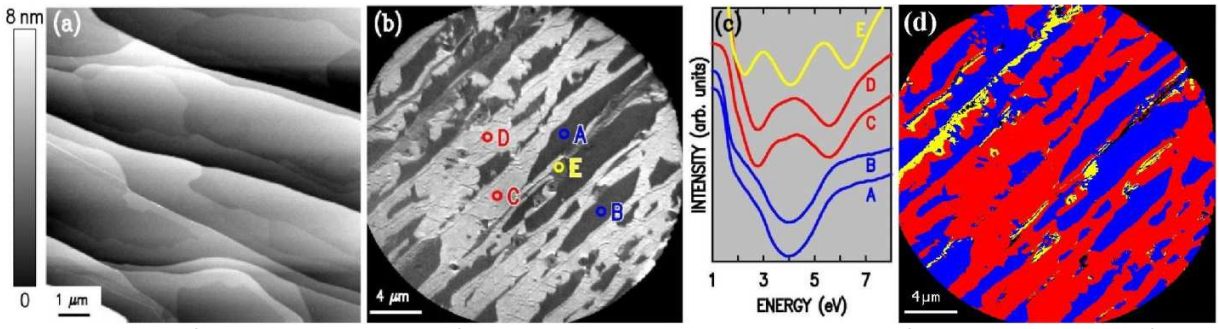

Fig. 3.6 Results for graphene on the Si-face, prepared by annealing at 1600 ºC for 20 min in 1 atm of neon. (a) AFM image, displayed with gray scale range of 8 nm. (b) LEEM image at beam energy of 3.8 eV. (c) Intensity of the reflected electrons from different locations marked in (b) as a function of electron-beam energy. (d) Color-coded map of local graphene thickness; the color blue, red, and yellow correspond to 1, 2, and 3 ML of graphene, respectively.

Graphitization on the *C-face* in the purified neon environment is then performed, and the results are shown in Fig. 3.7. Figure 3.7(a) shows an AFM image of the surface. One notable feature of the result of Fig. 3.7(a) is the network of raised (white) lines prominently seen in the figure. We attribute these ridges to the strain-induced features arising from the different thermal expansion coefficients between graphene and SiC [40]. As emphasized by Hass *et al*., the presence of such features is an indicator of a structurally ideal graphene film [17]. These ridges could be seen on most of the sample surface, indicating that the graphene films cover most of the surface uniformly, not as islands sitting on the surface. (These ridges appear somewhat broken up in some locations, but that effect follows the scan direction of the AFM and is surely an artifact of the scanning).

A LEEM image of this sample acquired at 4.0 eV is shown in Fig 3.7(b). Reflectivity curves from areas marked B – D in the LEEM image show 1, 2 or 3 minima, thus demonstrating that the surface is covered with graphene of 1, 2 or 3 layers. LEEM images from other locations of the sample show similar images, again indicating that most of the sample surface is covered by one or two layers of graphene, not islands of graphene as appear on the argon-prepared sample. As compared to the argon-prepared sample in Fig. 3.3, graphitization in purified neon environment eliminates the unintentional oxidation, leading to thinner and more uniform graphene films. We interpret this difference in terms of a cleaner environment. Our C-face work in argon displayed ample evidence for the existence of background oxygen during the graphene formation, and apparently the amount of oxygen is substantially lower in our purified neon environment.

It is important to note that the reflectivity curve A in Fig. 3.7(c) has a shape never before seen on vacuum-prepared samples [40], demonstrating that a new structure is present. We have found that these unique reflectively curves arise from a newly discovered graphene-like interface layer on the C-face. The formation of this interface layer will be discussed in detail in Chapter 4.

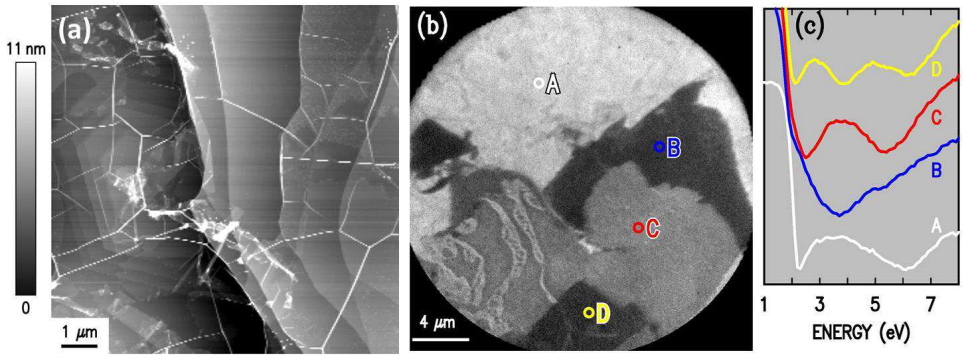

Fig. 3.7 Results for graphene on the C-face, prepared by annealing at 1450 ºC for 10 min in 1 atm of neon. (a) AFM image, displayed with gray scale range of 11 nm. (b) LEEM image at beam energy of 4.0 eV. (c) Intensity of the reflected electrons from different locations marked in (b) as a function of electron-beam energy.

3.2.3 Disilane Environment

As an alternative to the graphene preparation in argon or neon, we have also formed graphene in disilane on the C-face. The disilane (Si_2H_6) used here plays the role of Si source. At the temperatures and pressures used in our studies, disilane decomposes on the surface into Si and H. The advantage of using disilane is that the amount of Si near the surface could be tuned, since the disilane gas is introduced into our chamber by a leak valve. A low pressure of disilane was

used here, 5×10^{-5} Torr, but even so the annealing temperature needed for graphene formation was about 100 ºC higher than in vacuum and a much thinner film was formed on the surface. Graphitization using lower disilane pressure ($<5 \times 10^{-5}$ Torr) had been performed, but the results are quite similar to those prepared in vacuum. The surface morphology measured by AFM, as shown in Fig. 3.8(a), again displays raised lines (strain-induced ridges) on the surface, indicating the presence of structurally ideal graphene films [17]. An additional feature of our disilane-prepared samples is that, unlike the case for vacuum preparation, they do *not* display any nanocrystalline graphite (NCG) on their surface. Apparently the presence of the additional Si on the surface acts to provide an incorporation mechanism for that carbon.

The electron reflectivity curves C and D shown in Fig. 3.8(c) display a minimum near 3.5 eV, similar to that seen for vacuum-prepared films, but they also contain a minimum near 6.7 eV which is a new feature. This new feature is even more intensely seen (at 6.4 eV) for surface areas that do not display any simple oscillations over 2 – 7 eV, as shown by curves A and B of Fig. 3.8(c). Curves A and B are similar to curve A in Fig. 3.7(c), which are associated with a graphene-like interface layer. The formation of this interface layer will be discussed in detail in Chapter 4. What we can conclude from Fig. 3.8 is that graphitization of the C-face in a background of disilane leads to thinner and more uniform films at disilane pressure of about 5×10^{-5} Torr. As shown in Fig. 3.8(d), most of the surface is covered by uniform 1 ML of graphene (blue color).

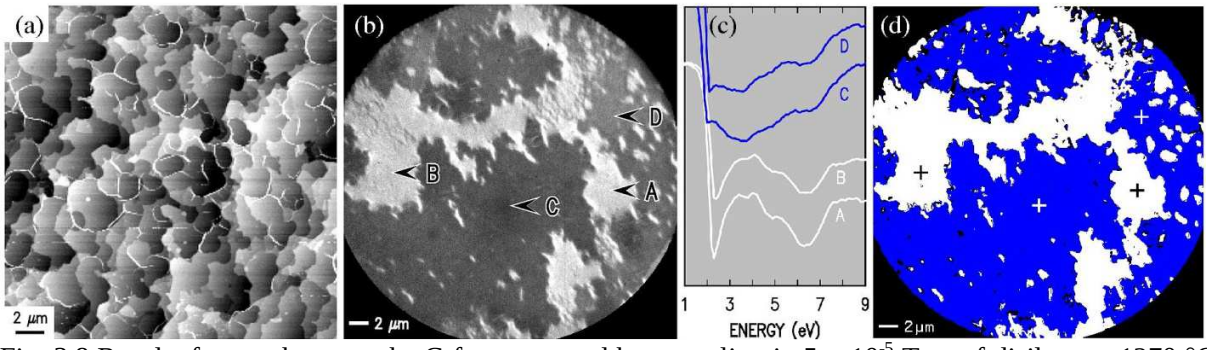

Fig. 3.8 Results for graphene on the C-face prepared by annealing in 5×10^{-5} Torr of disilane at 1270 °C for 15 min, producing an average graphene thickness of 0.64 ML. (a) AFM image, displayed using grey scale range of 3 nm, (b) LEEM image acquired at electron-beam energy of 4.5 eV. (c) Intensity of the reflected electrons from different regions marked in (b) as a function of electron-beam energy. (d) Color-coded map of local graphene thickness; blue corresponds to 1 ML of graphene, sitting on top of an interface layer denoted by white. Small white or black crosses mark the locations of reflectivity curves. (This data was obtained by Nishtha Srivastava from Prof. Feenstra's research group.)

3.3 Discussion

In contrast to the Si-face, the reproducibility between research groups regarding mode or growth morphology of graphene on the C-face is somewhat limited. Work of other groups revealed either islanding in the initial stages of the C-face graphene formation, or an apparent inhibition in the initial growth followed by rapid growth at temperatures above some critical temperatures [68, 128]. An important factor for graphene formation on the C-face is, we believe, the cleanliness of the surface (and surrounding environment). In our group, the presence of a silicate (Si_2O_3) on the C-face formed under argon is identified as being due to the unintentional oxidation. A number of the vacuum systems used by other groups for graphene formation under vacuum have only moderate base pressures (between 10^{-6} and 10^{-5} Torr) [17,68,128]. We believe that unintentional surface oxidation of the SiC (making it resistant to graphitization) is a significant factor in many of the previous reports.

The role of oxygen in our own observations of C-face graphene formation is definitely established by its characteristic signature in the intensity *vs*. voltage measurements of the $\sqrt{3} \times \sqrt{3} - \mathrm{R30°}$ LEED patterns, as shown in Fig. 3.5. Nevertheless, a direct measure of the partial pressure of oxygen during our argon-preparation procedure is lacking (such a measurement is difficult in the 1 atm argon environment). However, we have obtained indirect information about the presence of oxygen from the 1 atm *H environment* during our H-etching, with analogous results expected for the argon environment. To describe these results, we first note that the normal base pressure in our preparation system of 5×10^{-9} Torr is sufficiently low to prevent any significant oxidation of both the Si-face and the C-face surfaces, as revealed by the very faint (1/3,1/3) and (2/3,2/3) spots in Fig. 1.7(a) and Fig. 1.11(a). However, over a certain period of time we used our system under conditions of reduced pumping speed (when our 150 l/s main turbo pump was not operating) provided only by a 70 l/s load-lock pump with the valve to the load-lock left open. In that case our base pressure was significantly higher, about 2×10^{-7} Torr. Under these conditions the outgassing rate of the chamber walls was also significantly higher than usual; if the valve to the load-lock pump was closed (i.e. as done just prior to introducing H or Ar) then the chamber pressure rose to 2×10^{-5} Torr within a few seconds, whereas the rise for our normal operating conditions is more than an order-of-magnitude less

than that. Hence, under these conditions of reduced pumping, we have higher than usual oxygen partial pressures in the 1 atm H or Ar environments.

Performing surface cleaning by H-etching under these conditions of reduced pumping is found to yield relatively intense $\sqrt{3} \times \sqrt{3} - \mathrm{R30°}$ LEED spots on the H-etched surface (not shown). The (1/3,1/3) spots of those patterns have intensity greater than the (1,0) SiC spots, and even the (2/3,2/3) spots are clearly seen. Intensity versus energy analysis of these spots reveals that they do indeed arise from an oxidized surface [75]. Subsequent graphene formation at 1250 ºC on this sort of C-face surface yields *no graphene*, even though, for a nonoxidized SiC surface (i.e. made with our usual higher pumping speed), heating at the same temperature typically yields >4ML of graphene. Thus, the influence of an oxide layer on the surface is established once again, in agreement with our conclusions for the argon-prepared surfaces. Although we do not know the actual partial pressure of oxygen in the chamber during 1 atm H or Ar procedures, we do find that, for the conditions of restricted pumping in our preparation chamber, the resulting oxygen partial pressure is sufficiently high to cause the surface oxidation during both the H and Ar procedures.

For the Si-face, results for purified neon-prepared samples are in good agreement with the results employing argon, as shown in Fig. 3.1, Fig. 3.6, and in our previous reports [40,66]. The use of neon as compared with argon does not appear to significantly affect the situation for the Si-face. But for the C-face, our results using purified neon are in contrast to our work in argon: we find graphene with relatively uniform coverage over the surface using purified neon, whereas severe islanding of graphene occurred with argon. We interpret this difference in terms of a cleaner environment for the cryogenically purified neon. Apparently the amount of oxygen is substantially lower in our neon environment.

When we employ disilane for surface cleaning rather than H, we find that the resulting LEED patterns from the surface do *not* reveal any significant $\sqrt{3} \times \sqrt{3} - \mathrm{R30°}$ LEED pattern. This is the case even when restricted pumping of the preparation chamber (i.e. prior to, and during the disilane cleaning) is employed. We therefore suggest that the disilane (or Si) itself may act to scrub oxygen from the system, e.g. by the formation of volatile SiO_x species. This type of reaction may be significant in systems with only moderate or low vacuum environment,

such as the confined-controlled sublimation (CCS) process employed by de Heer and co-workers [129].

In the CCS process, a small SiC sample is graphitized while contained within a graphite container that is nearly closed except for a small hole in its cap [129]. The silicon pressure in the container during the heating is expected to be substantial, estimated at $\approx 10^{-3}$ Torr [129]. The resulting quality of the graphene layer appears to be quite good, both structurally and electronically [129]. However, to scale up the process to larger wafer sizes (and to ensure reproducibility between graphitization systems); one would like to perform this process in an open vacuum system with known partial pressures of the various gaseous constituents. It is this goal that we have pursued in the work described in this thesis. As mentioned in the previous paragraph, the chemical role of Si in the environment may be a significant one not only for its impact in reducing the Si sublimation rate, but also for its possible effect in maintaining an appropriate (i.e., reduced oxygen content) background gas.

3.4 Summary

We have studied the graphene formation on the Si-face under 1 atm of argon or 1 atm of purified neon. In both cases, as compared to vacuum-prepared samples, the samples prepared in argon or purified neon are found to have much larger domains of uniform graphene thickness. For nominally on-axis Si-face samples, the layer-by-layer growth mode is more firmly established, with the growth of a single monolayer of graphene over tens or hundreds of microns being relatively easy to achieve. For graphene prepared in the purified neon, results are in good agreement with the results employing argon, though the purified neon environment provides a cleaner environment. The graphene formed on the Si-face is found to be relatively insensitive to the preparation conditions (unlike the situation for the C-face), with this insensitive perhaps arising from the $6\sqrt{3}$ reconstruction of the surface forming a stable, low-energy surface termination.

One the C-face, graphitization occurs at a lower temperature than on the Si-face and so it is common to get thick (>10 ML) graphene films. To control this graphitization and hence achieve thinner films, we graphitized in 1 atm of argon, identical to the procedure on the Si-face. However, results on the C-face are quite different from that on the Si-face. Instead of uniform

layer-by-layer growth as seen on the Si-face we observed 3D formation of islands in the initial stage of graphene formation, with these islands growing relatively thick (≥5 ML) before complete graphene coverage is achieved. We attribute this islanding process to unintentional oxidation of the C-face in argon, which makes the surface resistant of graphitization (so that when the graphitization finally starts, it proceeds very quickly because of the elevated temperature). In contrast, for the neon-prepared C-face samples, we find graphene with relatively uniform coverage over the surface. We interpret this difference in terms of a cleaner environment. Our C-face work in argon displayed ample evidence for the existence of background oxygen during the graphene formation, and apparently the amount of that oxygen is substantially lower in our purified neon environment. For the C-face samples made in disilane we obtain films that are thinner and have a larger grain size than those made in vacuum.

Chapter 4

Interface Structure for Graphene on C-face SiC

4.1 Introduction

For graphene on SiC, it has been demonstrated that new graphene layers are formed *not* on top of existing ones, but rather, they form at *interface* between existing graphene layers and the underlying substrate [32]. Hence, the starting surface of SiC and the later interface structure between graphene films and SiC substrate play a crucial role for subsequent graphene formation.

To date the graphene/SiC interface on the Si-face is quite well understood: the interface consists of a graphene-like layer having $6\sqrt{3} \times 6\sqrt{3} - R30°$ symmetry (denoted $6\sqrt{3}$ for short), which is strongly bonded to the underlying SiC substrate [32,48,130,131]. This interface on the Si-face acts as a "buffer" layer between graphene films and SiC substrate and provides a template for subsequent graphene formation [32,48,130,131]. By the term *buffer layer* here, we mean a layer that has nearly the same structure as graphene, but is covalently bonded to the underlying material and therefore has different electronic structure than graphene. On the Si-face, a number of groups have succeeded in forming single-layer graphene, with good reproducibility between groups [17,31,39,66].

For the C-face, in contrast, the formation of interface structures and subsequent graphene films is found to be more complex than for the Si-face, for several reasons: (i) there exist more than one way to form graphene on the surface, i.e. more than one interface structure that has been observed between graphene and SiC substrate, (ii) the structural quality of graphene on the C-face is oftentimes much worse than for the Si-face, and (iii) employing an inert gas environment to improve the quality of graphene on the C-face is more problematic than for the Si-face. The reason for the latter issue was determined to be due to unintentional oxygen contamination of the inert gas (Ar), as discussed in Chapter 3.

Despite these complexities, one important aspect of graphene formation on the C-face to be noted is that several research groups have actually achieved very good quality graphene on this surface (better in certain respects than on the Si-face), albeit using growth conditions that are not so well understand [129,132]. Those growths are performed with the SiC sample in a confined space, so that a background Si pressure is formed near the surface, but the accurate value of this partial pressure is not known. To scale up the process to larger wafer sizes (and to ensure reproducibility between graphitization systems), one would like to perform this process in an open vacuum system with known partial pressures of the various gaseous constituents. With this

goal, the formation of graphene in an open vacuum system is studied by varying the formation conditions (sample temperature, T, and silicon pressure, P_{Si}).

In this chapter, we will demonstrate that, indeed, the interface between graphene and the C-face depends on the means of forming graphene. For formation in vacuum, we observe a 3×3 interface structure, in agreement with that seen by many other groups [17,32,76]. At relatively low P_{Si} (~5×10^{-6} Torr), the well-known $(2 \times 2)_C$ interface structure is found, consisting of 1/4 monolayer of Si adatoms on the surface [133,134]. The subscript "C" on the 2×2 label for this structure denotes that this reconstruction is more carbon rich than a different 2×2 structure that occurs on the same surface, but nevertheless it is Si (not C) adatoms that terminate this surface. When graphene is formed by using 5×10^{-5} Torr of disilane (or using 1 atm of purified neon), we find a new interface structure with $\sqrt{43} \times \sqrt{43} - R \pm 7.6°$ symmetry (denoted $\sqrt{43}$ for short). This interface structure is somewhat similar to the $6\sqrt{3}$ buffer layer for the Si-face, but with the supercell for the C-face being rotated by only ±7.6°, rather than 30°, relative to the SiC axes. We find that this new interface consists of a graphene-like layer that terminates the SiC crystal, analogous to the $6\sqrt{3}$ buffer layer on the Si-face, and hence we also use the term "buffer layer" to refer to this graphene-like layer on the C-face. When this $\sqrt{43}$ structure is oxidized, it changes to that of a graphene layer on top of a Si_2O_3 silicate layer. The graphene formed on this new interface is found to have higher quality than for graphene typically formed on the 3×3 or $(2 \times 2)_C$ interface.

4.2 Experimental Methods

Experiments are performed on nominally on-axis, *n*-type 6H-SiC or semi-insulating 4H-SiC wafers purchased from Cree Corp., with no apparent differences between results for the two types of wafers. The graphitization processes are similar to that described in Chapter 3 (section 3.1).

Characterization by low-energy electron diffraction (LEED) is performed *in situ* in a connected ultra-high-vacuum chamber. For quantitative LEED analysis, diffraction spot intensities were measured at different energies in the range of 100 eV to 300 eV. The analysis procedure is similar to that described in Section 3.1. After transferring the samples through air,

further characterization is performed using an Elmitec III low-energy electron microscope (LEEM).

4.3 Results

4.3.1 Structural models and preliminary diffraction results

Figure 4.1 shows structural models for the new interface structure that are the topic of this chapter: a graphene-like buffer layer on C-face SiC [Figs. 4.1(a) and (b)], and the same layer on a surface which has been oxidized [Figs. 4.1(c) and (d)]. The models shown in Fig. 4.1 are actually the conclusion of the detailed analysis in this chapter. However, we introduce them here in advance of that analysis in order to provide some definiteness to the structures that we will discuss. In Fig. 4.1(a), the graphene-like buffer layer is the topmost layer of the surface, with a carbon atom density and arrangement similar to that of graphene. The term "buffer layer", which we denote as "B", is used in Figs. 4.1(a) and (b) to refer to this graphene-like layer since it bonds to the underlying material. Actually, the precise interface structure between the graphene-like layer and the SiC is not known, as indicated by the box with question marks in Figs. 4.1(a) and (b). However, what *is* known is that the nature of the bonding between the graphene-like layer and the underlying SiC changes as a result of oxidation of the surface. As shown in Figs. 4.1(c) and (d), we find that after oxidation the SiC is terminated by a Si_2O_3 silicate and the graphene-like layer above that silicate is only weakly bonded to it. Hence, the graphene-like layer is *decoupled* from the underlying structure (analogous to what occurs on graphitized Si-face SiC [50,53,55,56]), and it becomes a regular graphene layer which we refer to as G_0 (with the subscript "0" referring to the fact that it originates from the graphene-like buffer layer). The structures in Figs. 4.1(b) and Fig. 4.1(d) have one additional graphene layer on top of the structures of Figs. 4.1(a) and (c), respectively. We denote this higher-lying graphene layer as G_1.

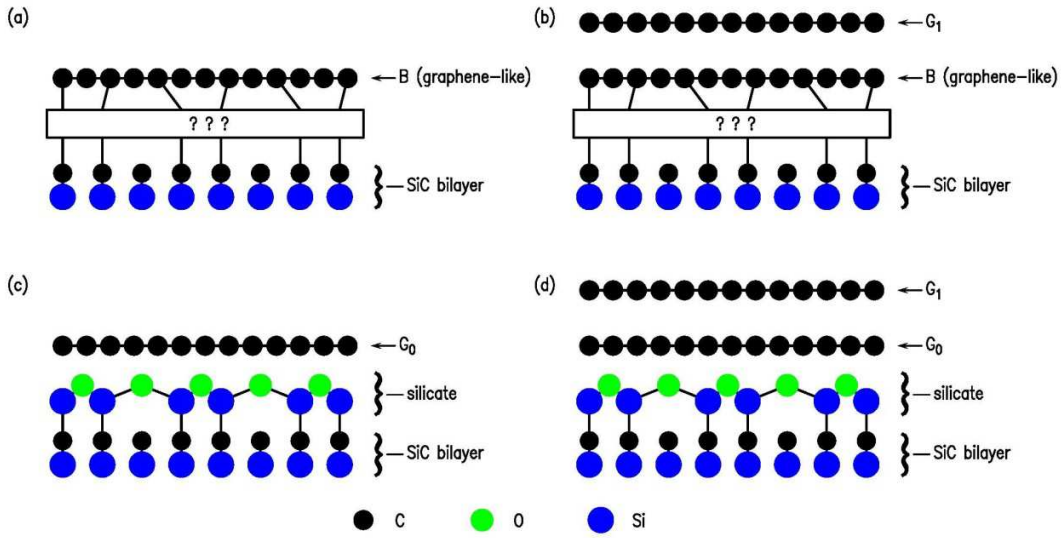

Fig. 4.1. Schematic view of the proposed models: (a) and (b) before oxidation, the graphene-like buffer layer (denoted as B) bonds to the underlying layer whose structure is not yet known; (c) and (d) after oxidation, the graphene-like layer decouples and becomes a graphene layer (denoted as G_0); a silicate layer with the form of Si_2O_3 appears between this graphene layer and the SiC substrate. Additional graphene layer on top of the graphene-like layer is denoted as G_1.

Figure 4.2(a) shows a LEED pattern acquired from an unoxidized surface, corresponding to Figs. 4.1(a) and (b). The pattern in Fig. 4.2(a) was obtained from a surface *in situ* immediately after graphene preparation, which is performed by heating the sample in 5×10^{-5} Torr of disilane at 1270 °C for 15 min. Weak graphene streaks are visible along with the primary SiC spots, as marked, and a complex arrangement of satellite spots forms around the latter. Analysis of these spots is shown in Fig. 4.2(a) [135,136]. The pattern can be perfectly indexed using a supercell on the SiC with edges extending along (6,-1) and (1,7) of the SiC 1 × 1 cells. In conventional notation this structure would be expressed as a matrix with columns (6,-1) and (1,7), and in a more compact notation we denote this structure as $\sqrt{43} \times \sqrt{43} - R \pm 7.6°$ (or $\sqrt{43}$ for short) with the $7.6° = tan^{-1}(\sqrt{3}/13)$ being the rotation of the supercell relative to the SiC. Approximately 8 × 8 unit cells of graphene fit within this supercell (with 2.4% mismatch, using room temperature lattice constants a_{SiC}=0.3080 nm and $a_{graphite}$=0.2464 nm). We interpret this complex pattern as indicating some distortion of the graphene-like layer and/or underlying SiC layer, due to bonding between the graphene-like layer and the SiC [48].

After this *in situ* study, the sample was exposed to air several days before introduced into the LEEM chamber. After introduction into the LEEM chamber it was outgassed at about 1000 ºC

for several minutes. This procedure caused the $\sqrt{43}$ pattern to disappear and a $\sqrt{3} \times \sqrt{3} - \mathrm{R30°}$ pattern to appear, as shown in Fig. 4.2(b). The same $\sqrt{3} \times \sqrt{3} - \mathrm{R30°}$ pattern was found on samples that were exposed to 1×10^{-5} Torr pure oxygen (rather than air) while heating to 1000 ºC. So, the $\sqrt{3} \times \sqrt{3} - \mathrm{R30°}$ pattern is an indication of oxidation of the surface.

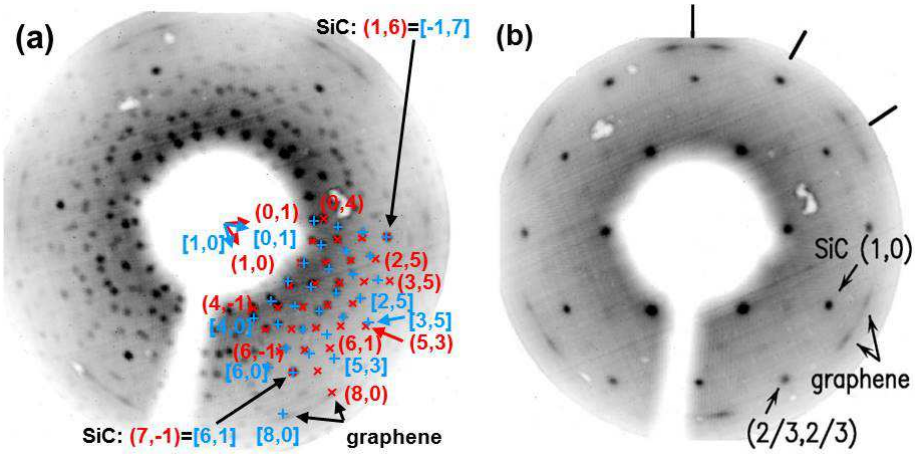

Fig. 4.2 LEED patterns obtained at 100 eV from 6H-SiC$(000\bar{1})$ surfaces: (a) LEED pattern obtained *in situ* from a sample heated in 5×10^{-5} Torr of disilane at 1270 ºC for 15 min, showing a complex LEED pattern with graphene streaks, (b) LEED pattern obtained from the same sample after oxidization, showing a $\sqrt{3} \times \sqrt{3} - \mathrm{R30°}$ pattern.

4.3.2 Detailed study of graphene on unoxidized SiC

Additional information comes from LEEM studies. In order to do LEEM measurements on the *bare* buffer layer (i.e. one that has not been oxidized); we prepared a sample and then transferred it from our graphene preparation chamber to the LEEM chamber in a relatively short time, ≈10 min, as opposed to the several hours or more used for other samples. Thus, we can study the buffer layer *before* any oxidation occurs.

Figure 4.3 shows results from this rapid transferred sample, prepared by heating in 5×10^{-5} Torr of disilane at 1220 °C for 10 min. The LEEM image at 3.8 eV shown in Fig. 4.3(a) consists predominantly of two types of areas, one with bright and the other with dark contrast. Measurements of the intensities of the reflected electrons as a function of their energy from locations marked in Fig. 4.3(a) are shown in Fig. 4.3(b). The reflectivity from the dark region (curves C and D) reveals a single minimum near 3.7 eV, as is typical for single-layer graphene [102]. The reflectivity from the bright region (curves A and B) shows behavior that we have

never observed previously on any C-face or Si-face sample, and we attribute them to the bare (unoxidized) buffer layer. Small areas of this surface consist of multilayer graphene, as in curves E and F, which reveal 2 and 4 ML of graphene, respectively.

Additional information is contained in the selected-area LEED (μ-LEED) results of Figs. 4.3(c) and (d). These patterns were acquired with a 5 μm aperture, at locations centered on the points A and C in Fig. 4.3(a). The size of that aperture is slightly larger than the areas of bright or dark contrast, respectively, surrounding those points, but data with a 2 μm aperture reveal the same diffraction spots (albeit with worse signal-to-noise) at these locations and at many other locations studied on the surface. At all locations, the patterns reveal spots with wavevector magnitude precisely equal to that of graphene.

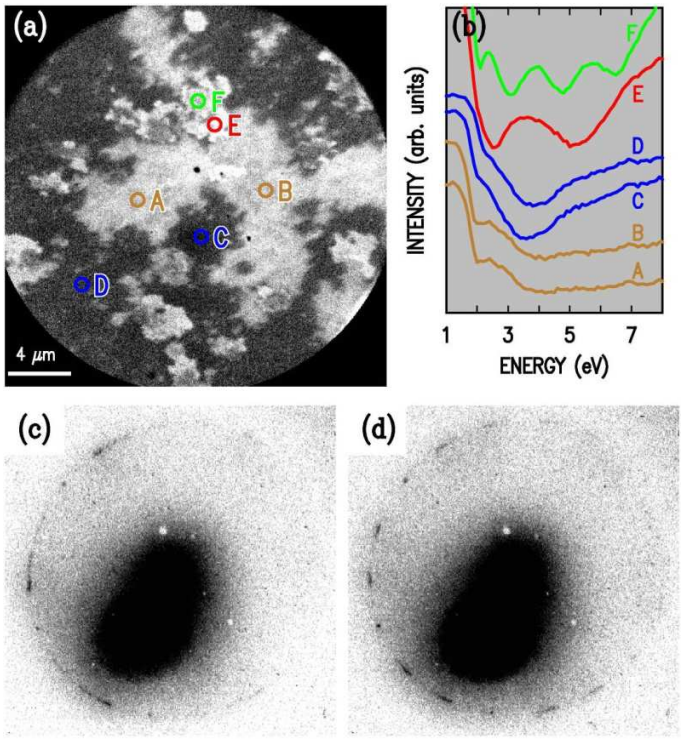

Fig. 4.3 Results for graphene on the C-face before oxidation. (a) LEEM image at beam energy of 3.8 eV. (b) Intensity of the reflected electrons from different locations marked in (a). (c) and (d) μ-LEED patterns acquired at 44 eV, using a 5 μm aperture centered at locations A (buffer layer) and C (1-ML graphene on buffer layer) in panel (a), respectively.

Based on the μ-LEED results, we can be certain that surface structure leading to the reflectivity curves A and B has the structure of graphene. We also know that it is the bottommost

graphene layer, i.e. directly in contact with SiC, since extensive studies both on this sample and many other samples reveal only thicker graphene or no graphene at all.

Immediately after the sample was produced, its LEED pattern acquired *in situ* at 100 eV revealed the $\sqrt{43}$ pattern (not shown), the same as that shown in Fig. 4.2(a). It should be noted that the $\sqrt{43}$ spots that appears in wide-area LEED patterns acquired at 100 eV from these unoxidized samples are not observed in the μ-LEED patterns of Figs. 4.3(c) and (d) acquired in the LEEM. We attribute this discrepancy to a reduced sensitivity of those diffraction intensities in the LEEM measurements, as further discussed in Section 4.4.

4.3.3 Detailed study of graphene on oxidized SiC

After the LEEM measurements reported in Fig. 4.3, the sample was removed from the LEEM instrument and oxidized by exposing it to air for several days. This oxidation caused the $\sqrt{43}$ spots to disappear (for other samples, we sometimes also observe the formation of $\sqrt{3} \times \sqrt{3} - R30°$ spots for the oxidized surface, but not for this particular sample, as further discussed in Section 4.4). LEEM results from the air-exposed surface are shown in Fig. 4.4. These LEEM images were not acquired from the same surface location as in Fig. 4.3 (due to difficulty in finding the same location), but nevertheless the surface of Fig. 4.4 was covered predominantly with areas of two different contrast levels, just as for Fig. 4.3, and we can confidently assign the two types of areas with the corresponding ones in Fig. 4.3.

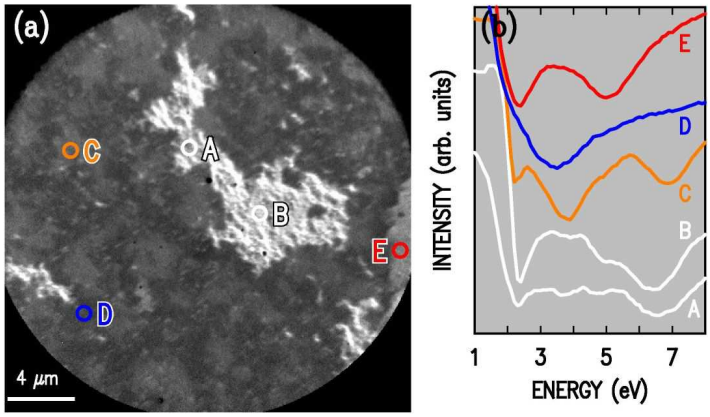

Fig 4.4 Results for the same sample in Fig. 4.3, after oxidation. (a) LEEM image at beam energy of 3.8 eV. (b) Intensity of the reflected electrons from different locations marked in (a).

The areas of bright and dark contrast can be seen in the LEEM image at 3.8 eV displayed in Fig. 4.4(a), although the dark areas now appear with two slightly different contrasts. Reflectivity curves from these dark regions, curves C and D of Fig. 4.4(b), reveal single-ML behavior (curve D) for the darkest contrast and single ML plus an additional minimum at 6.9 eV (curve C) for the slightly lighter contrast areas. The minimum at 6.9 eV is interpreted as forming because of "decoupling" of the buffer layer that is below the single-ML graphene (i.e., release of the covalent bonds between the buffer layer and the underlying SiC due to oxidation of the surface). The reflectivity curves (curves A and B) from the lighter-contrast areas reveal a broad maximum over 2 – 6 eV, along with a minimum near 6.6 eV. We associate the minima at 6.6 eV for curves A and B and the one at 6.9 eV for curve C with the same origin, i.e., some feature arising from the oxidation of the surface, which persists even with one (or more) graphene layer on top of the buffer layer.

4.3.4 In situ oxidation

As already discussed, the disilane-prepared surfaces (such as those shown in Fig. 4.4) are found to oxidize upon air exposure. To further elucidate this process, we describe experiments in which the oxidation is performed *in situ* in the LEEM, thus permitting study of a *fixed surface location* before and after oxidation. Our results are displayed in Fig. 4.5, acquired from a sample that was graphitized by heating in 1 atm of purified neon, after which it displayed a complex $\sqrt{43}$ LEED pattern identical to Fig. 4.2(a). The sample was then transferred through air into the LEEM, although rapid transfer was not employed in this case (the sample was exposed to air for four days before it was transferred into the LEEM chamber) so that much of the surface was oxidized. Nevertheless, some unoxidized areas remained, and for this sample we were able to study the same surface location before and after oxidation.

Immediately after introduction of the sample into the LEEM, data shown in Figs. 4.5(a) and (c) were obtained. Curves E and F of Fig. 4.5(c) in particular reveal single-layer graphene on an unoxidized interface. The surface was then exposed to 1×10^7 L of oxygen with the sample at ≈200 ºC, after which it was briefly heated to 1000 ºC. The surface areas from which the reflectivity curves E and F were acquired were modified by this procedure, producing reflectivity curves as shown in Fig. 4.5(d). Those curves show additional minima near 7.1 eV, similar to

curve C of Fig. 4.4(b). We thus find that these additional minima near 7.1 eV are indeed associated with oxidation of the interface.

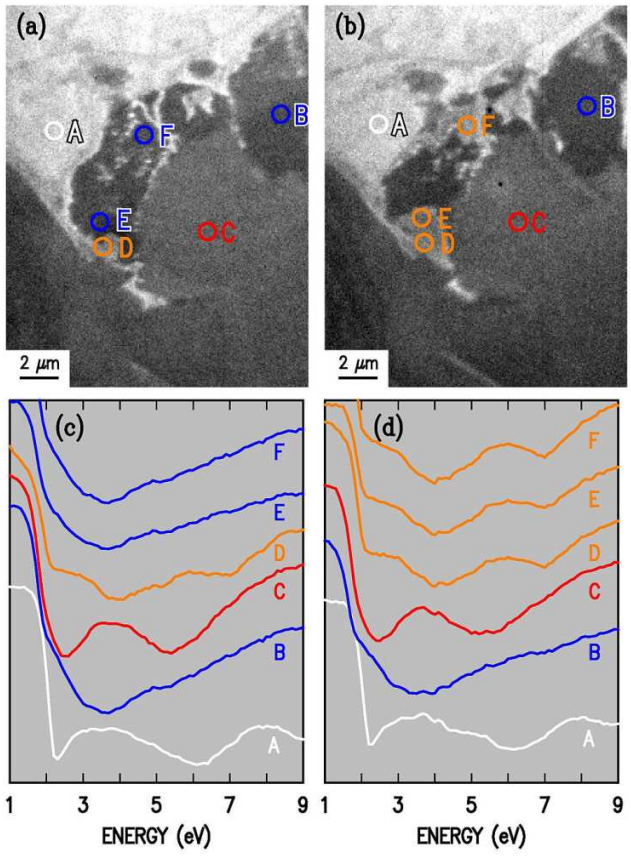

Fig. 4.5 Results for graphene on the C-face, prepared by heating in 1 atm of neon at 1450 ºC for 10 min. (a) and (b) LEEM images at 3.1 eV, before and after oxidation of the sample, respectively. (c) and (d) Reflectivity curves acquired from the circular areas marked in (a) and (b), respectively.

For this sample, immediately after the graphene formation in our preparation chamber, the characteristic $\sqrt{43}$ LEED pattern was observed, as shown in Fig. 4.6(a). After oxidation of the surface in the LEEM chamber, the $\sqrt{43}$ pattern disappeared and some $\sqrt{3}$ spots appeared, as seen in Fig. 4.6(b). This behavior is the same as for the disilane-prepared sample shown in Fig. 4.2. μ-LEED measurements of the oxidized surface, Figs 4.6(c) and (d), reveal spots with wavevector equal to that of graphene. A significant result here is that, on the buffer layer, the μ-LEED acquired with a 5 μm aperture reveals, in most cases, only a single sixfold arrangement of spots, as seen in Fig. 4.6(c). This result is in contrast to the disilane-prepared buffer layer, in which multiple orientations of the sixfold pattern are observed (Fig. 4.3). Thus, the crystallographic grain size for the neon-prepared graphene is found to be significantly larger than 5 μm. This is

the best structural result that we have found to date in any of our graphene prepared on the C-face.

It is also important to note that the orientation of the sixfold arrangement of spots in Fig. 4.6(c) is, judging from the 100 eV wide-area LEED result of Fig. 4.6(b), aligned at 30º relative to the primary (1,0) SiC spots (we further discuss this result in Section 4.4 and compare it to that recently obtained by other workers [129]). This result is in contrast to the rotational orientation of the graphene on top of the buffer, Fig. 4.6(d), for which a range of orientation angles is found, and with this range being centered on the same azimuth as the SiC spots (i.e., the usual orientation for C-face graphene [17]).

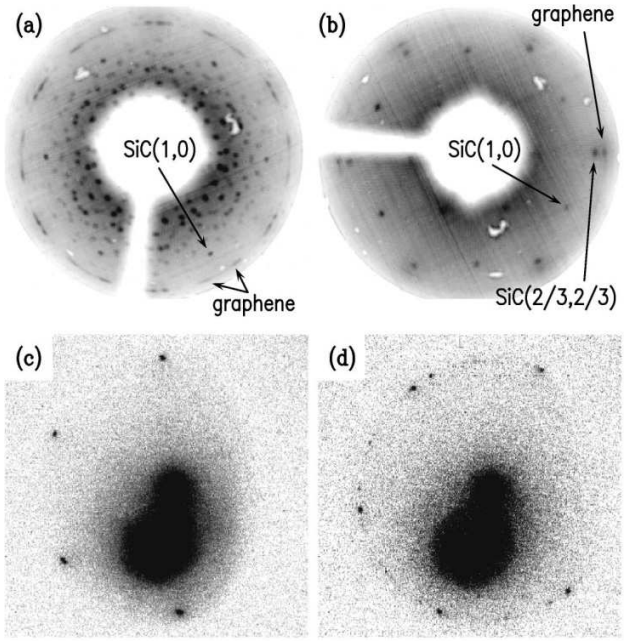

Fig. 4.6 (a), (b) LEED patterns at 100 eV, before and after further oxidation of the sample, respectively. (c), (d) µ-LEED patterns acquired after oxidation, with a 5 µm aperture at 44 eV, from the buffer layer and multilayer graphene on the buffer, respectively.

4.3.5 LEED I-V structure analysis

We would like to learn about the C-face interface structures both before and after oxidation, as characterized by the LEED patterns of Fig. 4.2. However, the LEED pattern for graphene before oxidation is very complex, being too complicated to permit dynamical LEED *I-V* analysis. For this reason, we focus on the pattern after oxidation of the sample (Fig. 4.2(b)). We have measured the *I-V* characteristics of the spots in that pattern, as shown by the solid lines in Fig. 4.7. LEED computation results, using a model consisting of one additional graphene layer on top

of one silicate (Si_2O_3) layer and six SiC bilayers, are shown by the dashed lines in Fig. 4.7. A $2\sqrt{3} \times 2\sqrt{3} - R30 \pm 6.59°$ graphene commensurate structure is used for the additional graphene layer. The structure of the silicate layer is the same as that used by Starke *et al.* [116], although we employ only the S3 stacking termination since we find that that produces the best fit with experiment (various terminations including fractional amounts of S1 and S2 have been tested, with the best fit obtained using >70% S3 termination). The graphene layer has initially a specified separation from the silicate, and the vertical coordinates of the graphene layer are then permitted to relax over distances of ±0.02 nm. The optimized *I-V* curves agree well with the experiment, yielding a relatively low *R*-factor of 0.18. This level of agreement between the experimental and calculated intensities provides the main evidence for the correctness of our structural models in Figs. 4.1(c) and (d): a silicate layer in the form of Si_2O_3 appears between the decoupled buffer layer and the SiC substrate. The separation between the decoupled buffer layer and the oxygen atoms of the silicate layer obtained from the calculation is 0.23 nm, although the *R*-factor is quite insensitive to this value. Our best determination of separation arises from a first-principles method for computing the reflectivity curves [103,104], where the separation between decoupled buffer and silicate layer is found, qualitatively, to be significantly less than the 0.33 nm separation between graphene layers.

Comparing the results of Fig. 4.7 and Fig. 3.5, which is from a bare oxidized C-face SiC, a noticeable difference of their *I-V* curves occurs for the intensity of the (4/3,1/3) beam, which, relative to the (1,0) beam, is much lower for the bare oxidized surface (Fig. 3.5) than for the graphene-covered surface (Fig. 4.7). Using integrated intensities of the measured intensities, the ratio of (4/3,1/3) intensity over (1,0) intensity is only about 0.05 for the bare oxidized SiC surface, while it is about 0.2 for the graphene-covered sample. The calculated curves display similar values for these ratios. It appears that the (4/3,1/3) beam is more or less forbidden for the bare oxidized surface, i.e. due to the symmetry of the precise atomic arrangement formed in that case. With one or more additional graphene layers on top, the symmetry changes, so that the (4/3,1/3) beam is much more intense from the graphene-covered surface. This approximate agreement in intensity ratio between the experimental and calculated intensities is another piece of evidence for the correctness of our structural model for the decoupled graphene-like buffer layer.

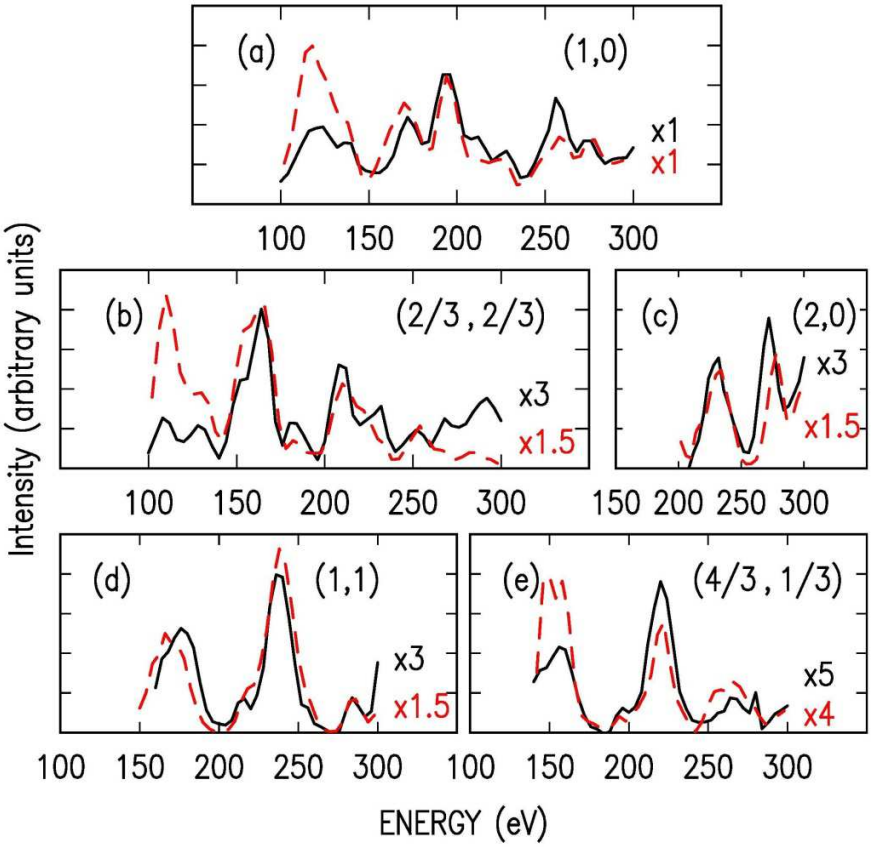

Fig. 4.7 Experimental LEED spot intensity spectra (solid line) obtained from the sample shown in Fig. 4.2(b). Dashed lines are spectra obtained from the theoretical calculations. Good agreement is obtained between the experimental and theoretical spectra, as manifested by the *R*-factor of 0.18.

4.3.6 Interpretation of the reflectivity curves

A first-principles method for computing the reflectivity curves is now available, and based on that we can now provide a more rigorous interpretation of the reflectivity curves discussed above [103,104].

For an unoxidized sample, we observe the bare buffer layer (B) together with areas of buffer layer plus graphene (B+G) and occasionally buffer layer plus 2 or 3 graphene layers (B+2G or B+3G). Similarly, for an oxidized sample, we observe areas of decoupled buffer layer which corresponds to a single graphene layer (G_0), together with areas of graphene on top of that (G_0+G) or areas with additional graphene layers. Fig. 4.8 shows a summary of these reflectivity curves, acquired from both unoxidized and oxidized samples.

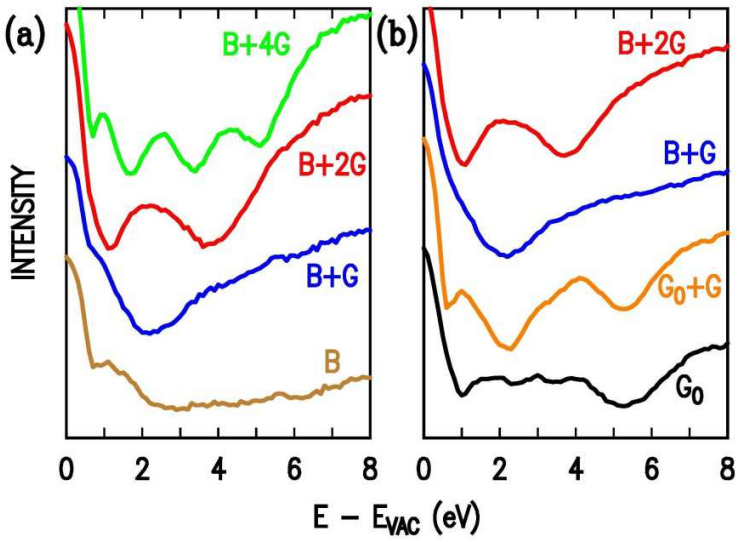

Fig. 4.8 Reflectivity curves from (a) unoxidized and (b) oxidized surfaces of graphene on C-face SiC. Curves are labeled according to graphene (G) or graphene-like buffer layer (B) present on the surface, with G_0 denoting the buffer layer that is decoupled from the SiC and forms a regular, pristine graphene layer. The curves have been shifted such that the vacuum level for each curve (as seen by the sharp increase in the reflectivity as a function of decreasing energy) is approximately aligned with zero energy.

These curves of Fig. 4.8 can be easily interpreted if we bear in mind the recent interpretation that the minima in the spectra arise from electronic states localized between the graphene layers or between the bottommost layer and the substrate [103,104,105]. For *n* graphene layers there are $n-1$ spaces between them and, hence, $n-1$ interlayer states. An additional state forms between the bottommost graphene layer and the substrate so long as the space between those is sufficiently large. Coupling (in a tight-binding sense) between all the interlayer states then produces a set of coupled states, and reflectivity minima are observed at the energies of these coupled states.

For example, the curve for the buffer (B) in Fig. 4.8(a) does not have any distinct minimum, since the buffer is relatively strongly bonded to the substrate and hence no interlayer state forms. For a layer of graphene on the buffer (B+G), a single state forms in the space between the buffer and the graphene and hence a single reflectivity minimum (at ≈2.1 eV) results. Similarly, two minima form for B+2G and three minima for B+3G, with these sets of minima all approximately centered around 2 eV.

Turning to the oxidized surface, Fig. 4.8(b), the buffer layer now decouples from the substrate (forming a *decoupled buffer* layer, G_0) so that an interlayer state forms, with energy

≈5.3 eV. The fact that this energy is higher than the 2.1 eV for the state between graphene layers indicates that the separation between the decoupled buffer and the substrate is *smaller* than that between two graphene layers (which is not surprising, since the graphene-graphene separation is likely close to a maximum interlayer separation considering the weak van der Waals bond between graphene layers) [103,104,105]. For a graphene layer on the decoupled buffer (G_0+G), there are interlayer states at about 2.1 and 5.3 eV, and these do not have large coupling (due to their relatively large energy difference) so that reflectivity minima are observed at nearly the same energies.

The upper two curves in Fig. 4.8(b) are essentially the same as the B+G and B+2G curves of Fig. 4.8(a) and they are labeled as such. For the B+G curve of Fig. 4.8(b), we always find some evidence of that along with the G_0+G curve on our oxidized surfaces, and we attribute the presence of the former simply to incomplete oxidation of the surface. For the case of the B+2G in Fig. 4.8(b), we cannot definitively distinguish that from a G_0+2G situation in which the bottommost interlayer state is not visible, but in any case for such spectra with two (or more) reflectivity minima centered around 2 eV we never observe any evidence of a higher reflectivity minimum near 5.3 eV. Interpreting such spectra as indeed arising from B+2G, it appears that oxidation of the SiC beneath multilayer graphene is more difficult than beneath single-layer graphene.

4.4 Discussion

We have obtained the $\sqrt{43}$ LEED pattern on several samples prepared in a Si-rich environment, utilizing either 5×10^{-5} Torr of disilane or 1 atm of neon environment, but never in vacuum. The differences between Si-face and C-face graphene/SiC interface structures are summarized in the following figure.

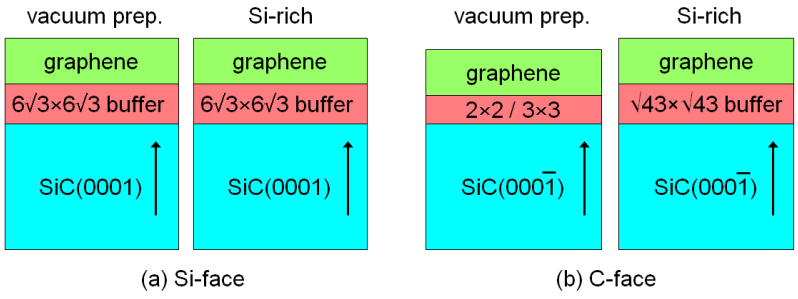

Fig. 4.9 (a) For the Si-face, the $6\sqrt{3}$ buffer layer forms at the interface under various preparation conditions. (b) For the C-face, the 3×3 and/or $(2 \times 2)_C$ structures form in vacuum, whereas the $\sqrt{43}$ buffer layer form at the interface in a Si-rich environment.

Regarding the reason for the different C-face interface structures in a Si-rich environment compared to vacuum, the graphene formation conditions in the former case are expected to be closer to equilibrium, as argued by Tromp and Hannon [85], so that kinetic limitations may lead to the absence of the $\sqrt{43}$ structure in vacuum-prepared C-face graphene. Graphitization in disilane at lower pressure ($<5 \times 10^{-5}$ Torr) has also been performed, but the results are somewhat similar to those of vacuum. Apparently, the formation of the $\sqrt{43}$ structure requires appropriate background gas (i.e. high enough Si partial pressure, reduced oxygen content). Graphitization in argon may also result in the formation of the $\sqrt{43}$ structure (it was also seen previously in small areas on an argon-prepared surface) as along as we can have an argon environment as clean as the purified neon environment. Complete geometrical determination of the $\sqrt{43}$ structure is still needed before a full understanding of its formation can be achieved.

For the pristine $\sqrt{43}$ structure, we find that μ-LEED reveals diffraction spots with the same wavevector magnitude as expected for perfect graphene. Thus, we conclude that the $\sqrt{43}$ structure is essentially a graphene layer, but one that is most likely covalently bonded to the underlying SiC. The covalent bonding distorts the graphene-like layer and results in the $\sqrt{43}$ LEED pattern. It should be noted, however, that the angle-resolved photoemission experiments for the Si-face that directly reveal the bonding and subsequent decoupling of the buffer layer from the Si-face SiC, Ref. 50, are not yet available for the C-face; such data would provide more complete evidence for our interpretation of our C-face results.

Although we have not determined the exact structure of the layer between the $\sqrt{43}$ graphene-like layer and the underlying SiC substrate, as represented by the box with question marks in Figs. 4.1(a) and (b), it is possible that this layer contains excess Si atoms compared with a SiC bilayer. Determining the stoichiometry of this interface immediately below the graphene-like layer is a crucial issue for the complete structural determination of the unoxidized C-face interface. In any case, during the subsequent graphene formation it is expected that the graphene-like layer becomes a new graphene layer and another graphene-like layer forms underneath it and bonds to the substrate, in the same way that graphene growth occurs on the Si-face [32].

After air exposure, with or without subsequent annealing in oxygen environment, the $\sqrt{43}$ pattern disappears and reflectivity spectra measured by LEEM change. As shown in Fig. 4.3 and Fig. 4.4, the reflectivity curves of that pristine buffer layer [curves A and B of Fig. 4.3(b)] are quite different than that after oxidation has occurred [curves A and B of Fig. 4.4(b)]. The general effect of the oxidation is seen to be the formation of a prominent minimum in the reflectivity near 6.6 eV. The minimum also occurs for graphene on top of the buffer layer, albeit shifted upwards by about 0.3 eV, as seen for single-layer-thick graphene on the buffer layer [curve C of Fig. 4.4(b)]. This transformation in the reflectivity curves has been observed repeatedly on several samples we prepared, and we interpret this transformation as arising from decoupling of the graphene-like buffer layer from the underlying SiC, analogously to what occurs for the $6\sqrt{3}$ buffer layer on the Si-face [50,53,55, 56].

In many cases we observe the $\sqrt{3} \times \sqrt{3} - \mathrm{R}30°$ LEED pattern to form after oxidation of the graphitized surface, but *not* always. We note that a significant variation from sample to sample is found in the efficacy with which the $\sqrt{3} \times \sqrt{3} - \mathrm{R}30°$ pattern forms. By comparing the detailed air/oxygen exposure and heating conditions for all our samples, it seems that $\sqrt{3} \times \sqrt{3} - \mathrm{R}30°$ pattern is more likely to form on samples with fewer graphene layers and with subsequent higher-temperature annealing. We therefore believe that in some cases oxidation has occurred, but the oxidized layer has not ordered sufficiently to form the $\sqrt{3} \times \sqrt{3} - \mathrm{R}30°$ structure. The formation of an ordered Si_2O_3 silicate layer under graphene requires right amount of Si and O atoms, and thick multilayer graphene may restrict the transport of O atoms through it. However, even on those samples *without* a $\sqrt{3} \times \sqrt{3} - \mathrm{R}30°$ pattern, reflectivity curves the same as those of Fig. 4.8(b) are obtained (i.e., including the G_0 and G_0 + G curves of Fig. 4.8(b) in particular), indicating that decoupling can occur even without the formation of an ordered silicate layer.

When oxidation of our C-face sample occurs, μ-LEED results from the buffer layer before and after oxidation are *unchanged*, as expected since that layer is essentially graphene. As noted in Fig. 4.3(c) and (d), those μ-LEED results are acquired at energies of around 44 eV or below, since at higher energies the diffraction spots observed in the LEEM broaden considerable and lose intensity. However, for the wide-area LEED patterns acquired with a conventional LEED apparatus, and displayed in this chapter at 100 eV, a change *is* observed before and after oxidation of the sample, namely, the $\sqrt{43}$ spots are present in the former case but absent in the

latter. We attribute this difference between the diffraction results of the LEEM compared to the conventional apparatus simply to the energy-dependence of the diffraction intensities (and also considering instrumental effects in the LEEM at the higher energies). Indeed, using the conventional LEED apparatus at lower energies, we find that the $\sqrt{43}$ spot intensities diminish as the energy is reduced from 100 eV, being very weak at energies below 60 eV. The disappearance of the $\sqrt{43}$ spots upon oxidation is interpreted, as mentioned earlier, in terms of a release of the covalent bonds between the graphene-like layer and the underlying SiC substrate.

The bonding and decoupling behavior of the graphene-like layer on the C-face is similar to that of the $6\sqrt{3}$ buffer layer on the Si-face. However, the behavior of the two surfaces is still different in some aspects. First, the $6\sqrt{3}$ buffer layer is quite stable and can survive under many environments, whereas even with just a few days of air exposure the $\sqrt{43}$ pattern will disappear. Second, since the $6\sqrt{3}$ buffer layer acts as a template for subsequent graphene formation, graphene layers do not have rotational disorder on the Si-face. However, we still get rotationally disordered graphene films on the C-face with the presence of a graphene-like layer, although the disorder is much less severe than for vacuum-prepared samples [41].

For single-layer graphene on the C-face of SiC, the group of de Heer and coworkers [129] reported a diffraction pattern consisting of sharp graphene spots located at positions rotated by 30º relative to the principal (1,0) SiC spots. We sometimes obtain a similar arrangement of graphene spots in our samples with reasonably sharp graphene spots along a 30º azimuth relative to the SiC spots, as shown in Fig. 4.6 (these types of graphene diffraction patterns are actually quite unusual on the C-face since, as just mentioned, the graphene spots more commonly are significantly broadened due to rotational disorder [17]). However, a significant difference in the patterns from our samples compared with those of de Heer *et al*. is that, after oxidation, our patterns display a $\sqrt{3} \times \sqrt{3} - \mathrm{R}30°$ pattern (or a $\sqrt{43}$ pattern before oxidation) whereas the pattern reported by de Heer *et al*. shows no such spots [129]. Hence, it appears that no ordered silicate layer is present on their samples. Further investigation of the graphene/SiC interfaces on their material (e.g., low-energy electron reflectivity measurement), compared with ours, is needed to further discern possible differences in the structures.

4.5 Summary

By preparing graphene on the C-face of SiC in a Si-rich environment, produced either by 5×10^{-5} Torr of disilane or using 1 atm of purified neon, a new interface structure with $\sqrt{43} \times \sqrt{43} - R \pm 7.6°$ symmetry is found to form between graphene layers and the underlying SiC substrate. Before oxidation of the surface, the bottommost graphene-like layer is bonded in some way to the SiC. After oxidation, this graphene-like layer decouples and becomes a graphene layer. This decoupling behavior is analogous to the decoupling of the $6\sqrt{3}$ buffer layer on the Si-face. After decoupling, an ordered Si_2O_3 silicate layer is found to usually form between the decoupled layer and the underlying SiC substrate (although the decoupling can also occur even without an *ordered* silicate layer, i.e. through the formation of what we believe to be a disordered oxide layer).

Chapter 5

Size, shape, and composition of InAs/GaAs quantum dots by scanning tunneling microscopy and finite-element calculation

5.1 Introduction

Semiconductor quantum dots (QDs) have been investigated extensively over the past decades [137], with InAs QDs grown on GaAs being one of the most commonly studied materials system. These self-assembled dots can be grown using molecular beam epitaxy (MBE) in the Stranski-Krastanow growth mode. Common experimental methods for studying QDs generally yield information on only structural characteristics (size, shape, and composition), e.g., using electron microscopy or x-ray diffraction, or on spectroscopic properties (energies of confined states), e.g., using low-temperature photoluminescence. However, the combination of scanning tunneling microscopy and spectroscopy (STM/S) can in principle yield information on both types of properties. Such measurements have the benefit of eliminating the inhomogeneous broadening that is inherent in measurements that average over the distribution of QDs in a sample. Nevertheless, prior STM/S studies have focused primarily on the structural [138,139,140,141,142] or the spectroscopic characteristics [143,144,145,146,147,148,149], with a complete determination of QD size, shape, composition, and electronic properties based solely on STM/S having not been reported.

To accurately model experimental data relating to QDs, it is important to develop a quantitative relationship between the QD size and the energy of its states. Two widely cited papers in the literature have developed theories of this sort, one based on nonlocal, empirical pseudopotentials [150], and the other on an eight-band $\boldsymbol{k} \cdot \boldsymbol{p}$ method [151]. Results for the two techniques generally agree in terms of the ordering and nature of the states, but the actual energies of the states for specific QD sizes differ significantly, for example, the energies of the lowest electron bound state differ by nearly a factor of 2 (subsequent work demonstrated that this discrepancy arose both from the parameters used in the computations as well as from the theoretical techniques *per se*) [152]. Comparison with experimental data for QDs of known size and shape is desirable in order to provide some measure of validation for the theories.

A prior study attempted such a comparison for lens-shaped QDs with base diameter of 25 nm and height 3.5 nm but lack of experimental knowledge on the composition of the QDs inhibited a parameter-free comparison [153]. A very recent study accomplished this type of comparison for InAs QDs with 24 nm base diameter and 7 nm height, by combining experimental results from STM and from optical spectroscopy, and this work then employed

theoretical predictions to fine-tune the QD structural parameters [154]. In contrast, in the present work we use STM/S measurements *alone* to extract both the structural and spectroscopic properties of QDs (albeit without the fine structural details as in Ref. 154), and we then employ these results as a test for the validity of the prior theoretical predictions for the binding energies of the QD states [155,156].

In this project, my own work focused on the determination of QD size, shape, and composition by comparison of measured STM data with finite-element calculations. The STM measurements themselves, along with STS measurements and associated modeling were accomplished by other group members. Hence, in this chapter I will focus on the determination of QD structural properties utilizing STM topographic data together with finite-element calculations.

5.2 Results

The InAs/GaAs QD structures were grown using solid source MBE [157]. On an *n*-type (001) oriented GaAs substrate, 200 nm of GaAs buffer layer was grown followed by five periods of InAs QDs. The QD layers were separated by 50 nm of GaAs. The superlattice was then capped with about 200 nm of GaAs overlayer. The GaAs buffer, spacer, and cap layers as well as the QDs were all nominally undoped. The GaAs was deposited at about 1 ML/s (ML=monolayer=0.28 GaAs thickness), with the wafer held at 580 ºC. The InAs for the QD layers was deposited at 0.27 ML/s (ML=0.30 nm InAs unstrained thickness) with the sample at 490 ºC, and using a deposition time of 10 s. This relatively large growth rate for the QDs is found to produce a high density of relatively small QDs, which lead to improved behavior of infrared focal plane arrays made with similarly grown QDs [158].

Cross-sectional STM (XSTM) measurements were performed at room temperature in an ultrahigh vacuum chamber with base pressure $<5 \times 10^{-11}$ Torr. Samples were cleaved *in situ* to expose atomically flat (110) surfaces for subsequent STM and scanning tunneling spectroscopy (STS) measurements. Commercial Pt-Ir tips were cleaned *in situ* by electron bombardment prior to use. Images are acquired with a constant current of 0.1 nA and at sample-tip voltages specified below.

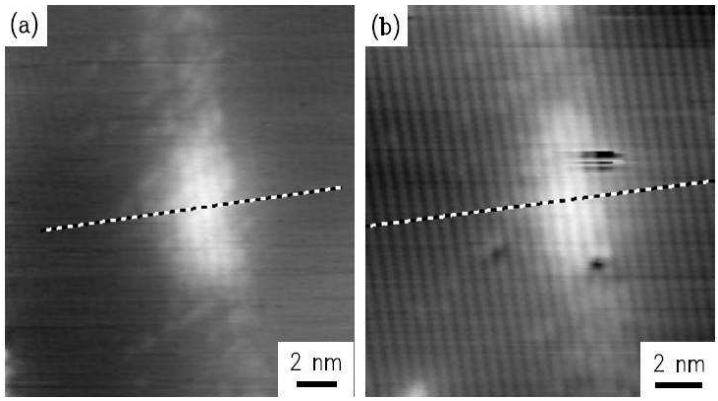

Fig. 5.1 STM images of two QDs, showing location of topographic cuts through each QD. Growth direction is from right to left across each image. Both images were acquired with sample voltage of -2 V, and are displayed with gray scale ranges of (a) 0.26 and (b) 0.24 nm. (Data was acquired by Sandeep Gaan of Prof. Feenstra's research group.)

Figure 5.1 shows two representative STM images of our QDs. The QDs appear bright in the images because, after cleavage, they relax outwards due to the strain arising from the 7% lattice mismatch between InAs and GaAs. We find a cross-sectional shape consistent with a truncated pyramid, a truncated cone, or a lens (section of a sphere), similar to that found by prior workers [159,160]. Further definition of the QD shape can be obtained using the methodology of Bruls *et al.* [159] in which the measured cross-sectional heights are plotted as a function of the measured cross-sectional base length, as shown in Fig. 5.2. The maximum base length along the $[1\bar{1}0]$ direction and height along the [001] direction are seen to be $b = 10.5 \pm 0.5$ nm and $h = 2.9 \pm 0.2$ nm, respectively (this height includes the wetting layers). The distribution is seen to be consistent with 3D dot shapes of either a truncated cone or a lens shape, and we use the latter for further analysis. For this lens shape, the radius of the corresponding sphere is $R = [(b/2)^2 + h^2]/(2h) = 6.20$ nm, and the maximum angle of the sidewall to the base is 57.8º. The occurrence of this type of shape, for small QDs such as ours, is well explained in a work of Eisele *et al*. [160]

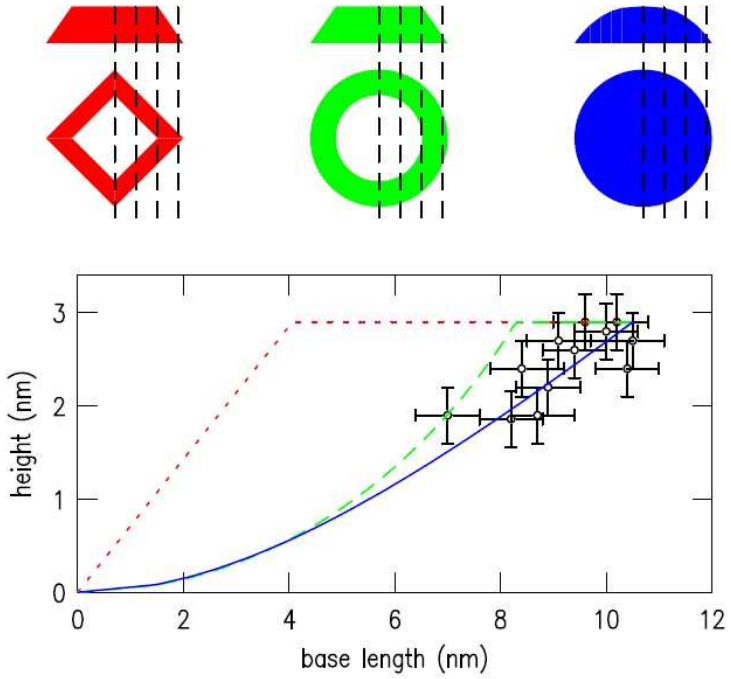

Fig. 5.2 Distribution of QD base lengths and heights, compared to theory for various shapes of the dots: truncated trapezoid—dotted line; truncated cone—dashed line; and lens shape—solid line. The shapes are pictured in the upper part of the figure, together with a few possible locations of the cleavage plane.

Topographic cuts through the QDs from Fig. 5.1(a) and (b) are shown in Fig. 5.3. These two QDs have cross-sections that are among the largest of any that we have studied, so that we can be confident that the cleavage plane has passed nearly through the center of the QDs. Assuming that electronic contributions to the images are small [161], this cut can be compared to the results of finite-element analysis (continuum mechanics, including anisotropic effects [162]) accomplished by using COMSOL software for a strained QD that is elastically relaxed at the cleavage surface. We consider our lens geometry with variable In composition x of the $In_xGa_{1-x}As$ QD. At the same time, we match to data for the distance between corrugation maxima (local lattice parameter), shown in Fig. 5.3(b), measured along the same cut through the QDs as for the surface displacement of Fig. 5.3(a). We match the experimental data with finite-element computations made using a lens shape in the *unstrained* geometry with dimensions of $b = 9.5$ and $h = 2.6$ nm which correspond to, after strain, a distorted lens shape with $b = 9.8$ and $h = 2.6$ nm. We find agreement between experiment and theory for a linearly-graded In composition pictured in Fig. 5.3(a), varying from $x = 0.65$ at the bottom of the QD to $x = 0.95$ in the middle and back to $x = 0.65$ at the top of the QD.

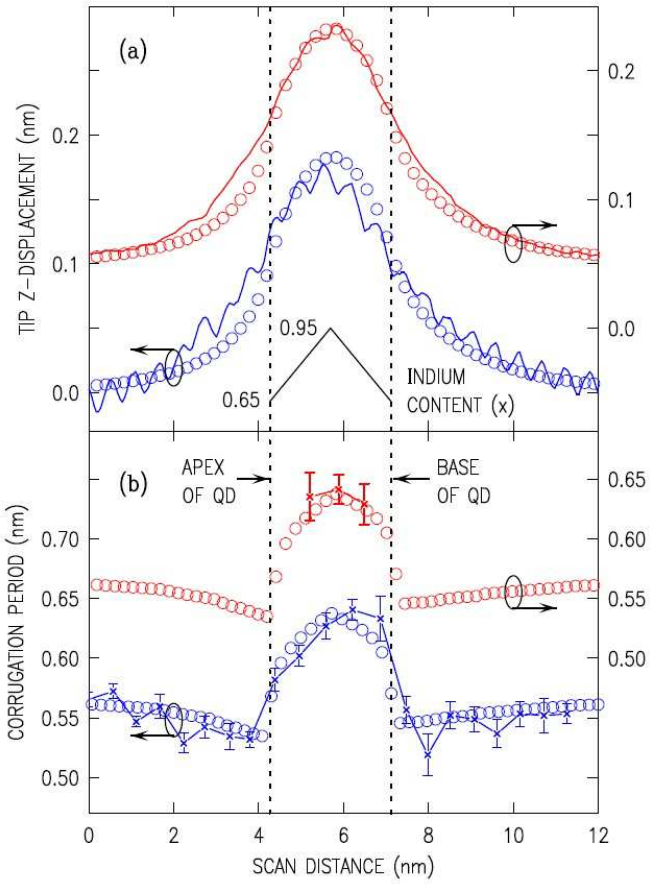

Fig. 5.3 (a) Cross-sectional topographic cuts and (b) corrugation period (local lattice parameter), measured along the dashed lines in Figs. 5.1(a) and (b) (upper and lower data sets, respectively). Experimental results are shown by solid lines, and results of finite-element computation by circles. The inset in (a) shows the step-graded composition profile for the QD used in the computations.

The simultaneous fitting of the data in Figs. 5.3(a) and (b) provide strong constraints on the In composition. The average *x*-value (averaged over the [001] direction) of 0.80 is determined to an accuracy of a few percent and the grading of the *x*-value of 0.21 nm^{-1} is determined with an accuracy of around 20% – 30%. Prior works have indicated a grading profile that is much less steep in the lower part of the QD than the upper part [154,159,163]. Our results are not inconsistent with that (i.e. at the limit of three times our estimated error range), although they favor the symmetric grading just mentioned. Separately, we note that for both data sets in Fig. 5.3(a) the experimental data are slightly higher than the finite-element results for spatial locations ≈1 nm above the apex of the QDs. We speculate that this discrepancy could arise from the presence of some excess In located in the GaAs *above* the QD, although we have not further investigated this possibility.

5.3 Summary

In summary, we have employed STM to probe the structure of InAs QDs in GaAs. Cross-sectional imaging, together with the finite-element calculations, permits a determination of the shape of the dots (lens-shaped, with maximum size of 10.5 nm base length and 2.9 nm height). Comparison between the STM data and the calculation results of the displacement of the dot profile out from the cleavage surface, together with observation of its local lattice parameter, leads to an accurate determination of the cation composition as varying from 65% indium at the base of the QD to 95% at its center and back to 65% at its apex.

Chapter 6

Summary

In this thesis we studied epitaxial graphene produced by thermal decomposition of SiC. Earlier studies on graphitization of SiC focused on UHV annealing of SiC, while my study focuses on graphene formation under three environments: 1 atm of argon, 1 atom of cryogenically purified neon and a low-pressure background of disilane. In this chapter we summarize our results.

6.1 Morphology of graphene on SiC prepared in argon, neon or disilane

On the Si-face, as compared to vacuum-prepared samples, we found improvements in the morphology of graphene films in all three environments. The presence of argon, neon or disilane gas decreases Si sublimation rate, thus increasing the temperature required for graphene formation. The higher graphitization temperature enhances the mobility of diffusing species, which in turn results in an improved morphology of the graphene films. The samples prepared in all three environments are found to have much larger domains of uniform graphene thickness. It is quite easy to produce a single ML extending over 10's or 100's of μm on the surface, with longer annealing (or higher temperatures) presumably leading to a second ML, etc.

One the C-face, the same procedures as used for the Si-face are employed. However, results on the C-face are quite different than for the Si-face. When argon-annealing is employed, instead of uniform layer-by-layer growth as seen on the Si-face we observed thick islands of graphene in the initial stage of graphene formation, which we attribute to unintentional oxidation of the surface. When annealing in cryogenically purified neon is employed (cleaner than the argon environment), we eliminated the unintentional oxidation and obtained relatively uniform graphene films. Use of a low-pressure background of disilane yields a similar improvement, i.e. a single layer of graphene over 10's or 100's μm is easy to produce.

6.2 Interface structure for graphene on SiC

Since interface structures have much effect on the structural and electrical properties of graphene films on top of them, much attention has been paid to interface structures between graphene films and the underlying SiC substrate in my study.

On the Si-face, we find that for all environments (including vacuum environment) the interface structure is a graphene-like structure but with some additional structural elements (five-fold and seven-fold carbon rings), forming $6\sqrt{3} \times 6\sqrt{3} - R30°$ unit cell [131]. Since this layer is

strongly bonded to the SiC below, it is considered as a buffer layer. As additional Si is sublimated from the sample, this buffer layer eventually converts to pristine graphene and a new buffer layer forms below it. A LEED image and a schematic structural model for the $6\sqrt{3} \times 6\sqrt{3} - R30°$ reconstruction and graphene on top are shown in Fig. 6.1.

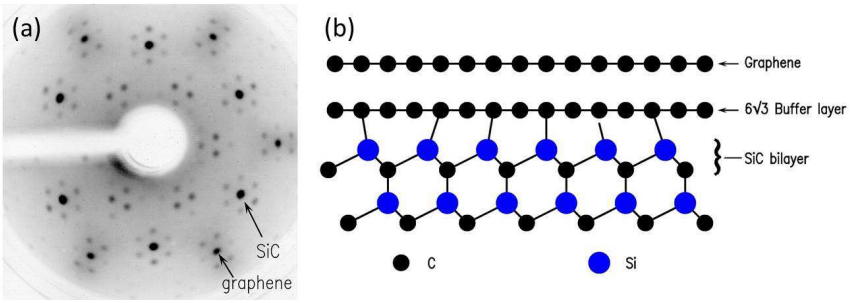

Fig. 6.1 (a) A LEED pattern at 100 eV shows a $6\sqrt{3} \times 6\sqrt{3} - R30°$ pattern. The 6 fold satellite spots around the SiC and graphene spots arise from the $6\sqrt{3} \times 6\sqrt{3} - R30°$ reconstruction. (b) Side view of the $6\sqrt{3} \times 6\sqrt{3} - R30°$ reconstruction. Lines are drawn between the buffer layer and the topmost Si atoms on SiC to indicate that the buffer layer is strongly bonded to the substrate.

On the C-face, the situation is found to be more complex than for the Si-face: more than one interface structure that has been observed, depending on the preparation conditions.

In vacuum, the 3×3 reconstruction is often found. A detailed model for this reconstruction has recently been proposed in a theoretical study by L. Nemec *et al* [164]. This 3×3 structure is an energetically stable structure, and it exists before graphene formation. Subsequent graphene forms on top of the 3×3 structure, covering it like a carpet, with relatively weak interaction between the graphene and the 3×3 structure. A LEED image and a schematic model for the 3×3 structure and graphene are shown in Fig. 6.2.

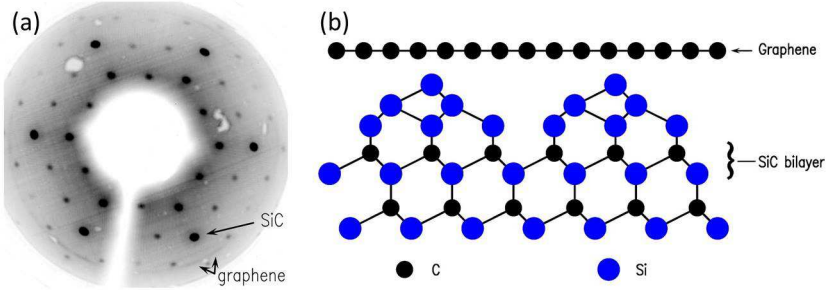

Fig. 6.2 (a) A LEED at 100 eV shows a 3×3 pattern. (b) Side view of the 3×3 reconstruction. No lines are drawn between the graphene layer and the reconstruction because they are weakly bonded.

At relatively low P_{Si} ($\approx 10^{-6}$ Torr), the $(2 \times 2)_C$ reconstruction is found, consisting of Si adatoms on T_4 sites terminating the SiC bilayer. The subscript "C" on the 2×2 label denotes that this reconstruction is more carbon rich than a different 2×2 structure that occurs on the same surface; nevertheless, it is important to realize that this $(2 \times 2)_C$ structure is in fact *Si-rich* compared to a terminating SiC bilayer, i.e. it contains 1/4 ML of excess Si atoms on the surface. A LEED image and a structure model for the $(2 \times 2)_C$ reconstruction and graphene are shown in Fig. 6.3.

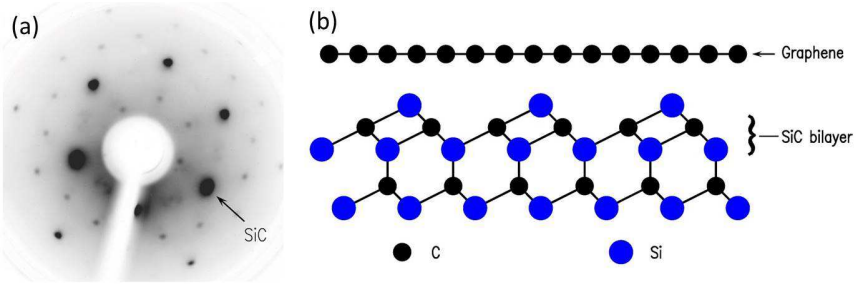

Fig. 6.3 (a) A LEED pattern at 100 eV shows a 2×2 pattern. (b) Side view of the $(2 \times 2)_C$ reconstruction. It consists of Si adatoms on T_4 sites terminating the SiC bilayer. No lines are drawn between the graphene layer and the reconstruction because they are weakly bonded.

In chapter 4, we have reported on the formation of graphene on the C-face under conditions of higher P_{Si} than occurs for the $(2 \times 2)_C$ or the 3×3 surfaces. Specifically, for a pressure of 5×10^{-5} Torr, we observed that the first C-layer to form is a graphene-like layer having a $\sqrt{43} \times \sqrt{43} - R \pm 7.6°$ symmentry. Although the precise atomic geometry of this graphene-like layer and the layers underneath it was not determined, we can certainly expect that it contains more excess Si atoms than for the 1/4 ML situation of the $(2 \times 2)_C$ structure. A LEED image and a schematic model for the interface structure are shown in Fig. 6.4. Whether or not the graphene-like layer is strongly bonded to the underneath structure or weakly bonded is not clearly known. We do know however, as discussed in chapter 4, that oxidation of the surface produces a silicate layer with weakly-bonded graphene above it, and furthermore we know experimentally from low-energy electron reflectivity (LEER) measurements that the graphene-like layer prior to the oxidation is considerably more strongly bonded to the underlying structure than after the oxidation. So we find that there is a not-so-weak interaction between the graphene-like layer and the structure underneath it. This interaction produces a better rotational alignment of the graphene on the surface than for vacuum-prepared graphene on the C-face (hence, larger

domains of single-thickness graphene), but most likely the bonding is not as great as for the $6\sqrt{3} \times 6\sqrt{3} - R30°$ structure on the Si-face.

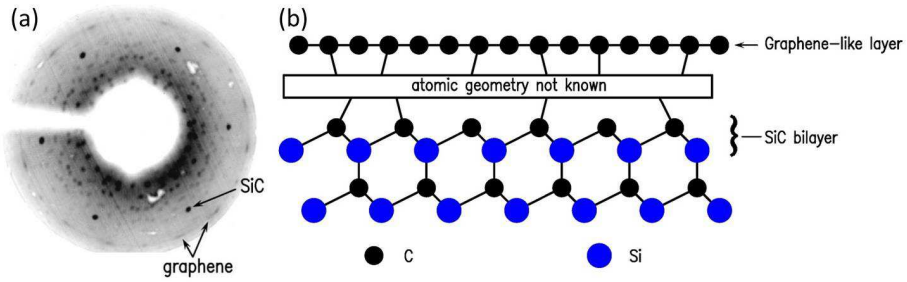

Fig. 6.4 (a) A LEED pattern at 100 eV shows a $\sqrt{43} \times \sqrt{43} - R \pm 7.6°$ pattern. (b) Side view of the $\sqrt{43} \times \sqrt{43} - R \pm 7.6°$ structure. Few lines are drawn between the graphene-like layer and the structure underneath it, indicating a not-so-weak interaction.

1 A. K. Geim and K. S. Novoselov, Nature Mater. **6**, 183-191 (2007).

2 N. D. Mermin, Phys. Rev. **176**, 250-254 (1968).

3 K. S. Novoselov, D. Jiang, F. Schedin, T. J. Booth, V. V. Khotkevich, S. V. Morozov, and A. K. Geim, Proc. Natl. Acad. Sci. U.S.A. **102**, 10451 (2005).

4 K. S. Novoselov, A. K. Geim, S. V. Morozov, D. Jiang, Y. Zhang, S. V. Dubonos, I. V. Grigorieva, and A. A. Firsov, Science **306**, 666 (2004).

5 Y. Zhang, Yan-Wen Tan, H. L. Stormer, and P. Kim, Nature **438**, 201 (2005).

6 K. S. Novoselov, A. K. Geim, S. V. Morozov, D. Jiang, M. I. Katsnelson, I. V. Grigorieva, S. V. Dubonos, and A. A. Firsov, Nature **438**, 197 (2005).

7 Y.-M. Lin, A. Valdes-Garcia, S.-J Han, D. B. Farmer, I. Meric, Y. Sun, Y. Wu, C. Dimitrakopoulos, A. Grill, P. Avouris, and K. A. Jenkins, Science **332**, 1294 (2011).

8 L. Liao, J. Bai, R. Cheng, Y.-C. Lin, S. Jiang, Y. Qu, Y. Huang, and X. Duan, Nano Lett. **10**, 3952-3956 (2010).

9 Y.-M. Lin, C. Dimitrakopoulos, K. A. Jenkins, D. B. Farmer, H.-Y. Chiu, A. Grill, and Ph. Avouris, Science **327**, 662 (2010).

10 M. I. Katsnelson, *Graphene: Carbon in Two Dimensions*, Cambridge University Press (2012).

11 W. Choi, and J.-W. Lee, *Graphene: Synthesis and Applications*, CRC press (2011).

12 S. Reich, J. Maultzsch, and C. Thomsen, Phys. Rev. B **66**, 035412 (2002).

13 E. Konstantinova, S. O. Dantas, and Paulo M. V. B. Barone, Phys. Rev. B **74**, 035417 (2006).

14 T. Ohta, A. Bostwick, T. Seyller, K. Horn, and E. Rotenberg, Science **313**, 951 (2006).

15 J. W. Gonzalez, H. Santos, M. Pacheco, L. Chico, and L. Brey, Phys. Rev. B **81**, 195406 (2010).

16 K. Nakada, and M. Fujita, Phys. Rev. B **54**, 17954 (1996).

17 J. Hass, W. A. de Heer, and E. H. Conrad, J. of Phys.: Condens. Matter **20**, 323202 (2008).

18 L. Jiao, X. Wang, G. Diankov, H. Wang, and H. Dai, Nature Nanotechnology **5**, 321-325 (2010).

19 G. Xin, W. Hwang, N. Kim, S. M Cho, and H. Chae, Nanotechnology **21**, 405201 (2010).

20 R. Murali, *Graphene Nanoelectronics, From Materials to Circuits*, Springer (2012).

21 X. Lu, M. Yu, H. Huang, and R. S Ruoff, Nanotechnology **10**, 269-272 (1999).

22 B. Jayasena, S. Subbiah, Nanoscale Research Letters **6**, 95 (2011).

23 Y. Zhang, L. Zhang, and C. Zhou, Acc. Chem. Res. **46**(10), 2329-2339 (2013).

24 A. Reina, X. Jia, J. Ho, D. Nezich, H. Son, V. Bulovic, M. S. Dresselhaus, and J. Kong, Nano Lett. **9**, 1 (2009).

25 I. Vlassiouk, P. Fulvio, H. Meyer, N. Lavirk, S. Dai, P. Datskos, S. Smirnov, Carbon 54, 58-67 (2013).

26 Neil W. Ashcroft, and N. David Mermin, *Solid State Physics*, Cengage Learning (1976).

27 P. Sutter, Nature Mater. **8**, 171 (2009).

28 J. Hass, F. Varchon, J. E. Millan-Otoya, M. Sprinkle, N. Sharma, W. A. de Heer, C. Berger, P. N. First, L. Magaud, and E. H. Conrad, Phys. Rev. Lett. **100**, 125504 (2008).

29 W. J. Choyke, H. Matsunami, G. Pensl, *Silicon Carbide: Recent Major Advances*, Springer (2004).

30 D. K. Gaskill, G. G. Jernigan, P. M. Campbell, J. L. Tedesco, J. C. Culbertson, B. L. VanMil, R. L. Myers-Ward, C. R. Eddy, Jr. J. Moon, D. Curtis, M. Hu, D. Wong, C. McGuire, J. A. Robinson, M. A. Fanton, J. P. Stitt, T. Stitt, D. Snyder, X. Wang, and E. Frantz, ECS Transactions, **19**(5) 117-124 (2009).

31 K. V. Emtsev, A. Bostwick, K. Horn, J. Jobst, G. L. Kellogg, L. Ley, J. L. McChesney, T. Ohta, S. A. Reshanov, J. Röhrl, E. Rotenberg, A. K. Schmid, D. Waldmann, H. B. Weber, and T. Seyller, Nature Mater. **8**, 203 (2009).

32 K. V. Emtsev, F. Speck, Th. Seyller, and L. Ley, Phys. Rev. B **77**, 155303 (2008).

33 K.-K. Lew, B. L. VanMil, R. L. Myers-Ward, R. T. Holm, C. R. Eddy, Jr. and D. K. Gaskill, Mater. Sci. Forum **556-557**, 513-516 (2007).

34 B. L. VanMil, K.-K. Lew, R. L. Myers-Ward, R. T. Holm, D. K. Gaskill, C. R. Eddy Jr., L. Wang, P. Zhao, J. Cryst. Growth **311**, 238-243 (2009).

35 S. Nie, C. D. Lee, R. M. Feenstra, Y. Ke, R. P. Devaty, W. J. Choyke, C. K. Inoki, T. S. Kuan, and Gong Gu, Surf. Sci. **602**, 2936-2942 (2008).

36 J. A. Robinson, K. A. Trumbull, M. LaBella III, R. Cavalero, M. J. Hollander, M. Zhu, M. T. Wetherington, M. Fanton, and D. W. Snyder, Appl. Phys. Lett. **98**, 222109 (2011).

37 W. A. de Heer, C. Berger, X. Wu, P. N. First, E. H. Conrad, X. Li, T. Li, M. Sprinkle, J. Hass, M. L. Sadowski, M. Potemski, and G. Martinez, Sol. St. Comm **143**, 92-100 (2007).

38 Luxmi, S. Nie, P. J. Fisher, R. M. Feenstra, G. Gu, and Y. Sun, J. Electron. Mater. **38**, 6 (2009).

39 Luxmi, N. Srivastava, R. M. Feenstra, and P. J. Fisher, J. Vac. Sci. Technol. B **28**(4) (2010).

40 Luxmi, N. Srivastava, Guowei He, R. M. Feenstra, and P. J. Fisher, Phys. Rev. B **82**, 235406 (2010).

41 N. Srivastava, Guowei He, Luxmi, P. C. Mende, R. M. Feenstra, and Y. Sun, J. phys. D: Appl. Phys. **45,** 154001 (2012).

42 A. J. Van Bommel, J. E. Crombeen and A. Van Toore, Surf. Sci. **48**, 463-472 (1975).

43 C. Berger, Z. Song, T. Li, X. Li, A. Y. Ogbazghi, R. Feng, Z. Dai, A. N. Marchenkov, E. H. Conrad, P. N. First , and W. A. de Heer, J. Phys. Chem. B **108**, 19912-19916 (2004).

44 I. Forbeaux, J.-M. Themlim, and J. -M. Debever, Phys. Rev. B **58**, 16396 (1998).

45 Th. Seyller, K. V. Emtsev, K. Gao, F. Speck, L. Ley, A. Tadich, L. Broekman, J. D. Riley, R. C. G. Leckey, O. Rader, A. Varykhalov, and A. M. Shikin, Surf. Sci. **600**, 3906 (2006).

46 W. Lu, P. Krüger, and J. Pollmann, Phys. Rev. B **61**, 13737 (2000).

47 J. Bernhardt, J. Schardt, U. Starke, and K. Heinz, Appl. Phys. Lett **74**, 1084 (1999).

48 C. Riedl, U. Starke, J. Bernhardt, M. Franke, and K. Heinz, Phys. Rev. B **76**, 245406 (2007).

49 K. V. Emtsev, Th. Seyller, F. Speck, L. Ley, P. Stojanov, J. D. Riley, and R. G. C. Leckey, Mater. Sci. Forum **556-557**, 525-528 (2007).

50 C. Riedl, C. Coletti, T. Iwasaki, A. A. Zakharov, and U. Starke, Phys. Rev. Lett. **103**, 246804 (2009).

51 C. Riedl, C. Coletti, and U. Starke, J. Phys. D: Appl. Phys. **43**, 374008 (2010).

52 F. Speck, J. Jobst, F. Fromm, M. Ostler, D. Waldmann, M. Hundhausen, and H. B. Weber, Appl. Phys. Lett. **99**, 122106 (2011).

53 S. Oida, F. R. McFeely, J. B. Hannon, R. M. Tromp, M. Copel, Z. Chen, Y. Sun, D. B. Farmer, and J. Yurkas, Phys. Rev. B **82**, 041411(R) (2010).

54 S. Watcharinyanon, L. I. Johansson, A. A. Zakharov, and C. Virojanadara, Surf. Sci. **606**, 401-406 (2012).

55 C. Virojanadara, S. Watcharinyanon, A. A. Zakharov, and L. I. Johansson, Phys. Rev. B **82**, 205402 (2010).

56 K. V. Emtsev, A. A. Zakharov, C. Coletti, S. Forti, and U. Starke, Phys. Rev. B **84**, 125423 (2011).

57 C. Xia, S. Watcharinyanon, A. A. Zakharov, R. Yakimova, L. Hultman, L. I. Johansson, and C. Virojanadara, Phys. Rev. B **85**, 045418 (2012).

58 I. Gierz, T. Suzuki, R. T. Weitz, D. S. Lee, B. Krauss, C. Riedl, U. Starke, H. Höchst, J. H. Smet, C. R. Ast, and K. Kern, Phys. Rev. B **81**, 235408 (2010).

59 A. Charrier, A. Coati, T. Argunova, F. Thibaudau, Y. Garreau, R. Pinchaux, I. Forbeaux, J.-M. Debever, M. Sauvage-Simkin, and J.-M. Themlin, J. of Appl. Phys. **92** (5), 2479-2484 (2002).

60 T. Ohta, A. Bostwick, J. L. McChesney, T. Seyller, K. Horn, and E. Rotenberg, Phys. Rev. Lett. **98**, 206802 (2007).

61 P. Mallet, F. Varchon, C. Naud, L. Magaud, C. Berger, and J.-Y. Veuillen, Phys. Rev. B **76**, 041403(R) (2007).

62 J. B. Hannon, and R. M. Tromp, Phys. Rev. B. **77** 241404(R) (2008).

63 G. Gu, S. Nie, R. M. Feenstra, R. P. Devaty, W. J. Choyke, W. K. Chan, and M. G. Kane, Appl. Phys. Lett. **90**, 253507 (2007).

64 C. Riedl, A. A. Zakharov, and U. Starke, Appl. Phys. Lett. **93**, 033106 (2008).

65 I. Langmuir, Phys. Rev. **34**, 6 (1912).

66 C. Virojanadara, M. Syväjarvi, R. Yakimova, and L. I. Johansson, Phys. Rev. B **78**, 245403 (2008).

67 J. L. Tedesco, B. L. VanMil, R. L. Myers-Ward, J. C. Culbertson, G. G. Jernigan, P. M. Campbell, J. M. Mc Crate, S. A. Kitt, C. R. Eddy Jr., and D. K. Gaskill, ECS Transaction **19**(5), 137-150 (2009).

68 J. L. Tedesco, G. G. Jernigan, J. C. Culbertson, J. K. Hite, Y. Yang, K. M. Daniels, R. L. Myers-Ward, C. R. Eddy, Jr., J. A. Robinson, K. A. Trumbull, M. T. Wetherington, P. M. Campbell, and D. K. Gaskill, Appl. Phys. Lett. **96**, 222103 (2010).

69 G. L. Greeth, A. J. Strudwick, J. T. Sadowski, and C. H. Marrows, Phys. Rev. B **83**, 195440 (2011)

70 Luxmi, P. J. Fisher, N. Srivastava, R. M. Feenstra, Y. Sun, J. Kedzierski, P. Healey, and G. Gu, Appl. Phys. Lett. **95**, 073101 (2009).

71 A. C. Ferrari, and J. Robertson, Phys. Rev. B **61**, 20 (2000).

72 N. Camara, G. Rius, J.-R. Huntzinger, A. Tiberj, L. Magaud, N. Mestres, P. Godignon, and J. Camassel, Appl. Phys. Lett. **93**, 263102 (2008).

73 N. Camara, J.-R. Huntzinger, G. Rius, A. Tiberj, N. Mestres, F. Pérez-Murano, P. Godignon, and J. Camassel, Phys. Rev. B **80**, 125410 (2009).

74 N. Camara, A. Tiberj, B. Jouault, A. Caboni, B. Jabakhanji, N. Mestres, P. Godignon, and J. Camassel, J. Phys. D: Appl. Phys. **43**, 374011 (2010).

75 U. Starke, J. Schardt, J. Bernhardt, and K. Heinz, J. Vac. Sci. Technol. A **17**, 1688 (1999).

76 F. Hiebel, P. Mallet, F. Varchon, L. Magaud, and J-Y. Veuillen, Phys. Rev. B **78**, 153412 (2008).

77 U. Starke and C. Riedl, J. Phys.: Condens. Matter **21**, 134016 (2009).

78 J. Bernhardt, M. Nerding, U. Starke, and K. Heinz, Mater. Sci. Eng. B **61-62**, 207-211 (1999).

79 I. Forbeaux, J.-M. Themlin, A. Charrier, F. Thibaudau, and J.-M. Debever, Appl. Surf. Sci. **162-163**, 405-412 (2000).

80 I. Forbeaux, J.-M. Themlin, and J.-M. Debever, Surf. Sci. **442**, 9-18 (1999).

81 Th. Seyller, A. Bostwick, K. V. Emtsev, K. Horn, L. Ley, J. L. McChesney, T. Ohta, J. D. Riley, E. Rotenberg, and F. Speck, Phys. Stat. Sol. (b) **245**, 7, 1436-1446 (2008).

82 A. Seubert, J. Bernhardt, M. Nerding, U. Starke, and K. Heinz, Surf. Sci. **454-456**, 45-48 (2000).

83 F. Hiebel, P. Mallet, J.-Y. Veuillen, and L. Magaud, Phys. Rev. B **83**, 075438 (2011).

84 X. Weng, J. A. Robinson, K. Trumbull, R. Cavalero, M. A. Fanton, and D. Snyder, Appl. Phys. Lett. **100**, 031904 (2012).

85 R. M. Tromp, and J. B. Hannon, Phys. Rev. Lett. **102**, 106104 (2009).

86 J. Park, Guowei He, R. M. Feenstra, and An-Ping Li, Nano Lett. **13**, 3269-3273 (2013).

87 K. W. Clark, X.-G. Zhang, I. V. Vlassiouk, Guowei He, R. M. Feenstra, and An-Ping Li, ACS Nano **7**, 7956 (2013).

88 K. W. Clark, X.-G. Zhang, G. Gu, J. Park, Guowei He, R. M. Feenstra, and An-Ping Li, Phys. Rev. X **4**, 011021 (2014).

89 V. Ramachandran, M. F. Brady, A. R. Smith, R. M. Feenstra, and D. W. Greve, J. Electron. Mater. **27**, 4 (1998).

90 K. Oura, V. G. Lifshifts, A. A. Saranin, A. V. Zotov, M. Katayama, *Surface Science*, Springer (2003).

91 H. Lüth, *Solid Surface, Interfaces and Thin Films*, Springer (2001).

92 M. A. Van Hove, W. H. Weinberg, C. M. Chan, *Low-energy Electron Diffraction*, Springer (1986).

93 V. Blum, K. Heinz, Computer Physics Communications **134**, 392-425 (2001).

94 J. B. Pendry, J. Phys. C **13**, 937 (1980).

95 E. G. McRae, Surf. Sci. **8** 14-34 (1967).

96 M. A. Van Hove, S. Y. Tong, *Surface Crystallography by LEED: Theory, Computation, and Structure Results*, Springer (1979).

97 E. Bauer, Rep. Prog. Phys. **57**, 895-938 (1994).

98 E. Bauer, Ultramicroscopy **17**, 51-56 (1985).

99 R. M. Tromp, IBM J. Res. Develop. **44**, 503 (2000).

100 Elmitec manual, Low-energy electron microscope, Model LEEM III.

101 L. H. Veneklasen, Rev. Sci. Instrum. **63**, 5513 (1992).

102 H. Hibino, H. Kageshima, F. Maeda, M. Nagase, Y. Kobayashi, and H. Yamaguchi, Phys. Rev. B **77**, 075413 (2008).

103 R. M. Feenstra, N. Srivastava, Q. Gao, M. Widom, B. Diaconescu, T. Ohta, G. L. Kellogg, J. T. Robinson, and I. V. Vlassiouk, Phys. Rev. B **87**, 041406(R) (2013).

104 N. Srivastava, Q. Gao, M. Widom, and R. M. Feenstra, Phys. Rev. B **87**, 245414 (2013).

105 R. M. Feenstra and M. Widom, Ultramicroscopy **130**, 101-108 (2013).

106 M. Posternak, A. Baldereschi, A. J. Freeman, E. Wimmer, and M. Weinert, Phys. Rev. Lett. **50**, 761 (1983).

107 Luxmi, PhD Thesis, Department of Physics, Carnegie Mellon University (2010).

108 N. Srivastava, PhD Thesis, Department of Physics, Carnegie Mellon University (2012).

109 P. J. Fisher, Luxmi, N. Srivastava, S. Nie, and R. M. Feenstra, J. Vac. Sci. & Tech. A **28**, 958 (2010).

110 G. Binning, C. F. Quate, Ch. Gerber, Phys. Rev. Lett. **56**, 9 (1986).

111 F. J. Giessibl, Rev. Mod. Phy. **75**, 949 (2003).

112 N. A. Geisse, Materials Today **12**, 7-8 (2009).

113 L. Huang, G. V. Hartland, L.-Q. Chu, Luxmi, R. M. Feenstra, C. Lian, K. Tahy, and H. Xing, Nano Lett. **10**, 1308 (2010).

114 S. Shivaraman, M. V. S. Chandrashekhar, J. J. Boeckl, and M. G. Spencer, J. Electron. Mater. **38**, 725 (2009).

115 C. Virojanadara, R. Yakimova, J. R. Osiecki, M. Syväjärvi, R. I. G. Uhrberg, L. I. Johansson, and A. A. Zakharov, Surf. Sci. **603**, L87-L90 (2009).

116 U. Starke, J. Schardt, J. Bernhardt, and K. Heinz, J. Vac. Sci. Technol. A **17**, 1688 (1999).

117 J. B. Hannon, and R. M. Tromp, Phys. Rev. B **77** 241404(R) (2008).

118 F. Owman, and P. Mårtensson, Sur. Sci. **369**, 126-136 (1996).

119 G. M. Rutter, N. P. Guisinger, J. N. Grain, E. A. A. Jarvis, M. D. Stiles, T. Li, P. N. First, and J. A. Stroscio, Phys. Rev. **B 76**, 235416 (2007).

120 S. Nie, and R. M. Feenstra, J. Vac. Sci. & Technol. A **27**, 1052 (2009).

121 J. Hass, J. E. Millán-Otoya, P. N. First, and E. H. Conrad, Phys. Rev. **B 78**, 205424 (2008).

122 H. Hibino, S. Mizuno, H. Kageshinma, M. Nagase, and H. Yamaguchi, Phys. Rev. B **80**, 085406 (2009).

123 J. Hass, R. Feng, T. Li, X. Li, Z. Zong, W. A. de Heer, P. N. First, E. H. Conrad, C. A. Jeffrey, and C. Berger, Appl. Phys. Lett. **89**, 143106 (2006).

124 L. B. Biedermann, M. L. Bolen, M. A. Capano, D. Zemlyanov, and R. G. Reifenberger, Phys. Rev. B **79**, 125411 (2009).

125 H. Hibino, H. Kageshima, F. Maeda, M. Nagase, Y. Kobayashi, Y. Kobayashi, and H. Yamaguchi, e-J. Surf. Sci. Nanotechnol. **6**, 107 (2008).

126 J. Schardt, J. Bernhardt, U. Starke, and K. Heinz, Surf. Rev. Lett. 5, 181-186 (1998).

127 D. Schmeißer, D. R. Batchelor, R. P. Mikalo, P. Hoffmann, and A. Lloyd-Spetz, Appl. Surf. Sci. **184**, 340-345 (2001).

128 G. Prakash, M. A. Capano, M. L. Bolen, D. Zemlyanov, R. G. Reifenberger, Carbon **48**, 2383-2393 (2010).

129 W. A. de Heer, C. Berger, M. Ruan, M. Sprinkle, X. Li, Y. Hu, B. Zhang, J. Hankinson, and E. Conrad, Proc. Natl. Acad. Sci. U.S.A. **108**, 16900 (2011).

130 C. Riedl, C. Coletti and U. Starke, J. Phys. D: Appl. Phys. **43**, 374009 (2010).

131 Y. Qi, S. H. Rhim, G. F. Sun, M. Weinert, and L. Li, Phys. Rev. Lett. **105**, 085502 (2010).

132 N. Camara, B. Jouault, A. Caboni, B. Jabakhanji, W. Desrat, E. Pausas, C. Consejo, N. Mestres, P. Godignon, and J. Camassel, Appl. Phys. Lett. **97**, 093107 (2010).

133 A. Seubert, J. Bernhardt, M. Nerding, U. Starke, K. Heinz, Surf. Sci. **454**, 45 (2000).

134 F. Hiebel, P. Mallet, J.-Y. Veuillen, and L. Magaud, Phys. Rev. B **83**, 075438 (2011).

135 N. Srivastava, Guowei He, Luxmi, and R. M. Feenstra, Phys. Rev. B **85**, 041404(R) (2012).

136 A correction to the LEED pattern of Fig. 4.1(a) has been performed to account for distortion in the wavevector scale: new wavevectors k' are computed from old ones k according to $(k'/k_{max}) = (k/k_{max})^{1.1}$ where k_{max} is the maximum observed wavevector. This same

correction when applied to Si-face data yields excellent results for the known spot locations of the $6\sqrt{3}$ pattern on that surface.

137 D. Bimberg, M. Grundmann, and N. N. Lendentsov, Quantum Dot Heterostructures (Wiley, New York, 1998).

138 B. Lita, R. S. Goldman, J. D. Phillips, and P. K. Bhattacharya, Appl. Phys. Lett. **74**, 2824 (1999).

139 H. Eisele, O. Flebbe, T. Kalka, C. Preinesberger, F. Heinrichsdorff, A. Krost, D. Bimberg, and M. Dähne-Preitsch, Appl. Phys. Lett. **75**, 106 (1999).

140 J. H. Blokland, M. Bozkurt, J. M. Ulloa, D. Reuter, A. D. Wieck, P. N. M. Koenraad, P. C. M. Christianen, and J. C. Maan, Appl. Phys. Lett. **94**, 023107 (2009).

141 D. M. Bruls, J. W. A . M. Vugs, P. M. Koenraad, H. W. M. Salemink, J. H. Wolter, M. Hopkinson, M. S. Skolnick, F. Long, and S. P. A. Gill, Appl. Phys. Lett. **81**, 1708 (2002).

142 H. Eisele, A. Lenz, R. Heitz, R. Timm, M. Dähne, Y. Temko, T. Suzuki, and K. Jacobi, J. Appl. Phys. **104**, 124301 (2008).

143 T. Yamauchi, Y. Matsuba, L. Bolotov, M. Tabuchi, and A. Nakamura, Appl. Phys. Lett. **77**, 4368 (2000).

144 B. Legrand, B. Grandidier, J. P. Nys, D. Stiévenard, J. M. Gérard, and V. Thierry-Mieg, Appl. Phys. Lett. **73**, 96 (1998).

145 T. Maltezopoulos, A. Bolz, C. Meyer, C. Heyn, W. Hansen, M. Morgenstern, and R. Wiesendanger, Phys. Rev. Lett. **91**, 196804 (2003).

146 J.-Q. Lu, H. T. Johnson, V. D. Dasika, and R. S. Goldman, Appl. Phys. Lett. **88**, 053109 (2006).

147 A. Urbieta, B. Grandidier, J. P. Nys, D. Deresmes, D. Stiévenard, A. Lemaître, G. Patriarche, and Y. M. Niquet, Phys. Rev. B **77**, 155313 (2008).

148 V. D. Dasika, R. S. Goldman, J. D. Song, W. J. Choi, N. K. Cho, and J. I. Lee, J. Appl. Phys. **106**, 014315 (2009).

149 J. C. Girard, A. Lemaître, A. Miard, C. David, and Z. Z. Wang, J. Vac. Sci. Technol. B **27**, 891 (2009).

150 L. W. Wang, J. Kim, and A. Zunger, Phys. Rev. B **59**, 5978 (1999).

151 O. Stier, M. Grundmann, and D. Bimberg, Phys. Rev. B **59**, 5688 (1999).

152 L. W. Wang, A. J. Williamson, A. Zunger, H. Jiang, and J. Singh, Appl. Phys. Lett. **76**, 339 (2000).

153 A. J. Williamson, L. W. Wang, and A. Zunger, Phys. Rev. B **62**, 12963 (2000).

154 V. Mlinar, M. Bozkurt, J. M. Ulloa, M. Ediger, G. Bester, A. Badolato, P. M. Koenraad, R. J. Warburton, and A. Zunger, Phys, Rev. B **80**, 165425 (2009).

155 S. Gaan, Guowei He, R. M. Feenstra, J. Walker, and E. Towe, Appl. Phys. Lett. **97**, 123110 (2010).

156 S. Gaan, Guowei He, R. M. Feenstra, J. Walker, and E. Towe, J. Appl. Phys. **108**, 114315 (2010).

157 D. Pal, and E. Towe, Appl. Phys. Lett. **88**, 153109 (2006).

158 L. Chen, D. Pal, and E. Towe, J. Cryst. Growth **251**, 208 (2003).

159 D. M. Bruls, J. W. A . M. Vugs, P. M. Koenraad, H. W. M. Salemink, J. H. Wolter, M. Hopkinson, M. S. Skolnick, F. Long, and S. P. A. Gill, Appl. Phys. Lett. **81**, 1708 (2002).

160 H. Eisele, A. Lenz, R. Heitz, R. Timm, M. Dähne, Y. Temko, T. Suzuki, and K. Jacobi, J. Appl. Phys. **104**, 124301 (2008).

161 R. M. Feenstra, Physica B **273-274**, 796-802 (1999).

162 We use the commercial package COMSOL, with elastic constants (in GPa) of C11=119, C12=53.8, and C44=59.9 for GaAs, and C11=83.29, C12=45.26, and C44=39.59 for InAs; from Semiconductors: Group IV Elements and III-V Compounds, edited by O. Madelung (Springer-Verlag, Berlin, 1991).

163 A. Urbieta, B. Grandidier, J. P. Nys, D. Deresmes, D. Stiévenard, A. Lemaître, G. Patriarche, and Y. M. Niquet, Phys. Rev. B **77**, 155313 (2008).

164 L. Nemec, F. Lazarevic, P. Rinke, V. Blum, M. Scheffler, APS March Meeting 2014, Volume 59, Number 1.